2020

Synthesis and Characterization of Carbon Sequestering Calcium Carbonate Cement

Mohammad Jobaer Uddin
University of North Florida, n01445294@unf.edu

SYNTHESIS AND CHARACTERIZATION OF CARBON SEQUESTERING CALCIUM CARBONATE CEMENT

by

Mohammad Jobaer Uddin

A thesis submitted to the School of Engineering in partial fulfillment of the requirements

for the degree of

Master of Science in Civil Engineering

UNIVERSITY OF NORTH FLORIDA

School of Engineering

Fall 2020

The thesis "Synthesis and Characterization of Carbon Sequestering Calcium Carbonate Cement" submitted by Mohammad Jobaer Uddin in partial fulfillment of the requirements for the degree of Master of Science in Civil Engineering has been

Approved by the thesis committee: **Date**

_____ _____

Dr. Paul D Eason
Thesis Advisor and Committee Chairperson

_____ _____

Dr. Craig Hargis

_____ _____

Dr. Raphael W Crowley

Accepted for the School of Engineering:

_____ _____

Dr. Osama Jadaan
Department Chair

Accepted for the College of Computing, Engineering, and Construction:

_____ _____

Dr. William Klostermeyer
Dean of the College

Accepted for the University:

_____ _____

Dr. John Kantner
Dean of the Graduate School

TABLE OF CONTENTS

TABLE OF CONTENTS iii

LIST OF TABLES vi

LIST OF FIGURES vii

ABSTRACT x

CHAPTER 1: INTRODUCTION 1

1.1 Background 1

1.2 Biomineralization and calcium carbonate 2

1.3 Calcium carbonate cement 6

1.4 Synthesis of vaterite 8

1.5 Carbon sequestering 10

1.6 Phase controlling chemistry of $CaCO_3$ 11

1.7 $CaCO_3$ characterization techniques 12

1.8 Importance of the study 12

CHAPTER 2: MATERIALS AND METHODS 15

2.1 Synthesis of vaterite using continuous stirred tank reactor (CSTR) 15

2.2 Preparation of cement paste and curing 17

2.3 X-ray diffraction (XRD) 18

2.4 Quantitative x-ray diffraction analysis 19

2.4.1 Kontoyannis and Vagenas (1999) method 19

2.4.2 Rietveld refinement 19
2.5 Particle size analysis (PSA) 20
2.6 Scanning electron microscopy (SEM) 21
2.7 Compressive strength test 21
CHAPTER 3: RESULTS AND DISCUSSIONS 23
3.1 Vaterite synthesis via CSTR 23
3.1.1 Effect of reaction temperatures 23
3.1.2 Effect of washing and drying methods 25
3.1.3 Effect of the relative concentration of reactants 26
3.2 Cement characterization 27
3.3 Role of divalent ions on phase transformation of cement 30
3.3.1 Transformation in DI water 30
3.3.2 Transformation in Mg^{2+} solution 32
3.3.3 Transformation in Mg^{2+} and Sr^{2+} solution 39
3.4 Effect of divalent ions on the crystal lattice of calcite and aragonite 42
3.5 Role of divalent ions on compressive strength development 45
3.5.1 Strength development in DI water 45
3.5.2 Strength development in Mg^{2+} solution 46
3.5.3 Strength development in Mg^{2+} and Sr^{2+} solution 49
3.6 Relationship between compressive strength and transformed phase 50

CHAPTER 4: CONCLUSIONS AND SUGGESTIONS FOR FUTURE STUDY 55

REFERENCES 57

APPENDIX A 63

LIST OF TABLES

Table 1.1 Selected properties of anhydrous crystalline polymorphs of $CaCO_3$. 4

Table 1.2 A summary of composition of $CaCO_3$ cements, and mechanical properties. 7

Table 1.3 Synthesis parameters and morphology of precipitated vaterite reported by Nebel & Epple (2008). 9

Table 2.1 List of parameters investigated to determine the favorable conditions for vaterite precipitation. 16

Table 2.2 Mix design of cement for transformation and compressive strength test. 18

Table 2.3 Crystalline structure model used in Rietveld analysis. 20

Table 3.1 Effect of hydrous and anhydrous washing and drying condition on vaterite. 26

Table 3.2 Calcite lattice parameters in different ages for DI solution. 30

LIST OF FIGURES

Figure 1.1 Simplified diagram of the cement production process and stagewise CO_2 release (Adopted from Maddalena, R., Roberts, J. J., & Hamilton, A., 2018). Half of the CO_2 emissions are from the thermal decomposition of $CaCO_3$ into CaO and CO_2. 2

Figure 1.2 Gibbs free energy diagram of anhydrous polymorphs of $CaCO_3$ (Reproduced from Müller et al., 2015). The high energy state of $CaCO_3$ (ACC) transforms into a low energy stable phase to achieve thermodynamic equilibrium. 5

Figure 1.3 A. (a) Formation of nano-sized ACC, (b) nano-aggregation of vaterite, (c) nano-aggregated micron-sized vaterite spherulites (Adapted from Rodriguez-Blanco et al., 2011). B. Graphical illustration of the formation of vaterite- (i) formation of vaterite core (grey) inside an amorphous crystal (pink), (ii-iii) branching of nanocrystals (grey), (iv) Formation of vaterite sphere and ripening (Adapted from Imai et al., 2011). 9

Figure 1.4 Hypothesized strength development mechanism in $CaCO_3$ cement. The presence of divalent ions favors acicular aragonite precipitation, which will provide better interlocking to achieve better compressive strength than the rhombohedral calcite. 14

Figure 2.1 CSTR designed for controlled solution precipitations. The reactants' concentrations were maintained using peristaltic pumps, and the residence time was controlled using inflow and outflow from the reactor. 16

Figure 2.2 Schematic diagram to make cement paste samples for determining the phase transformation and compressive strength. 18

Figure 2.3 Crystal structure of (1) Aragonite, (2) Calcite, (3) Vaterite. 20

Figure 2.4 Compression test set up. A displacement-based loading rate of 0.5 inches/ min was used for determining the compressive strength. 22

Figure 3.1 60 percent vaterite (V) and 40 percent calcite (C) synthesized at 4 °C; the SEM image shows the spherical vaterite and rhombohedral calcite. 24

Figure 3.2 SEM image showing an abundance (~90%) of spherical vaterite (V) precipitated at 20°C. 25

Figure 3.3 Effect of reactants' concentrations on the abundance of vaterite. Low Ca^{2+} to CO_3^{2-} ratio conducive to vaterite precipitation. 27

Figure 3.4 XRD pattern of $CaCO_3$ cement (Vaterite is 97.3 percent). 28

Figure 3.5 Particle size distribution of the $CaCO_3$ cement. 28

Figure 3.6 SEM image of the metastable $CaCO_3$ cement (spherical vaterite). Inset high magnification image of vaterite shows the nano-aggregated particles that comprise the micron-sized vaterite spherulite. 29

Figure 3.7 Transformation of vaterite in DI water. No untransformed vaterite was observed after 1 day. 31

Figure 3.8 SEM image of transformed calcite in DI water. 32

Figure 3.9 Transformation of vaterite 0.05 M Mg^{2+} solution 34

Figure 3.10 Transformation of vaterite 0.15 M Mg^{2+} solution. 35

Figure 3.11 Transformation of vaterite 0.50 M Mg^{2+} solution. 36

Figure 3.12 Decrease of vaterite transformation rate with the increase of Mg^{2+} concentration. 37

Figure 3.13 Transformation from vaterite to aragonite over time in different Mg^{2+} concentrations. 39

Figure 3.14 Transformation of vaterite in 0.15 M Mg^{2+} and 0.05 M Sr^{2+} solution. 40

Figure 3.15 a) SEM images of grinded hardened cement powder; b) Elongated acicular morphology of aragonite crystal. 40

Figure 3.16 Effect of Mg^{2+} and/or Sr^{2+} ions on the transformation rate of vaterite. 41

Figure 3.17 Transformation from vaterite to aragonite over time. 42

Figure 3.18 Effect of Mg^{2+} and Sr^{2+}ions on the aragonite lattice parameters at 7 days, (a) a and b axis, (b) c and a axis. 44

Figure 3.19 Compressive strength of $CaCO_3$ cement pastes made with DI water at different ages. Compressive strength remains relatively unchanged despite increased curing time. 45

Figure 3.20 Compressive strength of $CaCO_3$ cement pastes made with 0.05 M Mg^{2+} 46

Figure 3.21 Compressive strength of $CaCO_3$ cement pastes made with 0.15 M Mg^{2+} 48

Figure 3.22 Compressive strength of $CaCO_3$ cement pastes made with 0.50 M Mg^{2+} 49

Figure 3.23 Compressive strength of $CaCO_3$ cement pastes made with 0.15 M Mg^{2+} and 0.05 M Sr^{2+}. 50

Figure 3.24 Relationship between transformed phase and mechanical strength. 52

Figure 3.25 Schematic diagram illustrating the microstructure development of the hardened cement, ... 53

Figure 3.26 Fracture surface of compressive strength specimen of 0.50 M Mg^{2+} concentration at 7 days. 54

ABSTRACT

The cement industry is the second-largest manufacturing emitter of CO_2, and the manufacture and placement of concrete accounts for 7-8% of anthropogenic CO2 emissions. There is increasing pressure on the cement industry to develop a sustainable cement to support rapid global urban development without the associated emissions of cement production. The calcination reaction required to manufacture Portland cement is the prime source of emissions, so eliminating the release of CO_2 liberated during calcination of limestone provides an excellent opportunity to produce a more sustainable cement. Calcium carbonate ($CaCO_3$) cement is a novel alternative, which can eliminate the calcination process or close the loop on CO_2 emissions during cement production. In this study, a vateritic $CaCO_3$ is synthesized from the double decomposition reaction of equimolar $CaCl_2.2H_2O$ and Na_2CO_3 at room temperature using a continuous stirred-tank reactor (CSTR). The morphology of precipitated vaterite displays nano-aggregated micron-sized spherical particles. The dissolution of vaterite and recrystallization to a stable polymorph (calcite and/or aragonite) provides the necessary cementing reaction. Mg^{2+} and/or Sr^{2+} ions control the transformation kinetics and the abundance of the stable phase. However, the low concentration of Mg^{2+} (0.05 M) was insufficient to inhibit calcite formation and promote aragonite formation. Aragonite containing hardened cement exhibits 10 times higher compressive strength than a calcite containing one. The hardened cement exhibits a pH neutral microporous structure with relatively low compressive strength; the highest compressive strength was measured at approximately 1.11 MPa. By capitalizing on the unique properties of $CaCO_3$ cement, it can be developed as an ideal cement to support environmental restoration projects, such as oyster reef restoration along the Intracoastal Waterway in Florida, where the neutral pH of $CaCO_3$ cement and its chemical

composition provide it with enhanced properties for oyster recruitment compared to Portland cement.

Keywords: $CaCO_3$ cement, vaterite synthesis, phase transformation, calcite, aragonite, XRD, compressive strength, Rietveld analysis.

CHAPTER 1: INTRODUCTION

1.1 Background

Concrete is the most widely used human-made construction material (Naik, 2008) and the second most consumed substance globally, just after water (Sakai & Noguchi, 2012). More than 10 billion tons of concrete are produced yearly (Sakai & Noguchi, 2012). This ever-rising amount is predicted to grow up to 18 billion tons by 2050 (Mehta, 2002). Due to its enormous scale of production, it accounts for 7-8 % of global anthropogenic CO_2 emissions (Miller et al., 2016).

Concrete is primarily a heterogeneous mixture of rock, sand, binder, and water. Portland cement (PC) is ubiquitously used as a binder in the concrete industry. Global cement production has increased dramatically to keep up with the increasing concrete demand due to the urbanization of the rising population. It is expected that by the year 2050, global cement production will be approximately 4.68 billion tons per year (Schneider, 2019). Around the globe, 4.1 billion metric tons of cement were produced in 2019 (Wang, 2020). This production is expected to keep rising in the future as the demand for construction of buildings and infrastructures will keep increasing due to the need for settlement of the ever-rising population. Due to its scale, the cement industry is the second-largest manufacturing emitter of CO_2, just after the iron & steel industry, and the third-largest in anthropogenic gas emissions (Andrew, 2019). The global average CO_2 emission to produce a unit ton of cement is 0.95 tons (Ludwig & Zhang, 2015). The emissions can be attributed from three principal sources: 1) The calcination process to produce clinker (accounts for 50% of CO_2 emissions), 2) Fuel combustion in the rotary kiln (accounts for 35% of CO_2 emissions), and 3) Indirect emissions from electricity used to operate machinery, quarrying, and transportation of products (accounts for 10% of CO_2 emission), as shown in Figure 1.1 (Maddalena, R., Roberts, J. J., & Hamilton, A., 2018).

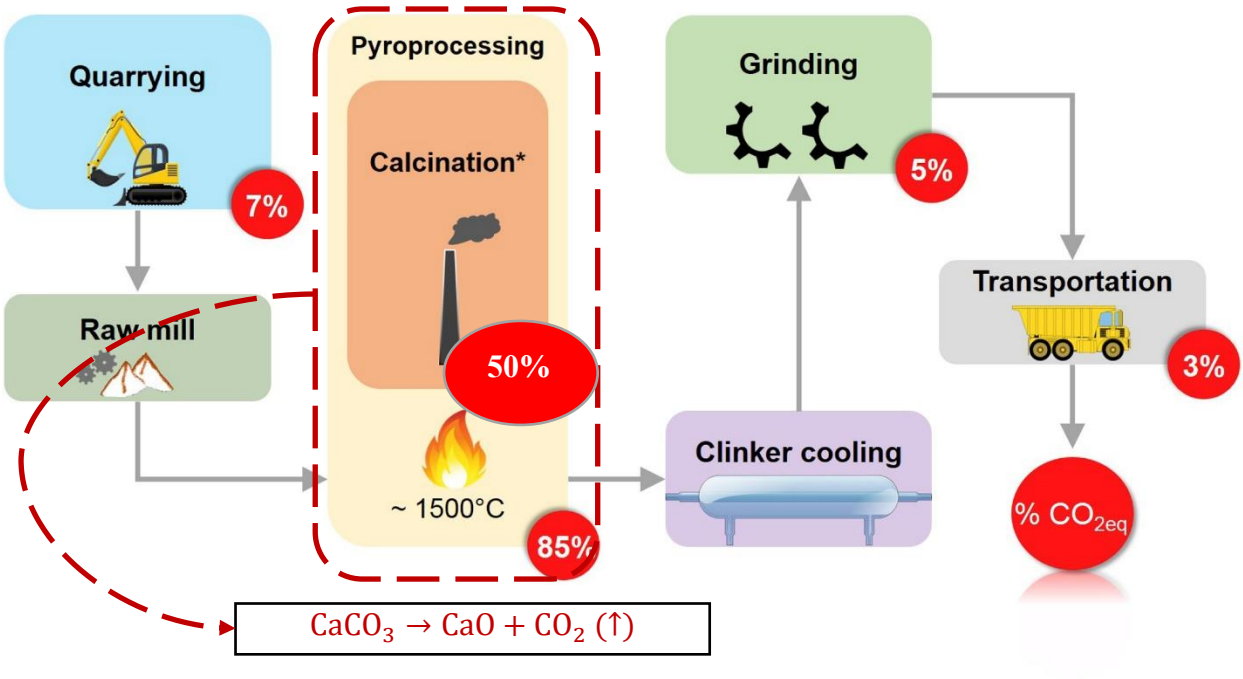

Figure 1.1 Simplified diagram of the cement production process and stagewise CO_2 release (Adopted from Maddalena, R., Roberts, J. J., & Hamilton, A., 2018). Half of the CO_2 emissions are from the thermal decomposition of $CaCO_3$ into CaO and CO_2.

The calcination process is the decomposition of limestone ($CaCO_3$) in pyroprocessing to produce CaO (a major constituent of cement) and is directly releasing CO_2 in the environment. The decarbonization of the cement industry has become an incumbent issue. IEA (2018) sets out a plan to reduce the total CO_2 from the industry by 50 % by 2050. In this regard, researchers have developed numerous methods to reduce CO_2 emissions from the cement industry. In general, those ideas concentrate on three main areas: 1) Improving manufacturing methods & efficiency, 2) Reducing clinker factor, and 3) Developing alternative cement to Portland cement. However, developing an alternative cement to Portland cement is the most direct method to reduce the cement industry's carbon footprint.

1.2 Biomineralization and calcium carbonate

Corals spend their lives building reefs through an intriguing process called biomineralization. The biomineralization process (Dhami et al., 2013) facilitates the

immobilization of CO_2 from the global environment and plays an essential role in sustaining ocean biodiversity. In the biomineralization process, oceans absorb roughly 30 percent of the globally emitted CO_2, which dissolves in water and produces HCO_3^-, as shown in Eq. 1.1 and 1.2 (Carilli et al., 2018). Oysters, corals, clams, sea urchins, and plankton utilize HCO_3^- and CO_3^{2-} to produce structural shells and/or skeletons, as shown in Eq. 1.3, and 1.4.

$$CO_2 + H_2O \rightarrow H_2CO_3 \quad \text{Eq. 1.1}$$

$$H_2CO_3 + OH^- \rightarrow HCO_3^- + H_2O \quad \text{Eq. 1.2}$$

$$HCO_3^- + OH^- \rightarrow CO_3^{2-} + H_2O \quad \text{Eq. 1.3}$$

$$CO_3^{2-} + Mg/Ca^{2+} \rightarrow CaCO_3/MgCO_3 \quad \text{Eq. 1.4}$$

Among mineral carbonates, biogenic $CaCO_3$ is the most common in marine organisms that create seashells and corals. For example, oyster shell is predominantly calcite with a small fraction of aragonite (Hamester et al., 2012). The binder component of oysters that cements individual oysters to build a colony is aragonite with a calcite phase (Burkett et al., 2010; Lombardi et al., 2013). The mechanical strength of the oyster reef is strong enough to protect the shoreline from storms and waves (Morris et al., 2019).

Calcium carbonate ($CaCO_3$) is also widely found in non-marine environments, from delicate eggshells to massive geological deposits; approximately 3-4 percent of the earth's crust is $CaCO_3$ (Gutschick, 2000). Common names for naturally deposited geological $CaCO_3$ include chalk, gypsum, limestone, dolomite, and marble. Aragonite and calcite are two anhydrous crystalline polymorphs of $CaCO_3$; calcite is the most stable polymorph, followed by aragonite. Amorphous calcium carbonate (ACC) and vaterite are two metastable phases of $CaCO_3$. Selected properties of the anhydrous phases of $CaCO_3$ are listed in Table 1.1. ACC and metastable vaterite will transform into more thermodynamically favorable phases such as aragonite and calcite, the

absence/presence of water can change the rate of transformation. Typical calcium carbonate morphologies and properties are shown in Figure 1.2.

Table 1.1 Selected properties of anhydrous crystalline polymorphs of $CaCO_3$.

Properties	Vaterite	Aragonite	Calcite
	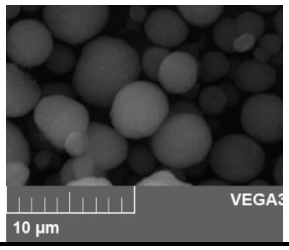	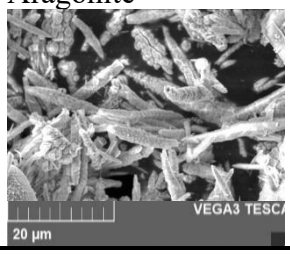	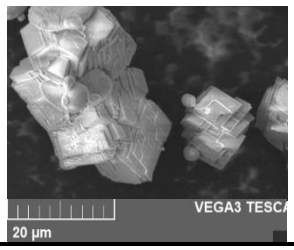
Density (g/cm^3) [1]	2.645	2.947	2.7102
Crystal System[1]	Hexagonal	Orthorhombic	Trigonal
Shape[1]	Spherical aggregates	Acicular	Rhombohedral
Hardness[1]	3	3.5-4	3
Abundance[2]	Rare	Common	Very Common

1. (Scott, 2012); 2. (Konopacka-Łyskawa, 2019)

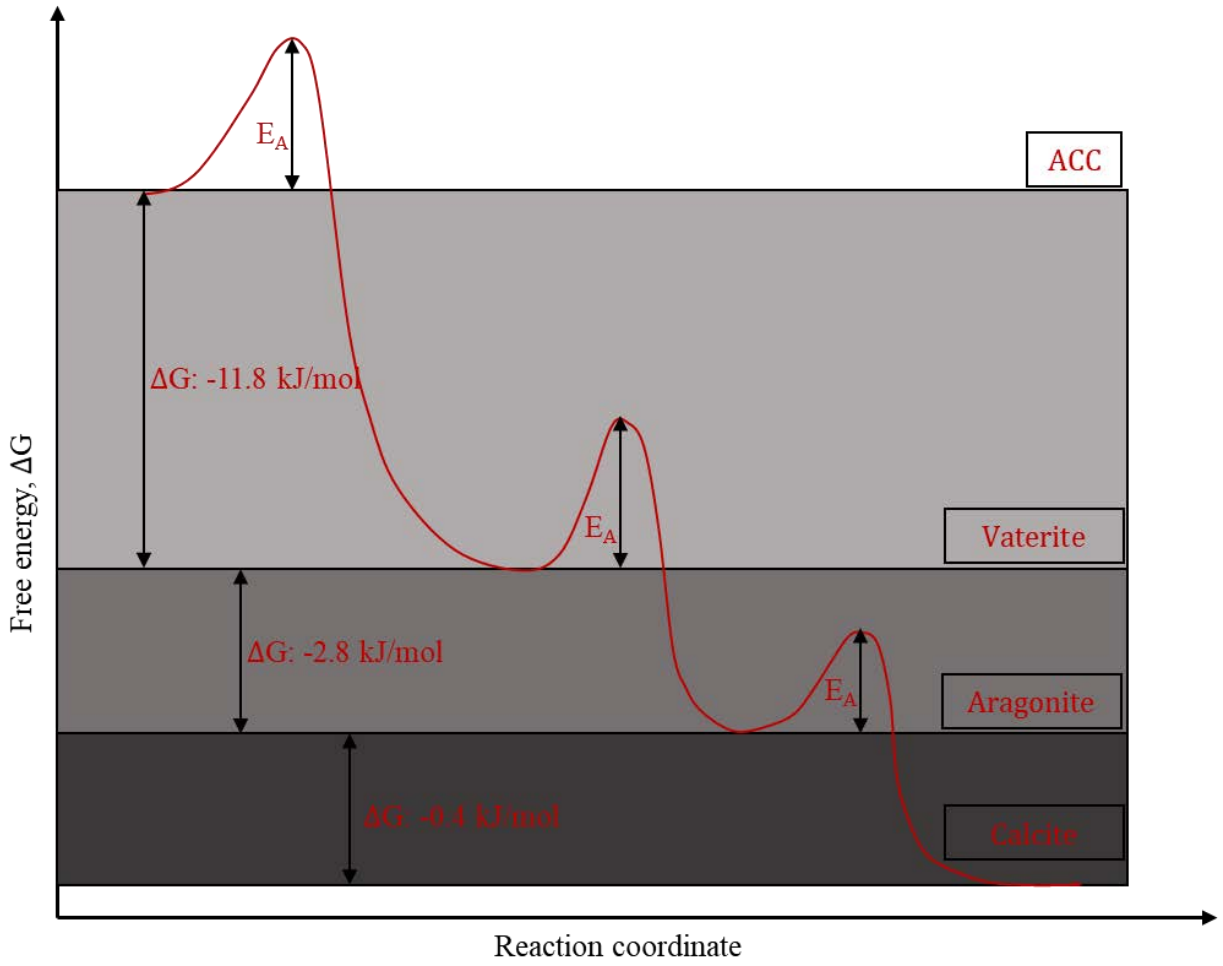

Figure 1.2 Gibbs free energy diagram of anhydrous polymorphs of $CaCO_3$ (Reproduced from Müller et al., 2015). The high energy state of $CaCO_3$ (ACC) transforms into a low energy stable phase to achieve thermodynamic equilibrium.

Both geological and biogenic $CaCO_3$ has been utilized in the construction industry for ages. Use of lime-based mortar for restorative projects in an application of geological $CaCO_3$. Burned oyster shells to produce building blocks are common in historic buildings from the coastal United States (Kelley, 2009). The development of $CaCO_3$ cement could significantly reduce the industry's CO_2 emission by evading the calcination reaction. The excellent chemical and mechanical properties of oysters inspired researchers to mimic nature and develop a $CaCO_3$ binder based on oyster shell chemistry (Lombardi et al., 2013). Aside from the interest of construction industry,

$CaCO_3$ is intriguing to the biomedical industry for bone filling and bone activity because of its excellent biocompatibility (Combes, et al., 2006).

1.3 Calcium carbonate cement

Fontaine et al. (2005) successfully developed a novel $CaCO_3$ cement with potential for orthopedic applications. Later, Combes et al. (2006) and Rodríguez-Sánchez et al. (2019) were able to produce a $CaCO_3$ biomedical cement through aqueous precipitation from the double decomposition reaction of $CaCl_2$ and Na_2CO_3. The cementitious properties of calcium carbonate can be harnessed via the transformation of $CaCO_3$ polymorphs from an amorphous phase and/or metastable phase (i.e. vaterite) to a more thermodynamically stable phase (i.e., aragonite or calcite) through a dissolution-reprecipitation process in an aqueous medium. The cement manufactured by Fontaine et al. (2005) was a biphasic $CaCO_3$ powder of aragonite and vaterite (metastable phase). Cement was mixed with the liquid (deionized water/ sodium chloride solution) and liquid to solid (L/S) ratios of 0.27-0.50 to start the cementing reaction. The compressive strength of the cement was approximately 3 MPa after casting of the wet cement in the mold and allowing for a cure time of 90 minutes. Combes et al. (2006) and Rodríguez-Sánchez et al. (2019), both used a biphasic mixture of highly reactive ACC and metastable vaterite at different ratios (1:1, 1:2, 1:3), and mixed with different L/S (deionized water/ sodium chloride) of 0.40-0.60 to investigate the effects of changing the calcium carbonate phases and L/S on setting behavior of fresh cement and the compressive strength development of hardened cement. The final cement exhibited micro-porosity and a low compressive strength (less than 13 MPa). However, Fontaine et al. (2005) and Combes et al. (2006) both claimed that such a low compressive strength would not hinder its application as a bone filler material in non-load-bearing defects. Cement produced from the carbonation reaction of sea water-based brine (0.18M Ca; 0.048 M Mg), in the presence of alkalinity (NaOH), with a

L/S (water) of 0.30 achieved a compressive strength of approximately 20 MPa and was promising for its potential use in construction applications (Constantz et al., 2011). Vaterite was the major phase in the cement. Similar to the biogenic oyster cement described previously, aragonite comprised the major phase (>75%) of the bulk material, and the elongated particle morphology leads to mechanical interlocking that was purportedly the mechanism for developing mechanical behavior in the hardened cement. Recently, Hargis et al. (2020) produced a $CaCO_3$ cement where vaterite was the major phase, and aragonite was found to be the major phase in the transformed hardened cement with a compressive strength of ~40MPa. The results of the studies mentioned above are summarized in Table 1.2 below. Clearly, initial powder composition, particle size, composition of the hardened cement, and morphology dramatically influence the bulk material behavior. Using predominately vaterite as the starting material, which then transforms to aragonite, in high yield, resulting in higher compressive strength (Constantz et al., 2011; Hargis et al., 2020) when compared to cements formed from primarily ACC precursor materials.

Table 1.2 A summary of composition of $CaCO_3$ cements, and mechanical properties.

Authors	Initial Composition	Mean Dia. (μm)	L/S	fc (MPa)	Transformed Composition
Fontaine et al. (2005)	A + metastable $CaCO_3$	n/a	0.25 - 0.60	~3	C and A
Combes et al. (2006)	Sr doped ACC + V	n/a	0.40	13	C
	Mg doped ACC + V	n/a	0.55	3	A (92%)
Combes et al. (2010)	ACC + V	2.1	0.67		A
Constantz et al. (2011)	V (82 %) + C	25	0.30	~ 20	A (>76%)
Rodríguez-Sánchez et al. (2018)	ACC + V	n/a	0.50	< 3	C (> 59%)
Myszka et al. (2019)	Mg doped ACC + V	2.5	0.50	~ 1	C
Hargis et al. (2020)	V (99.5 %) + C	15	0.35	~ 40	A (~100%)

L/S: liquid to solid ratio; fc: Compressive strength; ACC: Amorphous Calcium Carbonate; V: Vaterite; C: Calcite

1.4 Synthesis of vaterite

Spherical vaterite can be artificially synthesized using different techniques such as the double decomposition, solution method, diffusion method, and carbonation method (Konopacka-Łyskawa, 2019). Vaterite can be synthesized at low temperatures from 1°C to 30 °C (Ogino et al., 1987; Nebel & Epple, 2008). Nebel & Epple (2008) also stated that change of temperature controlled the abundance of vaterite fraction. The CO_3^{2-} and Ca^{2+} ratio can also control the relative phase fraction of precipitated vaterite (Chen & Xiang, 2009). Precipitated vaterite can transform into calcite in the presence of moisture. Washing and drying conditions at the post precipitation stage play an important role in stabilizing vaterite. Hydrous, (Chen & Xiang, 2009) anhydrous (Cherkas et al., 2018), or both (Nebel & Epple, 2008) washing methods of the precipitated $CaCO_3$ were reported in the literature. Nebel & Epple (2008) developed a protocol to synthesize vaterite using standard laboratory glassware from the double decomposition reaction of $CaCl_2$ and Na_2CO_3 at 1°C. Spherical shape nanoparticles of ACC formed immediately after mixing and followed by the formation of vaterite nanoparticles. Vaterite nanoparticles and ACC coexist for a few minutes. Then, ACC disappeared, and the nano-sized vaterite aggregated to micron-sized vaterite (Rodriguez-Blanco et al., 2011), as shown in Figure 1.3.

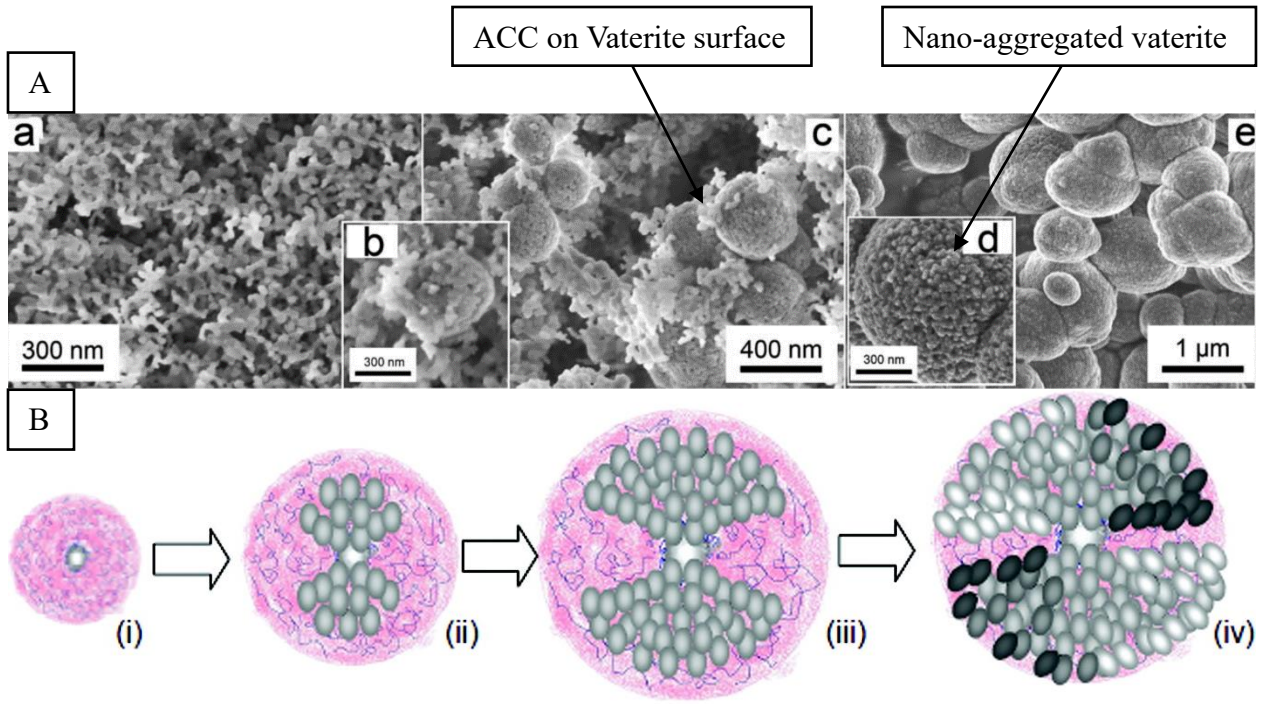

Figure 1.3 A. (a) Formation of nano-sized ACC, (b) nano-aggregation of vaterite, (c) nano-aggregated micron-sized vaterite spherulites (Adapted from Rodriguez-Blanco et al., 2011). B. Graphical illustration of the formation of vaterite- (i) formation of vaterite core (grey) inside an amorphous crystal (pink), (ii-iii) branching of nanocrystals (grey), (iv) Formation of vaterite sphere and ripening (Adapted from Imai et al., 2011).

. Under aqueous reaction conditions the supersaturation, temperature, pH, residence time, stirring speed, solvent, additives can control the purity and the morphology of precipitated vaterite (Konopacka-Łyskawa, 2019). Apart from spherical morphology, vaterite sometimes could be found with an ellipsoidal (Myszka et al., 2019) or lens-like (Li et al., 2002) morphology due to ions in the process solution inhibiting the growth of crystallographic faces. Usually, vaterite particle exhibits porous and high surface area than other anhydrous phases- calcite, and aragonite. Table 1.3 shows the reaction conditions and features of precipitated vaterite reported by Nebel & Epple (2008).

Table 1.3 Synthesis parameters and morphology of precipitated vaterite reported by Nebel & Epple (2008).

Parameters	**Value**
Molar concentration of [Ca^{2+}]	2 M

Parameters	Value
Molar concentration of [CO_3^{2-}]	0.05 M
pH of Ca^{2+} solution	2.7
pH of CO_3^{2-} solution	11.4
pH of the precipitated solution	8.7
Residence time	Few seconds
Particle size (μm)	0.1
Lattice parameter	a = 4.127; b = 7.121; c = 8.458
	α = β = γ = 90°

1.5 Carbon sequestering

Aside from the cementitious properties, calcium carbonate cement is also of interest for sustainable engineering applications due to its potential carbon-sequestration ability. Vaterite can be synthesized on an industrial scale using carbon capture technology (Chang et al., 2017; Constantz et al., 2011; Hargis et al., 2020). Na_2CO_3/$(NH_4)_2CO_3$ can be synthesized from the reaction of carbon dioxide with NaO, NaOH, and NH_4OH. Na_2CO_3/$(NH_4)_2CO_3$ can then be used as the carbonate source in the vaterite synthesis reaction, as shown in Eq 1.5 -1.7 (Azdarpour et al., 2018; Chang et al., 2017; Lee et al., 2016).

$$CO_2 + Na_2O \rightarrow Na_2CO_3 \quad \text{Eq. 1.5}$$

$$CO_2 + 2NaOH \rightarrow Na_2CO_3 + H_2O \quad \text{Eq. 1.6}$$

$$2NH_4OH + CO_2 \rightarrow (NH_4)_2CO_3 + H_2O \quad \text{Eq. 1.7}$$

The industrial-scale production of vaterite using industrial byproducts can further enhance the sustainability of $CaCO_3$ cement production by promoting industrial ecology in addition to carbon capture. However, as previously discussed, cement's hardened properties depend on the transformed phase, which bounds the scope of application of the $CaCO_3$ cement.

1.6 Phase controlling chemistry of $CaCO_3$

In an aqueous medium, phase transformation can be mediated by the presence (or absence) of different ions present in solution (Bischoff, 1968; Wada et al., 1995; Gutjahr et al., 1996). The synthesis of aragonite is slower than calcite. Aragonite's predominance will only be observed if aragonite formation is faster than calcite's transformation since calcite is the most thermodynamically favorable phase (Bischoff, 1968). Using FTIR analysis, Burkett et al. (2010) observed the presence of Mg^{2+} and Fe^{2+} in the material that cements individual oyster shells together, so biomineralization presumably incorporates ions from surrounding seawater. Additionally, the $CaCO_3$ at the cemented oyster shell connections was 33 percent aragonite and 66 percent calcite; however, no divalent cations other than Ca^{2+} were found in the shell, which is made of calcite, suggesting that ions can inhibit/promote the formation of less stable polymorphs. Mg^{2+} and Fe^{2+} have known calcite inhibitors during $CaCO_3$ phase transformation, meaning it will promote aragonite formation (Cherkas et al., 2018). Bischoff (1968) also stated that calcite inhibition was only possible when the concentration of Mg^{2+} was above the magnesite ($MgCO_3$) saturation. Mg^{2+} ions adsorb on the surface of the calcite and increase its solubility, thus hindering calcite's ability to crystallize. The same phenomenon is also applicable to other divalent inhibitors: Fe^{2+}, Cu^{2+}, and Zn^{2+} (Wada et al., 1995). Gutjahr et al. (1996) stated that calcite inhibition was mild if the concentration of Mg^{2+} is lower than 0.001 M. However, Mg^{2+} ions do not inhibit aragonite formation. Gutjahr et al. (1996) speculated that Mg^{2+} ions did not incorporate into the aragonite lattice but did for calcite. However, it is relevant to state that using higher concentrations of calcite inhibitors above a certain threshold can prevent vaterite transformation and reduce aragonite's crystal growth along the c-axis. The presence of Sr^{2+} with Mg^{2+} ions can catalyze aragonite formation (Bischoff, 1968; Boon et al., 2020; Wada et al., 1995). However, Sr^{2+} ions

facilitate transformation only when the concentration is above the strontianite ($SrCO_3$) saturation (approximately 0.0003 M). Bischoff (1968) stated that strontianite seeded aragonite growth by providing a similar crystal habit. Apart from the Sr^{2+} ion, Ba^{2+} also favors the formation of aragonite in a similar way.

1.7 $CaCO_3$ characterization techniques

The presence of different phases of anhydrous $CaCO_3$ can be identified using powder x-ray diffraction (XRD), Raman spectroscopy, and Fourier transform infrared spectroscopy (FTIR) (Vagenas et al., 2003). However, infrared spectroscopy was found ineffective due to band overlapping of calcite and aragonite (Kontoyannis & Vagenas, 2000). XRD is one of the most popular techniques to determine the phase fraction and crystal structural information using Rietveld analysis (Blake et al., (2008)). Morphology of $CaCO_3$ can be determined by imaging with optical microscopy (Plummer et al., 1982), scanning electron microscopy (Combes et al., 2006), and transmission electron microscopy (Nielsen et al., 2014). Researchers commonly use indentation hardness tests (Lombardi et al., 2013) and compressive strength tests (Combes, Miao, et al., 2006) to test mechanical properties. However, XRD, SEM, and compressive strength tests are the most common techniques for $CaCO_3$ cement characterization.

1.8 Importance of the study

All the above studies on phase transformations were conducted on the transformation mechanism of metastable $CaCO_3$ particles fully dissolved in a dilute aqueous medium, which are not relevant for practical cementing applications which require much lower L/S to achieve satisfactory mechanical performance. However, scant attention has been directed toward partial aqueous immersion, representing real-world applications and conditions (i.e., L/S < 1). Furthermore, the relationship between the transformed carbonate cement phase fraction and

compressive strength development has yet to be fully explored. The precipitation and polymorphic transformation of $CaCO_3$ are of interest to the scientific community due to its broader application in different fields, including geology, chemistry, materials science, physics, and biology to name a few; however, often these studies do not focus on the properties and conditions that would be necessary for civil engineering and/or biotechnology applications (Dhami et al., 2013). In the current study, bulk vaterite was synthesized via precipitation in a CSTR and characterized using XRD to confirm phase purity. Subsequently, the temporal conversion rate of vaterite to aragonite and/or calcite was investigated using various ionic solution precipitation conditions (Mg^{2+} and Sr^{2+}) to manipulate transformation. Finally, the mechanical properties, $CaCO_3$ phase fractions, and particle morphology were characterized using compressive loading, X-ray diffraction, and scanning electron microscopy, respectively. It is hypothesized that transformed cement containing needle-like aragonite will exhibit better compressive strength properties compared to transformed cement containing predominately calcite, as shown in Figure 1.4. Moreover, the study sought to further the scientific body of knowledge on calcium carbonate transformation reactions by identifying appropriate ionic concentrations that could control the transformation of vaterite to aragonite at low L/S needed in civil engineering applications.

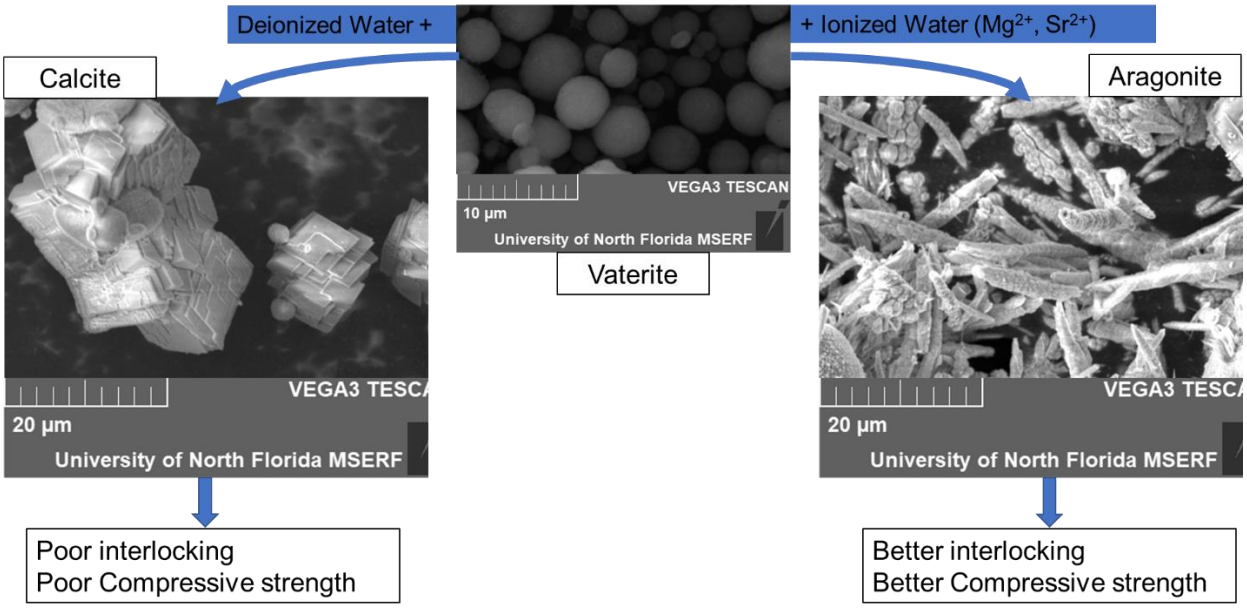

Figure 1.4 Hypothesized strength development mechanism in $CaCO_3$ cement. The presence of divalent ions favors acicular aragonite precipitation, which will provide better interlocking to achieve better compressive strength than the rhombohedral calcite.

CHAPTER 2: MATERIALS AND METHODS

2.1 Synthesis of vaterite using continuous stirred tank reactor (CSTR)

Solutions of calcium chloride ($CaCl_2.2H_2O$) and sodium carbonate (Na_2CO_3) were prepared by dissolving ACS grade anhydrous powders of $CaCl_2.2H_2O$ and Na_2CO_3 (VWR International) in deionized (DI) water. The dissolution reactions of $CaCl_2.2H_2O$ and Na_2CO_3 are exothermic. It is suggested to prepare the solutions a few hours before conducting the vaterite synthesis reaction to allow the solutions to return to room temperature prior to adding the last amount of water to create a solution with a particular molarity. Otherwise, the solution will have expanded, and its concentration will be incorrect. An alcohol thermometer was used to measure the reactant solution's temperature. The pH of solutions was determined by using universal plastic pH test strips purchased from LabRat Supplies. The Ca^{2+} solution and the CO_3^{2-} solutions were found acidic and basic, respectively, whereas the precipitated solution was pH neutral. Peristaltic pumps were used for continuous solutions inflow to a double-walled jacketed reactor passing through a Vigreux column (Figure 2.1). A mechanical stirrer was mixing the two solutions at a constant speed (999 rpm). Precipitation of vaterite required a very short residence time (less than a minute) via the solution mediated route (Nebel & Epple, 2008). Immediately upon mixing of the reactants, a white gel-like precipitate formed. An increase in residence time facilitates the crystallization of calcite.

The precipitated $CaCO_3$ was immediately collected by passing through a 2.5 μm membrane using vacuum filtration, and the supernatant was discarded. In this study, two different temperatures, three reactants ratios, and hydrous and anhydrous washing methods were studied to determine an optimum vaterite synthesis condition. Isopropyl alcohol purchased from VWR chemical used for anhydrous washing. The effect of drying conditions on the stabilization of

vaterite was also studied. Table 2.1 summarizes the experimental conditions investigated to determine the ideal condition for vaterite synthesis. The synthesized powder was stored in a vacuum desiccator until further analysis and testing.

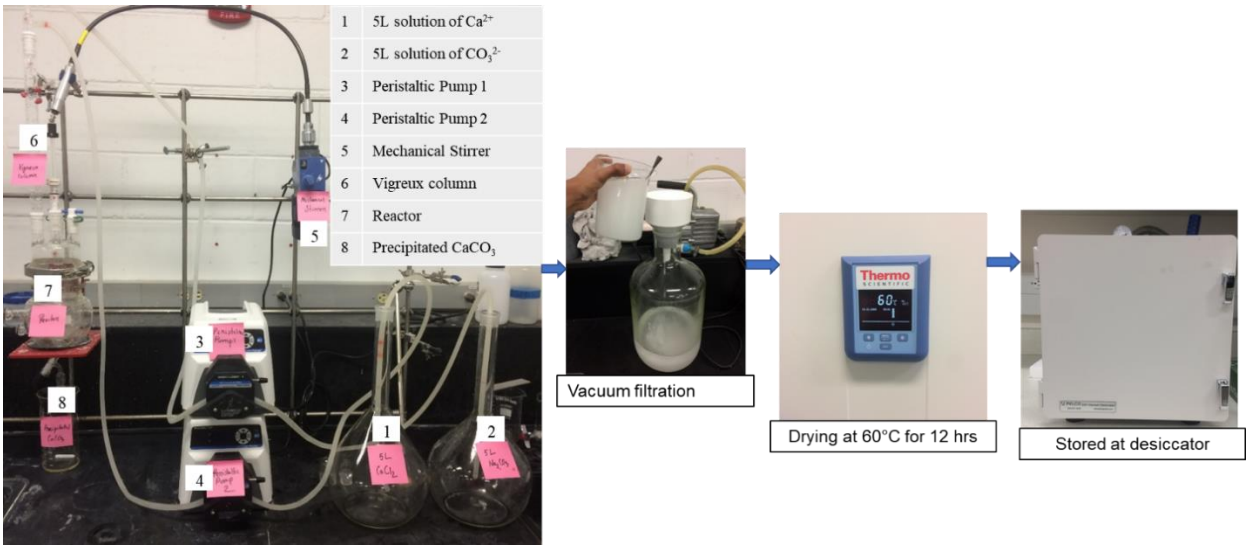

Figure 2.1 CSTR designed for controlled solution precipitations. The reactants' concentrations were maintained using peristaltic pumps, and the residence time was controlled using inflow and outflow from the reactor.

Table 2.1 List of parameters investigated to determine the favorable conditions for vaterite precipitation.

			Variable parameters			
ID	$[Ca^{2+}]$ (M)	$[CO_3^{2-}]$ (M)	Temperature	Washing	Drying	$[Ca^{2+}]/[CO_3^{2-}]$
1. a	2.00	0.05	**4°C**	-OH	60°C for 12 hr	40
1. b			**20°C**			
2. a	2.00	0.05	20°C	**DI**	-	40
2. b					**60°C for 12 hr**	
2. c				**-OH**	-	
2. d					**60°C for 12 hr**	
3. a	1.00	1.00	20°C	**DI**	60°C for 12 hr	1
3. b				**-OH**		
4. a	2.00	0.05	20°C	-OH	60°C for 12 hr	**40**
4. b	2.00	0.20				**10**
4. c	1.00	1.00				**1**

Bold texts are the variables corresponding to the case.

2.2 Preparation of cement paste and curing

Divalent salt (Mg^{2+}, Sr^{2+}) solutions were prepared by dissolving $MgCl_2.6H_2O$ (ACS grade purchased from VWR International) and $SrCl_2$ (Lab grade purchased from Thermo Fisher Scientific) in DI water and then mixing the solution with $CaCO_3$ cement at L/S = 1:2 to initiate the phase transformation of vaterite to aragonite/ calcite. A control batch of samples not subject to ionic solutions was prepared using only using DI water to determine the effect of divalent cations. The cylindrical mold of 1-inch diameter and height was used to make the compressive strength test cement specimen. The Crushed compressive strength specimens were then grinned and used for the XRD test. Fresh cement paste was consolidated for 1 minute using the Humboldt cylinder testing vibration table to remove air voids. Then, the cement paste samples were wrapped with plastic wrap to avoid evaporation and cured inside a plastic container at 60 °C for 24 hours in a relative humidity > 95 percent. Specimens were demolded after 24 hours. Test specimens of 6 hours and 1 day did not receive any additional curing. The 3- and 7-days samples were further cured at 60 °C in a solution bath containing the same solutions used in making the corresponding cement paste. Before performing the compressive strength tests, samples were dried at 105 °C for 3 hours to remove moisture. Figure 2.2 shows the process diagram to make cement paste samples for investigating the relationship between compressive strength and polymorph abundance. Table 2.2 shows the investigated parameters to understand the transformation mechanism and compressive strength development of the $CaCO_3$ cement.

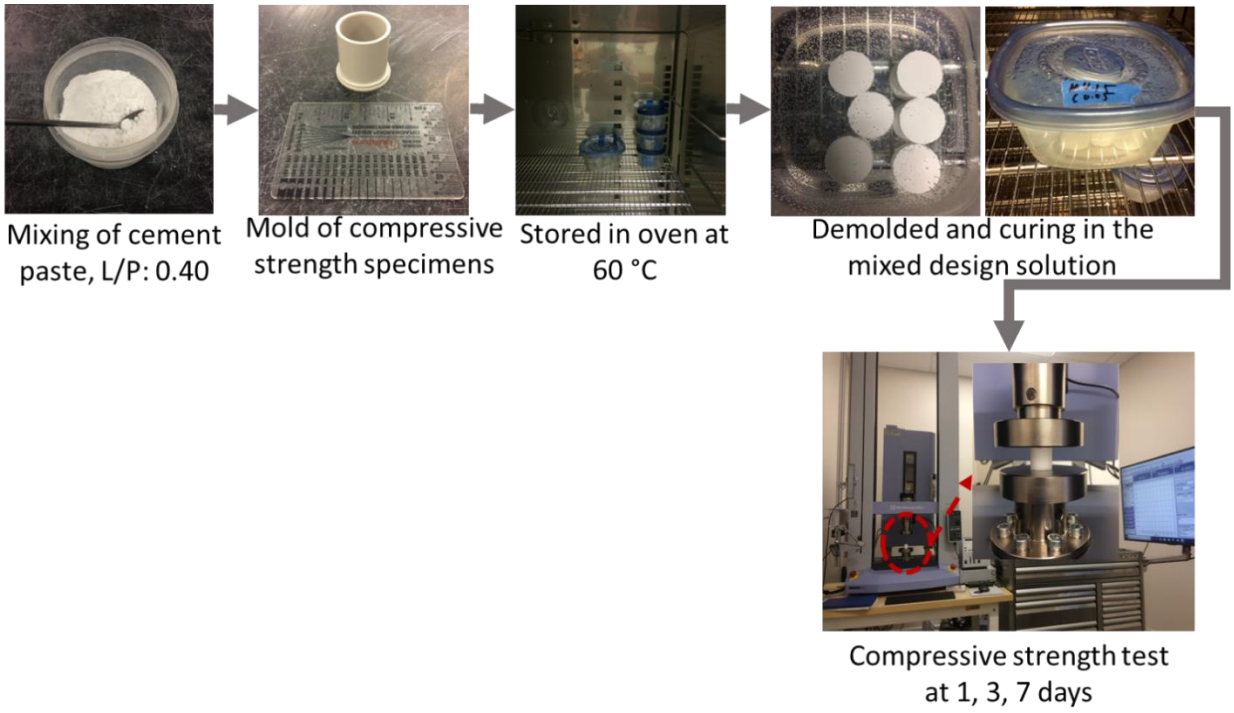

Figure 2.2 Schematic diagram to make cement paste samples for determining the phase transformation and compressive strength.

Table 2.2 Mix design of cement for transformation and compressive strength test.

Solution Type	L/S	Curing Temp.	XRD	fc
DI	0.5	60°C	¼, 1,3 and 7 days	1, 3, and 7 days
Mg 0.05 M			¼, 1 day	1 day
Mg 0.15 M			¼, 1,3, and 7 days	1, 3, and 7 days
Mg 0.50 M			¼, 1,3, and 7 days	1, 3, and 7 days
Mg 0.15 M & Sr 0.05			¼, 1,3, and 7 days	1, 3, and 7 days

2.3 X-ray diffraction (XRD)

X-ray diffraction was performed (Shimadzu XRD 6100) using Cu $K\alpha_1$ radiation and an acceleration voltage of 40 kV with a scan speed of 2°/min and a step size of 0.01°. The scan was performed over an angular range of 20° to 60°, as the major peaks of vaterite (110), calcite (104), and aragonite (221) have Bragg angles of 25°, 29.4°, and 45.6°, respectively (Kontoyannis &

Vagenas, 2000). Phase identification was confirmed by matching with standards from the Inorganic Crystal Structure Database (ICSD).

2.4 Quantitative x-ray diffraction analysis

2.4.1 Kontoyannis and Vagenas (1999) method

The Kontoyannis and Vagenas (1999) method were used for quantitative analysis of relative phase fractions of initial cement by using Eq. 2.1-2.3.

$$X_A = \frac{3.157 \times I_A^{221}}{I_C^{104} + 3.157 \times I_A^{221} + 7.691 \times I_V^{110}} \quad \text{Eq. 2.1}$$

$$X_C = \frac{I_C^{104} \times X_A}{3.157 \times I_A^{221}} \quad \text{Eq. 2.2}$$

$$X_V = 1.0 - X_A - X_C \quad \text{Eq. 2.2}$$

Whereas, X_V, X_A, and X_C stand for molar fractions of vaterite, aragonite, and calcite, respectively. I_V^{110} , I_A^{221} , and I_C^{104} are the intensity of vaterite, aragonite, calcite peak, corresponding to 2θ angle of 25° (110), 45.6° (221), and 29.4° (104) respectively.

2.4.2 Rietveld refinement

Rietveld refinement was used to determine the phase fractions of transformed cement because Kontoyannis and Vagenas (1999) method was found to underestimate the amount of aragonite during this study. The Rietveld method is a crystalline material characterizing tool to fit an experimental pattern with a calculated profiles and background. Phase identification was conducted by searching the XRD spectrum in the Crystallography Database. A phase identification program *Match! (Crystal Impact GbR)* and a Rietveld analysis program *FullProf (Juan Rodríguez-Carvajal, Laboratoire Léon Brillouin)* were used for crystal structure analysis and quantitative analysis. Background, specimen displacement correction, zero-point correction, and unit cell parameters were the parameters varied to reduce $\chi 2$ (goodness of fit) to less than 10 percent (in

most cases around 5 percent) and corresponding to a low Bragg R-factor. The smaller value of χ^2 and R-factor describes a good agreement between the observed and calculated patterns (Blake et al., 2009). It is relevant to mention that the R factor and χ^2 sometimes can be misleading. Hence, the graphical fittings of the calculated pattern were also observed to avoid any wrong estimation. Table 2.3 and Figure 2.3 show crystalline structure models of vaterite, aragonite, and calcite that were used for calibration and refinement.

Table 2.3 Crystalline structure model used in Rietveld analysis.

Phase	COD #	Space Group	Crystal System	Lattice Parameters (Å)
Aragonite[1]	9013801	P m c n	Orthorhombic	a = 4.962; b = 7.969; c = 5.743
Calcite[2]	9016706	R -3 c	Trigonal	a = b = 4.984; c = 17.0376
Vaterite[3]	9015898	P 63/m m c	Hexagonal	a = b = 4.130; c = 8.475

1. (Antao & Hassan, 2009); 2. (Ondruš et al., 2003); 3. (Le Bail et al., 2011)

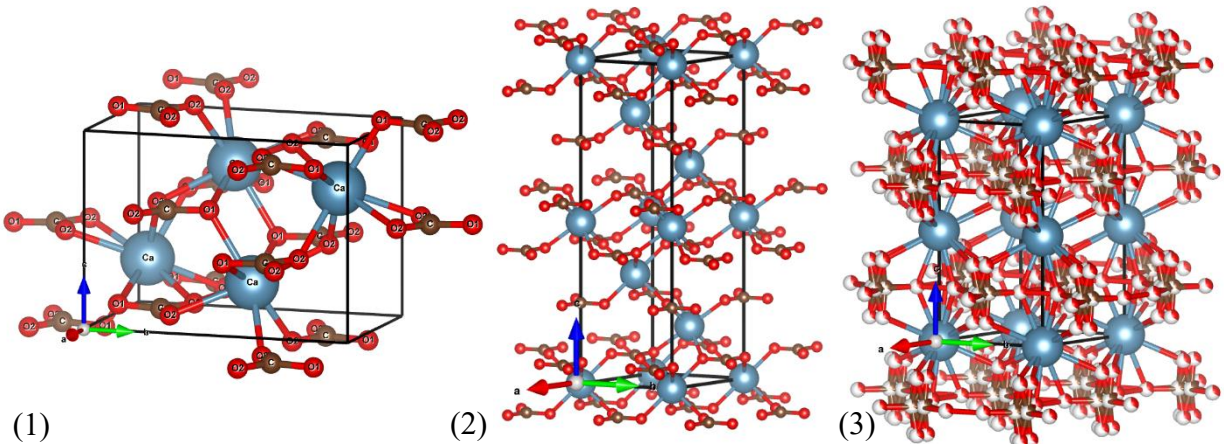

(1) (2) (3)

Figure 2.3 Crystal structure of (1) Aragonite, (2) Calcite, (3) Vaterite.

2.5 Particle size analysis (PSA)

A Horiba LA-950V2 Laser Scattering Particle Size Distribution Analyzer (two light sources: 650 nm wavelength laser and 405 nm wavelength LED) was used to study the particle

size distribution of the $CaCO_3$ cement. Measurements were carried out with test samples dispersed in water using refractive indexes of 1.33 for water and 1.58 for $CaCO_3$.

2.6 Scanning electron microscopy (SEM)

Secondary electron images were obtained using a Tescan Mira and Vega 3 microscopes. Vega 3 has a tungsten source and was found adequate for imaging of the bulk cement powder. However, Mira was found useful for close-up imaging of crystals and imaging fracture surfaces. The accelerating voltage varied from 2 kV to 30 kV, and working distance varied from 15 mm to 17 mm was used. Fine powder specimens were mounted on aluminum SEM stubs using adhesive carbon tape and coated with a thin layer of gold to enhance conductivity for imaging. For imaging the hardened cement fracture surface, a 4-5 mm piece of the compressed sample was attached to the sample stub using graphene paint. Then a conductive line was drawn from the stub to the top of the sample using paint. For both imaging cases, the samples were coated with gold (Au) coating using a Cressington sputter coater for 30 seconds in automatic operation mode.

2.7 Compressive strength test

Cylindrical specimens of 1-inch (25.4 mm) height and diameter were made for the compressive strength test. Compression tests were performed at 1, 3, and 7 days using a Shimadzu AGS-X, 50 kN machine, as shown in Figure 2.4. A displacement-based loading rate of 0.5 inches/min was used to determine the compressive strength for all ages. A crushing strength below 0.5 inches of specimen height was unreliable and to sustain the test for 1 minute. A 20 percent drop from the maximum load or top platen height below 0.50 inches was considered the failure criterion for stopping. The average crushing strength of three samples was reported as the compressive strength with standard deviation at each timepoint.

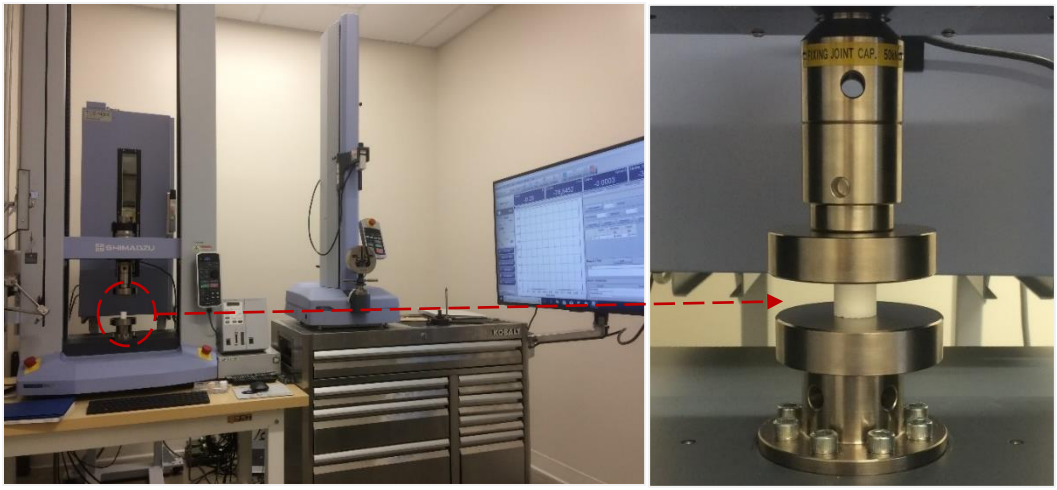

Figure 2.4 Compression test set up. A displacement-based loading rate of 0.5 inches/ min was used for determining the compressive strength.

CHAPTER 3: RESULTS AND DISCUSSIONS

3.1 Vaterite synthesis via CSTR

3.1.1 Effect of reaction temperatures

Initially, vaterite was synthesized by mixing a 2 M solution of $CaCl_2.2H_2O$ and a 0.05 M solution of Na_2CO_3 at near-freezing temperature (4°C) following the experimental protocol of Nebel & Epple (2008). The amount of vaterite, aragonite, and calcite was estimated using Kontoyannis & Vagenas (1999). The $CaCO_3$ powder synthesized at 4°C comprised of 60 percent vaterite (V) and 40 percent calcite (C), whereas Nebel & Epple (2008) reported pure vaterite at 1°C. Figure 3.1 shows the XRD spectrum (inset) of the biphasic $CaCO_3$ powder and the morphology of the synthesized powder. The higher temperature of the reaction could be responsible for the lower vaterite phase fraction. However, the pH of the precipitated $CaCO_3$ is also lower (pH = ~7), whereas Nebel & Epple (2008) found a basic precipitated solution. Probably, the combination of low pH and temperature was not conducive for vaterite stabilization. Accordingly, Tai & Chen (1998) stated that a pH neutral reaction condition at room temperature was conducive for vaterite stabilization. Combes et al. (2006) and Rodríguez-Sánchez et al. (2019) also synthesized $CaCO_3$ powder containing vaterite as the major phase at 30°C and 20°C, respectively.

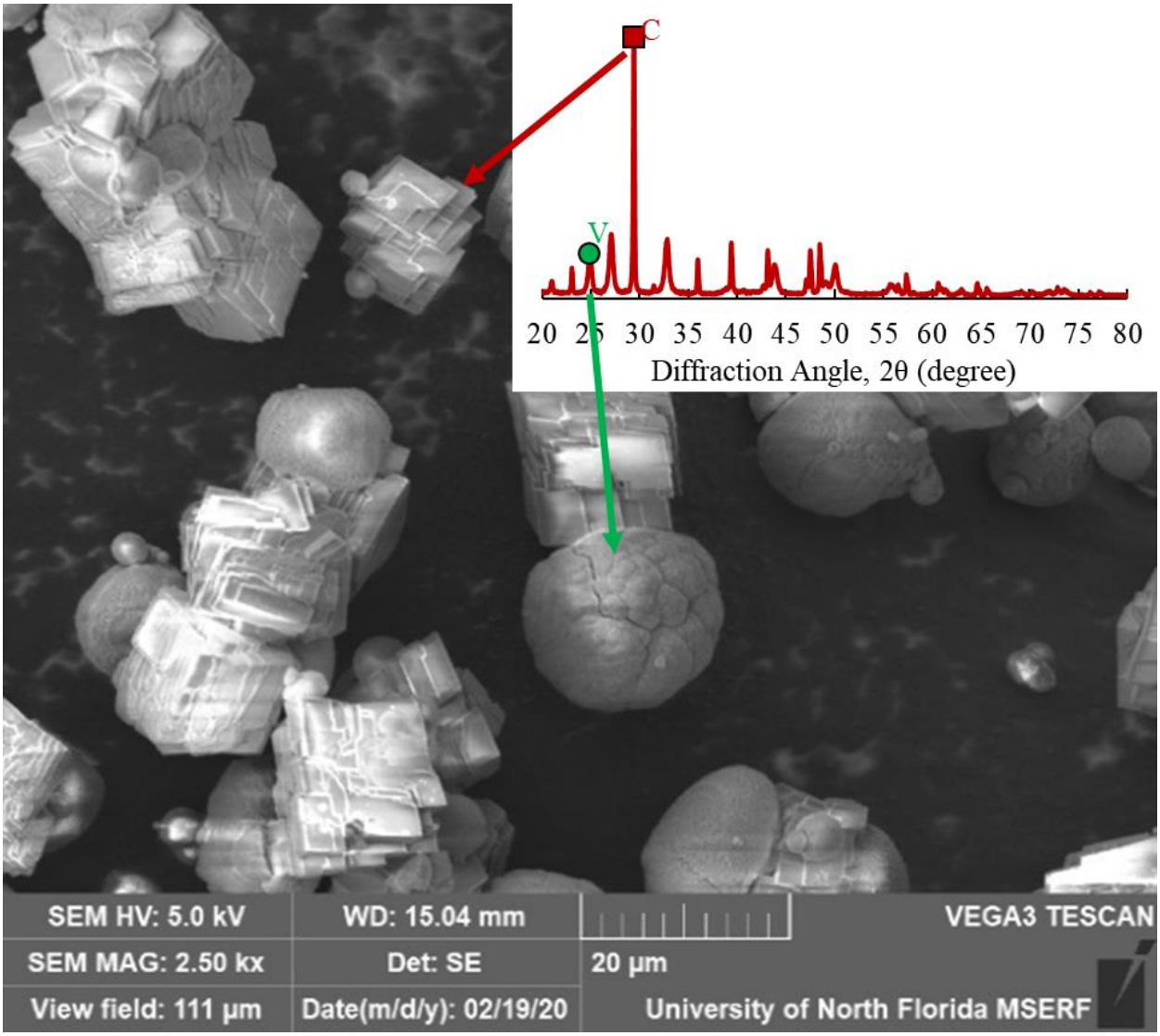

Figure 3.1 60 percent vaterite (V) and 40 percent calcite (C) synthesized at 4 °C; the SEM image shows the spherical vaterite and rhombohedral calcite.

By only changing the reaction temperature from 4°C to room temperature (20°C), the vaterite amount rose from 60 percent to 90 percent, as shown in Figure 3.2. Tai & Chen (1998) also found the comparably same amount of vaterite at 20°C. Consequently, 20°C room temperature was selected as the optimal temperature for vaterite synthesis and used to synthesize cement.

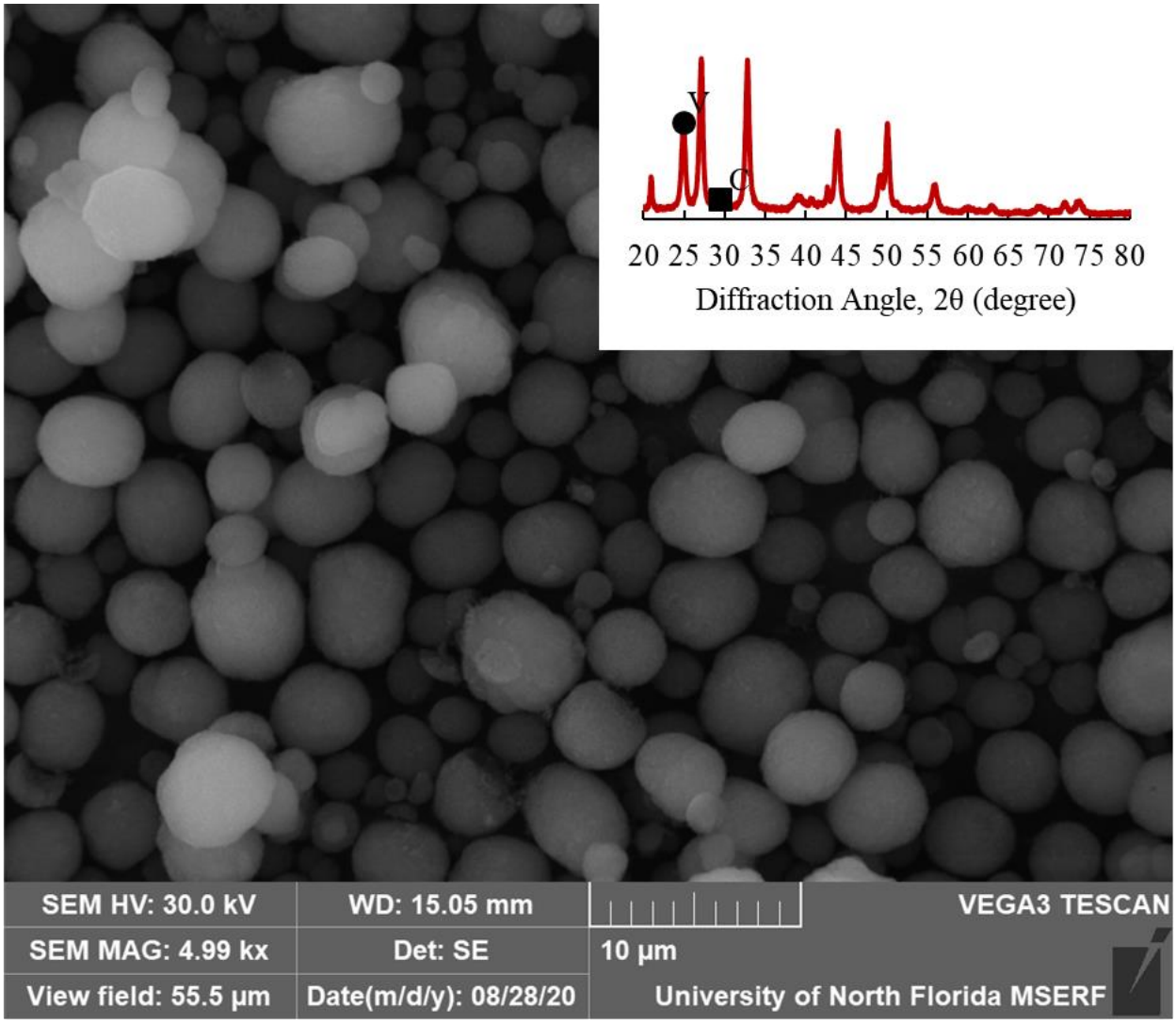

Figure 3.2 SEM image showing an abundance (~90%) of spherical vaterite (V) precipitated at 20°C.

3.1.2 Effect of washing and drying methods

Six cases were investigated, keeping the same reaction conditions except varying the washing and drying methods, as shown in Table 3.1. A low amount of vaterite was measured via XRD if the powder was not dried in the oven. An increase in vaterite purity was observed by oven drying the powder. Consequently, it is speculated that atmospheric moisture may have accelerated the transformation of vaterite to calcite. Moreover, an alcohol wash helped remove adherent moisture from the surface of the vaterite and slow down the transformation reaction rate. The

sample only washed with alcohol shows more vaterite content than the sample washed with DI water. The combination of an ethanol wash and drying in the oven resulted in more favorable vaterite formation conditions. Approximately 55 percent pure vaterite resulted from using an alcohol wash combined with oven drying compared to 22 percent vaterite from using a DI water wash and no drying. Optimal conditions were determined to be the room temperature equimolar case. Approximately 93 percent pure vaterite was formed when samples were washed with alcohol and dried in the oven.

Table 3.1 Effect of hydrous and anhydrous washing and drying condition on vaterite.

Cases	Reaction Temperature (°C)	[$CaCl_2.2H_20$]	[Na_2CO_3]	V (%)
DI wash only	4	2.00	0.05	22.79
DI wash + Drying				53.48
Ethanol wash				36.52
Ethanol wash + Drying				55.27
DI wash + Drying	20	1.00	1.00	79.85
Ethanol wash + Drying				93.26

3.1.3 Effect of the relative concentration of reactants

Luo et al. (2020) reported that excess CO_3^{2-} ions to Ca^{2+} ions might increase vaterite precipitation. To determine the effects of concentration on the reaction products, three concentration ratios of Ca^{2+}:CO_3^{2-} were investigated (40:1, 5:1, and 1:1). Figure 3.3 shows an increase in the vaterite fractions with the decrease in the Ca^{2+}: CO_3^{2-}, which is in agreement with the findings of Luo et al. (2020). Han et al. (2006) also reported similar findings when prepared $CaCO_3$ using the CO_2 bubbling method. In other words, an increase of Ca^{2+} to CO_3^{2-} is found beneficial to calcite formation and not vaterite formation. It is speculated that the change in pH to an alkaline environment with the increase of CO_3^{2-} in the reactor increases the vaterite fraction (Luo et al., 2020). Besides, an increase in the yield of vaterite content was also observed for the equimolar case. Despite changing Ca^{2+}: CO_3^{2-}, pH of the synthesized cement remained almost neutral (~7).

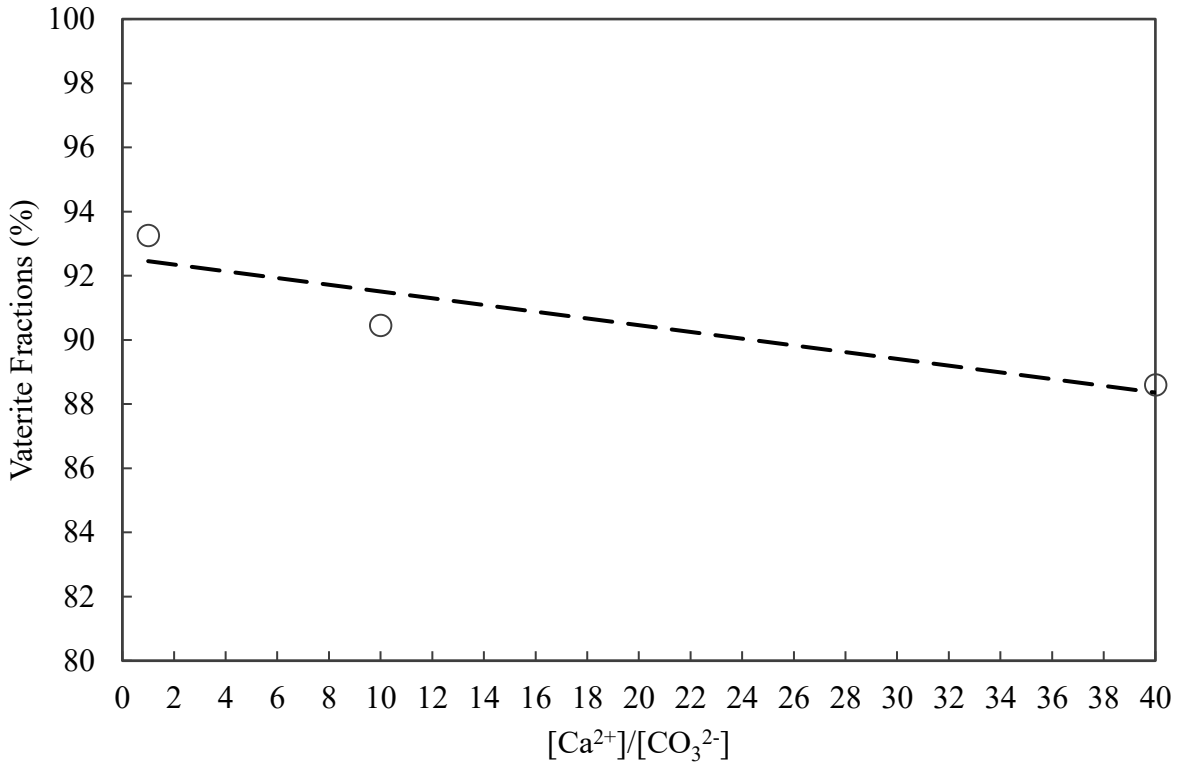

Figure 3.3 Effect of reactants' concentrations on the abundance of vaterite. Low Ca^{2+} to CO_3^{2-} ratio conducive to vaterite precipitation.

3.2 Cement characterization

The optimized precipitation conditions were used to produce several vaterite batches, which were characterized to assess purity, then blended into a bulk batch of cement precursor material. The material contained 97 percent vaterite (V) and 3 percent calcite (C) as measured via refinement of the XRD spectra (Figure 3.4). The fractions of phases were estimated using both the Kontoyannis and Vagenas (1999) equations and Rietveld analysis. The mean and median size of the cement particles, determined from PSA, was 4.12 μm and 3.85 μm, respectively (Figure 3.5). The D_{10} and D_{90} for the cement are 6.49 μm and 2.09 μm. The lattice parameters of the hexagonal vaterite crystal were calculated to be a = b = 4.12529 Å and c = 8.46502 Å via Rietveld analysis of the XRD pattern. The low R-factor (7.8%) and goodness of fit (chi^2 =5.9) value show a good agreement between observed and model data.

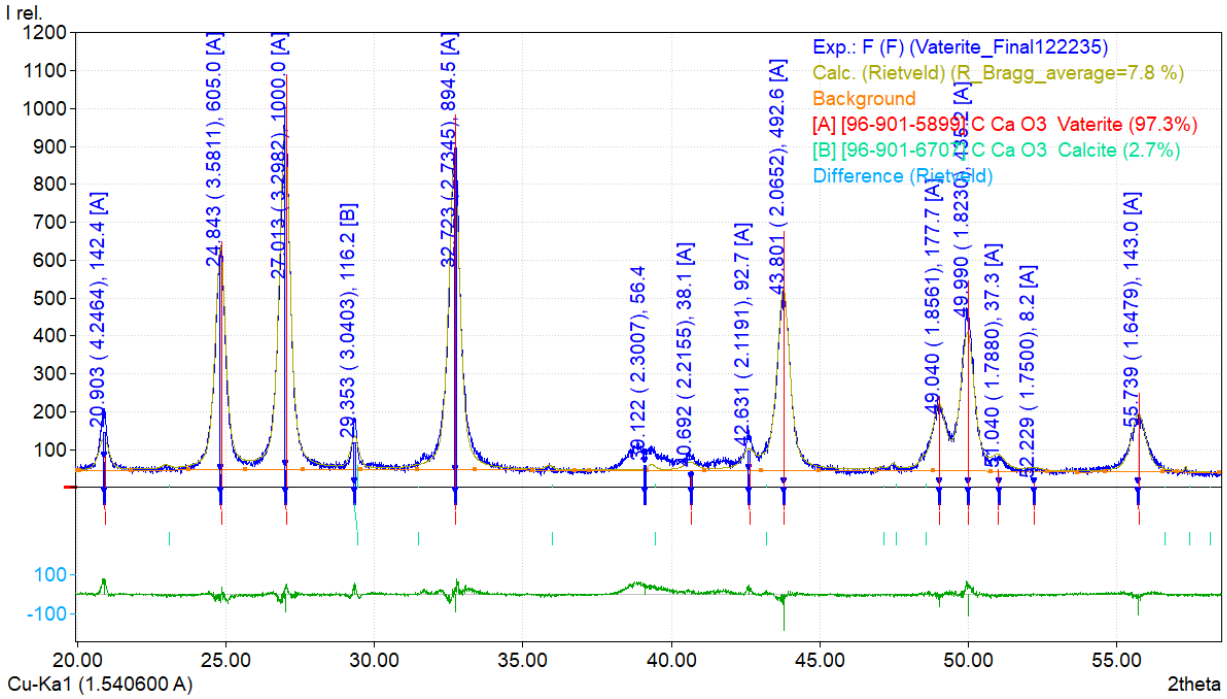

Figure 3.4 XRD pattern of $CaCO_3$ cement (Vaterite is 97.3 percent).

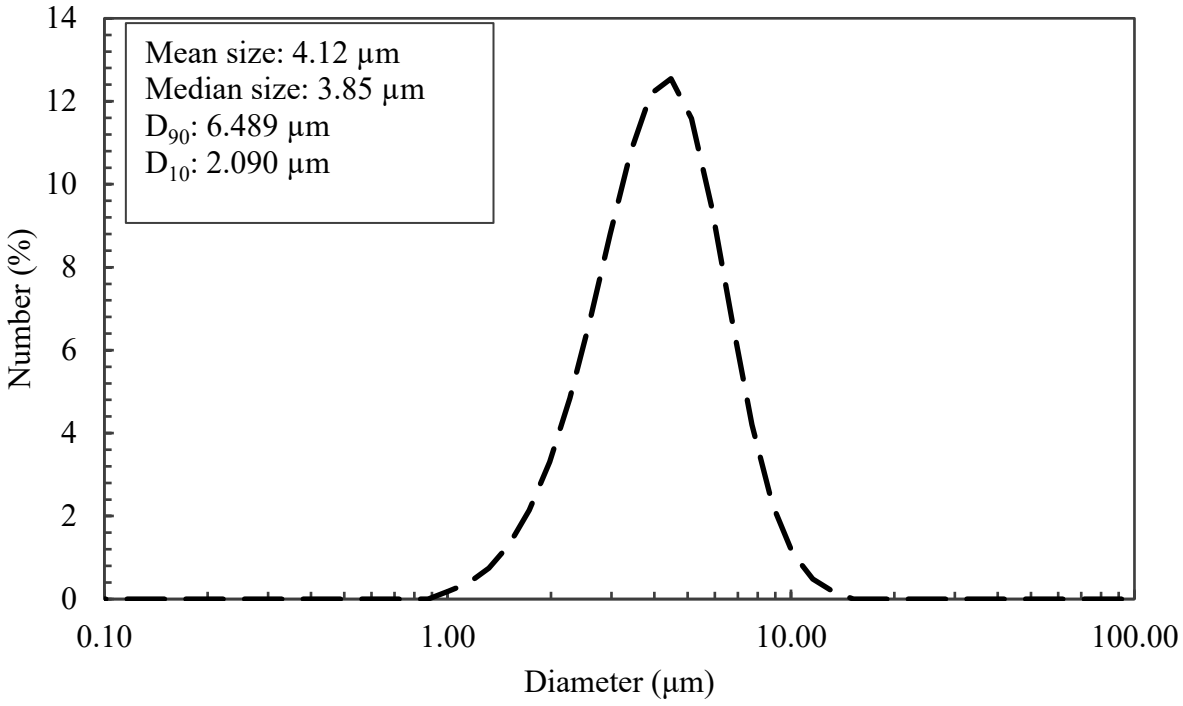

Figure 3.5 Particle size distribution of the $CaCO_3$ cement.

Figure 3.6 shows the spherical morphology of the vaterite particles. Agglomeration of precipitated vaterite primary crystals to form a large vaterite sphere is also observed for particles that are in close contact. Cherkas et al. (2018) also observed the agglomeration behavior of vaterite particles. They reported a porous inner structure of the agglomerated vaterite particles. This type of agglomerated microstructure is referred to as framboidal, after the French word for raspberry.

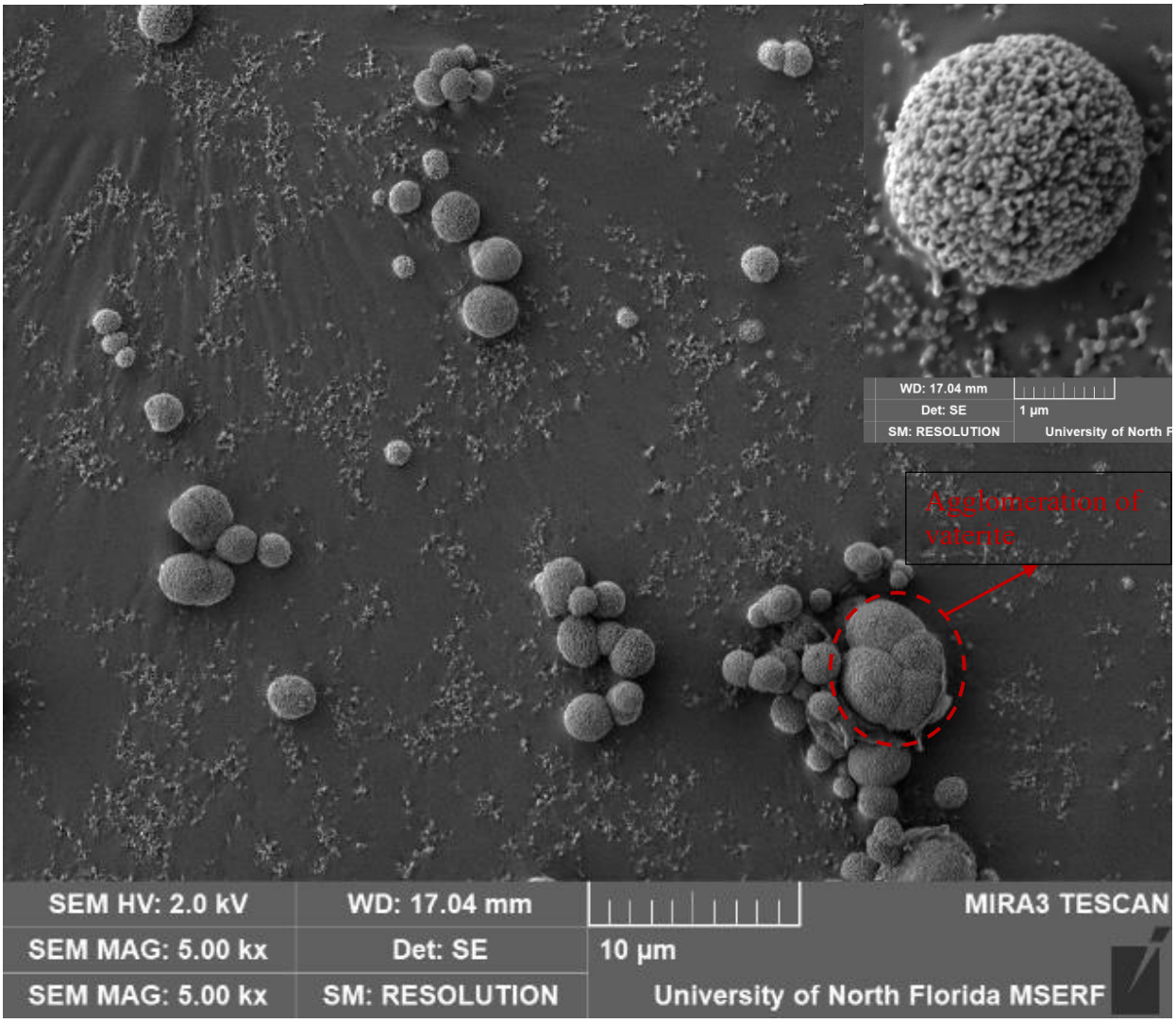

Figure 3.6 SEM image of the metastable $CaCO_3$ cement (spherical vaterite). Inset high magnification image of vaterite shows the nano-aggregated particles that comprise the micron-sized vaterite spherulite.

3.3 Role of divalent ions on phase transformation of cement

3.3.1 Transformation in DI water

Transformation in pure DI water led to the transformation of almost 80 percent of the vaterite into calcite within the first 6 hours after making of cement paste (Figure 3.7). Rhombohedral calcite was the only phase after 24 hours (1 day). Appendix: A.1 and Appendix: A.2 show the XRD patterns and Rietveld refinements of the $CaCO_3$ cement in DI water. No aragonite formation was observed. In contrast, Cherkas et al. (2018) observed aragonite at 6 hours in a more dilute $CaCO_3$ system. They also reported slower vaterite to calcite transformation kinetics in DI water. The high liquid to powder ratio (L/S = 100) may change the formation kinetics and abundance of polymorphs, compared to the present study.

The greater bulk solubility constant of vaterite $K_{vaterite}$ (60 °C) = $10^{-8.275}$ compared to calcite $K_{calcite}$ (60 °C) = $10^{-8.759}$ is the driving force in the transformation (Plummer et al., 1982). The more soluble vaterite dissolves and recrystallizes into the less soluble and more thermodynamically stable polymorph, calcite. The calcite transformation rate declined with time. Spanos & Koutsoukos (1998) reported that in the presence of calcite, the transformation rate of vaterite to calcite is controlled by vaterite dissolution. In the present study, the approximately 3 percent calcite impurity in the initial vaterite powder would therefore seed the vaterite to calcite transformation. The rate of transformation declines as there is less vaterite to dissolve. Table 3.2 shows the lattice parameters found from the Rietveld analysis.

Table 3.2 Calcite lattice parameters in different ages for DI solution.

Age	a = b (Å)	c (Å)	R Bragg factor	χ^2
Initial calcite	4.984	17.038		
6 hours	4.984	17.051	9.9	7.3
1 day	4.985	17.054	9.7	5.3

The Lattice parameters a and b remain constant; however, the c lattice parameter is slightly larger in the calcite that is transformed from vaterite. The accompanying salt, NaCl present in the vaterite synthesis, may be substituted into the calcite crystal during synthesis at a trace amount. Since the ionic radii of sodium and chlorine are less than those of calcium and carbonate, respectively, then that would cause a reduction in the lattice parameter. However, further testing would be necessary to prove the hypothesis.

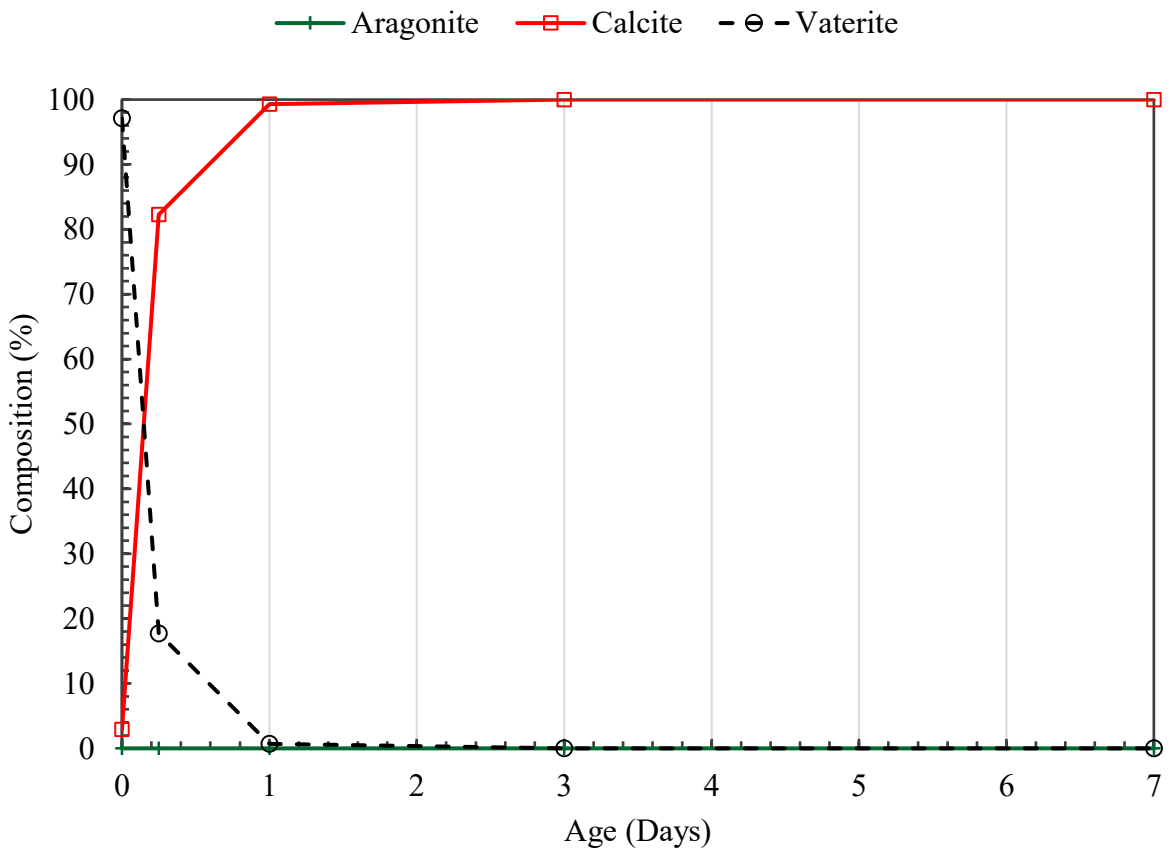

Figure 3.7 Transformation of vaterite in DI water. No untransformed vaterite was observed after 1 day.

Figure 3.8 shows the rhombohedral morphology of calcite. The size of calcite crystals varies widely, indicating different amounts of precipitation and growth. The largest crystals

probably represent the 3% calcite impurity in the $CaCO_3$ cement since those calcite crystals would have the most time to grow from the Ca^{2+} and CO_3^{2-} ions released during vaterite dissolution.

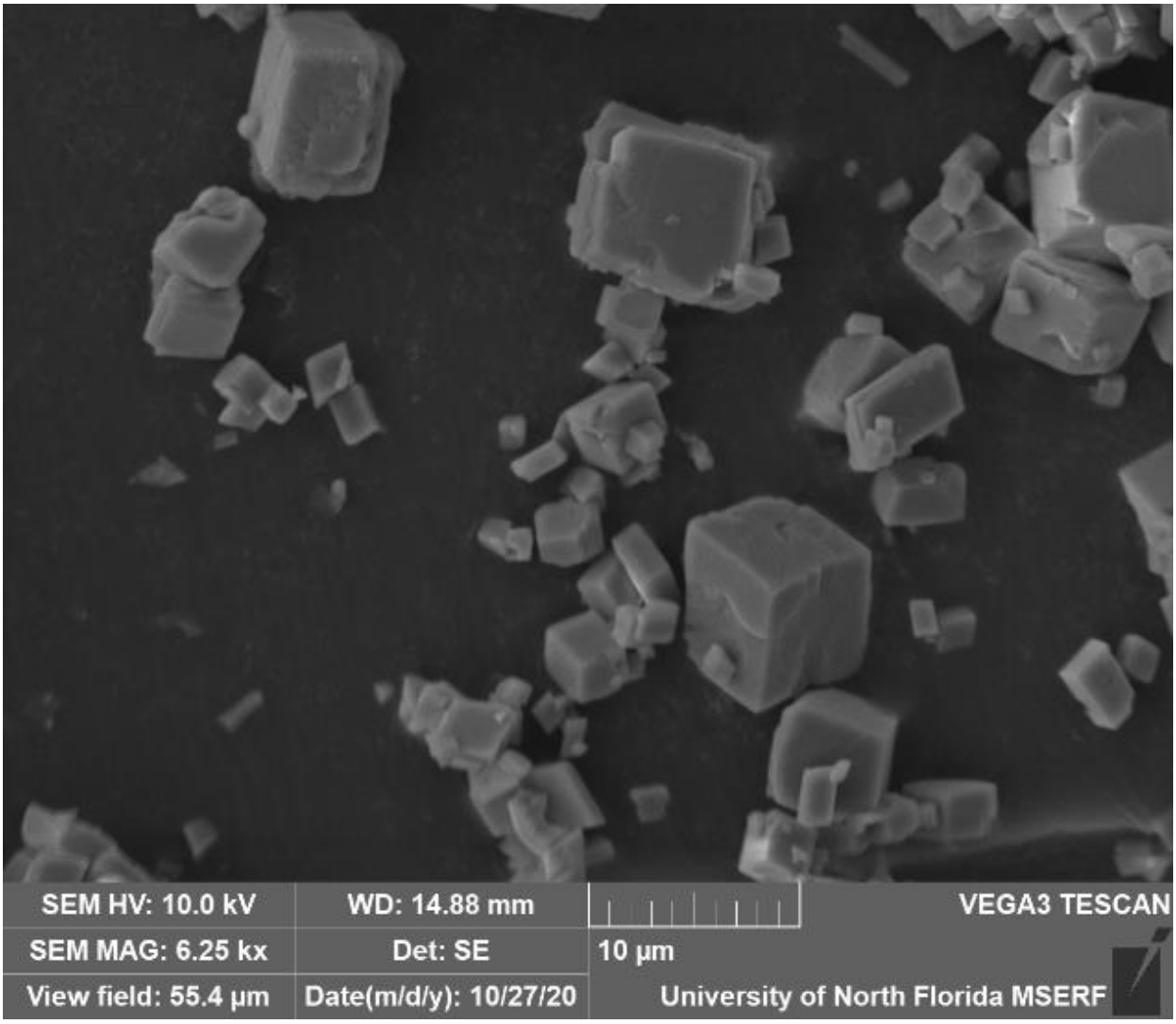

Figure 3.8 SEM image of transformed calcite in DI water.

3.3.2 Transformation in Mg^{2+} solution

As discussed, the presence of Mg^{2+} ions during the dissolution of vaterite inhibits the precipitation of calcite. It favors needle-like aragonite formation, which is hypothesized to be the preferred hardened cement phase due to the ability of the aragonite needles to form an interlocking network. However, prior studies were done in dilute suspensions (L/S ~ 100) at relatively low

concentrations of Mg^{2+}. If those same solution concentrations were used in the present study, then the relative ratios of magnesium and calcium would be very different because of the higher amounts of calcium carbonate and the lower amount of solution utilized to make cement pastes (L/S = 0.50). Consequently, this study sought to determine the necessary concentration of solutions that need to control vaterite transformation into aragonite and not calcite. Ultimately, three solution concentrations (0.05 M, 0.15 M, and 0.50 M) were investigated.

The first Mg^{2+} concentration was 0.05 M, which is 25 times more concentrated than utilized by Cherkas et al. (2018). This study showed magnesium's ability to control vaterite's transformation to aragonite at a L/S = 100. After 6 hours in 0.05 M $MgCl_2$ solution, the $CaCO_3$ cement had transformed to 70 percent calcite and had 30 percent remaining vaterite. After 1 day, almost all vaterite (99 percent) had transformed into calcite (Figure 3.9). The XRD patterns and Rietveld refinement can be found in Appendix: A.3 and Appendix: A.4 for transformation at 6 hours and 1 day, respectively. The concentration of Mg^{2+} is a critical factor in the inhibition of transformation to calcite and promotes aragonite's growth. At lower liquid to solid ratios (i.e. L/S = 0.50) a 0.05 M Mg^{2+} solution concentration was insufficient to prevent the vaterite from transforming to calcite, despite being 25 times more concentrated than in prior studies (L/S ~ 100). However, comparing Figure 3.9 to Figure 3.7, it becomes evident that the presence of Mg^{2+} is having an effect and is slowing the transformation of vaterite to calcite. For instance, at 6 hours in DI water, the vaterite had transformed to 80 percent calcite, whereas, at 6 hours in 0.05 M Mg^{2+} solution, the vaterite had transformed to 70 percent calcite.

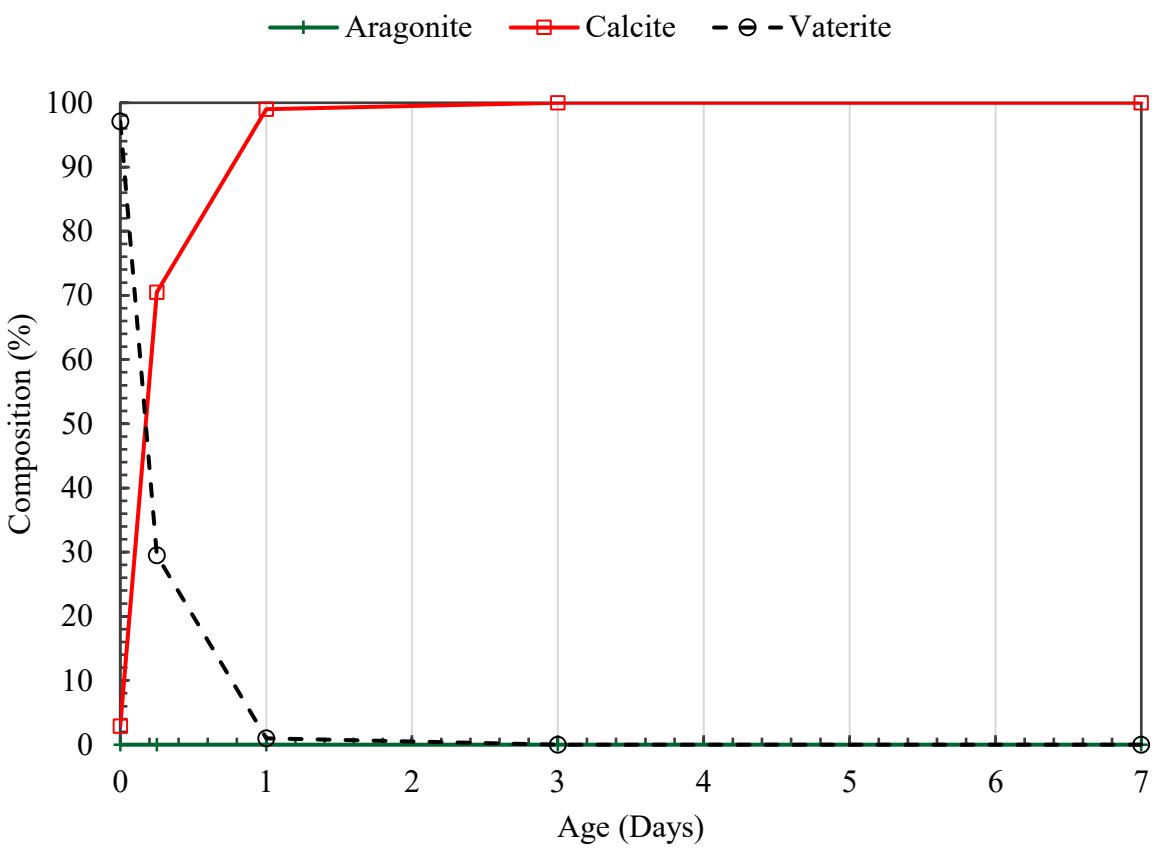

Figure 3.9 Transformation of vaterite 0.05 M Mg^{2+} solution

Since 0.05 M Mg^{2+} solution was insufficient to inhibit transformation to calcite. A solution of 0.15 M Mg^{2+} was tested. 0.15 M Mg^{2+} solution produces aragonite phase fractions of approximately 10, 42, 72, and 75 percent after 6 hours, 1, 3, and 7 days, respectively (Figure 3.10). The corresponding XRD patterns and Rietveld refinements can be found in Appendix: A.5 - Appendix: A.8. The relatively low amount of calcite remained unchanged over time, while the vaterite to aragonite ratio decreased, indicating the inhibition of additional calcite formation and the promotion of aragonite formation. Preferential adsorption of Mg^{2+} onto the surface of calcite increases the surface energy and hinders calcite's growth. Accumulation of calcite lattice strain by incorporating Mg^{2+} into the calcite lattice increases the solubility of calcite and hinders the transformation of vaterite to calcite (Gutjahr et al., 1996). The denser crystal structure of aragonite

hinders the accumulation of Mg^{2+} into aragonite (Boon et al., 2020). Therefore, precipitation of aragonite occurs following Oswald's rule. In the first 6 hours, a slower transformation of vaterite to aragonite is observed because the transformation rate is limited by the rate of nucleation and aragonite growth since no aragonite seeds were present initially. Between 6 hours and 1 day, the transformation rate accelerates before it begins to decline again. Beyond 1 day, the transformation rate declines as the abundance of vaterite declines, and its dissolution becomes the rate-controlling step. As the concentration of Mg^{2+} increased from 0.05 to 0.15 M, the amount of vaterite remaining at 1 day increased from 30 to 80 percent, indicating the increasing Mg^{2+} concentration further reduced the vaterite transformation rate.

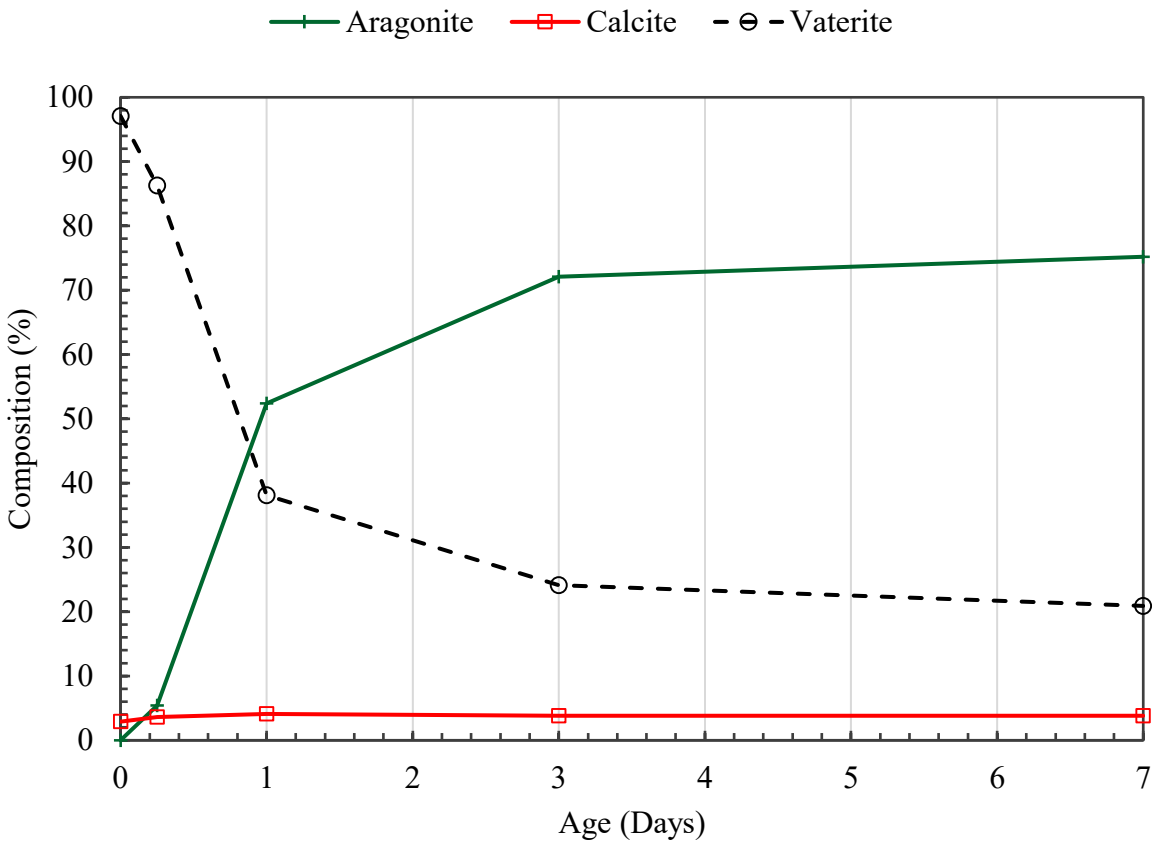

Figure 3.10 Transformation of vaterite 0.15 M Mg^{2+} solution.

The 0.50 M Mg^{2+} solution produced aragonite phase fractions of approximately 4, 39, 64, and 67 percent after 6 hours, 1, 3, and 7 days, as shown in Figure 3.11. Additionally, the calcite concentration remained below 4 percent, indicating that additional calcite formation was still sufficiently inhibited. Moreover, at 1 day, 43 percent vaterite remained, which clearly identifies that increasing Mg^{2+} concentration slows the vaterite transformation. The corresponding XRD patterns and Rietveld refinements can be found in Appendix: A.9 - Appendix: A. 12 for all time points.

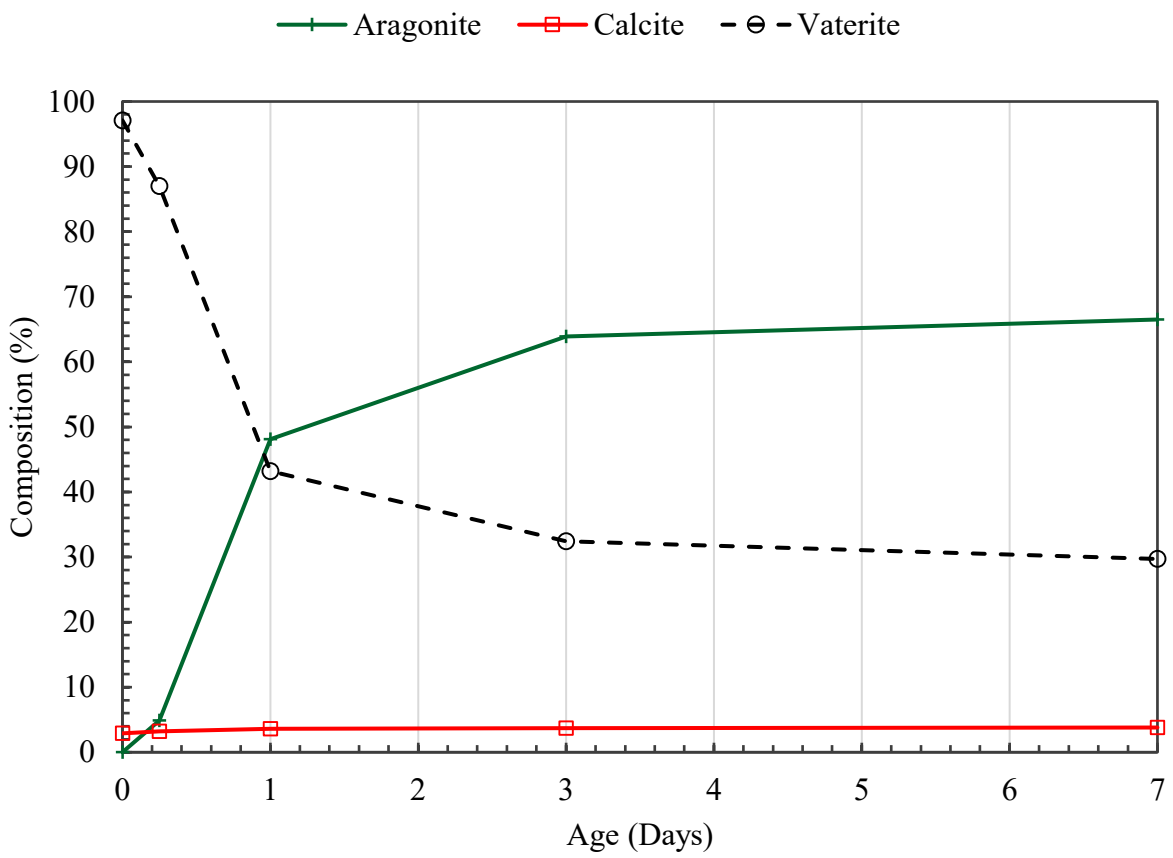

Figure 3.11 Transformation of vaterite 0.50 M Mg^{2+} solution.

Figure 3.12 further illustrates the stabilizing effect that Mg^{2+} ions have on vaterite transformation. At all timepoints observed in this set of experiments, a higher concentration of Mg^{2+} ions led to a higher amount of untransformed vaterite. This has important practical

considerations since when compared to Portland cement, $CaCO_3$ cement has relatively slow early age reaction kinetics. Consequently, a practitioner utilizing $CaCO_3$ cement would want to use a high enough Mg^{2+} concentration to sufficiently inhibit additional calcite formation, but not so much as to overly retard the transformation of vaterite to aragonite. In other words, it is desirable for the transformation of $CaCO_3$ metastable phase to aragonite cement to occur as quickly as possible.

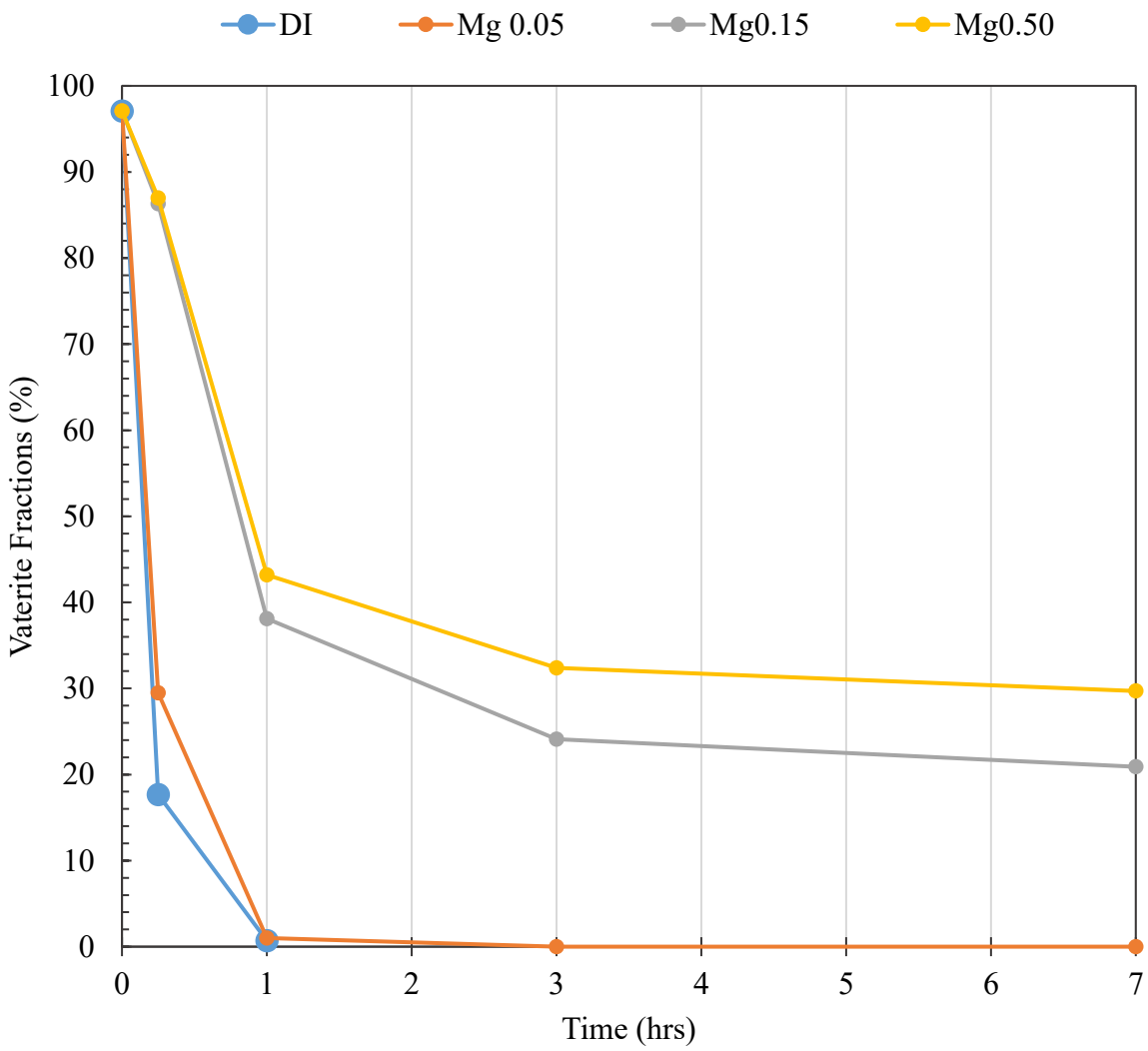

Figure 3.12 Decrease of vaterite transformation rate with the increase of Mg^{2+} concentration.

Figure 3.13 compares the rate of aragonite formation with varying Mg^{2+} concentrations. As previously shown, a minimum concentration of Mg^{2+} ion is necessary to inhibit calcite formation and therefore promote aragonite formation. However, as the Mg^{2+} concentration increases, less aragonite is produced at each point in time, indicating that increasing Mg^{2+} concentrations retards vaterite transformation to aragonite. Bischoff (1968) also observed similar findings and reported that higher concentration mildly inhibited aragonite formation. However, at earlier time points (especially 6 hours), the differences are not as significant. Both 0.15 and 0.50 M concentrations show slower transformation kinetics between 0 and 6 hours than between 6 hours and 1 day. Again, the slower formation kinetics of initial aragonite nucleation probably causes the delay. However, once aragonite exists in the system, the aragonite crystals help transform vaterite to aragonite by providing additional surfaces to precipitate, and an increase in the transformation rate results. This has practical implications for $CaCO_3$ cement. By including aragonite seed crystals in the $CaCO_3$ cement blend, then it may be possible to accelerate the initial transformation rate, which would reduce the amount of time that it takes the $CaCO_3$ cement paste to harden (set).

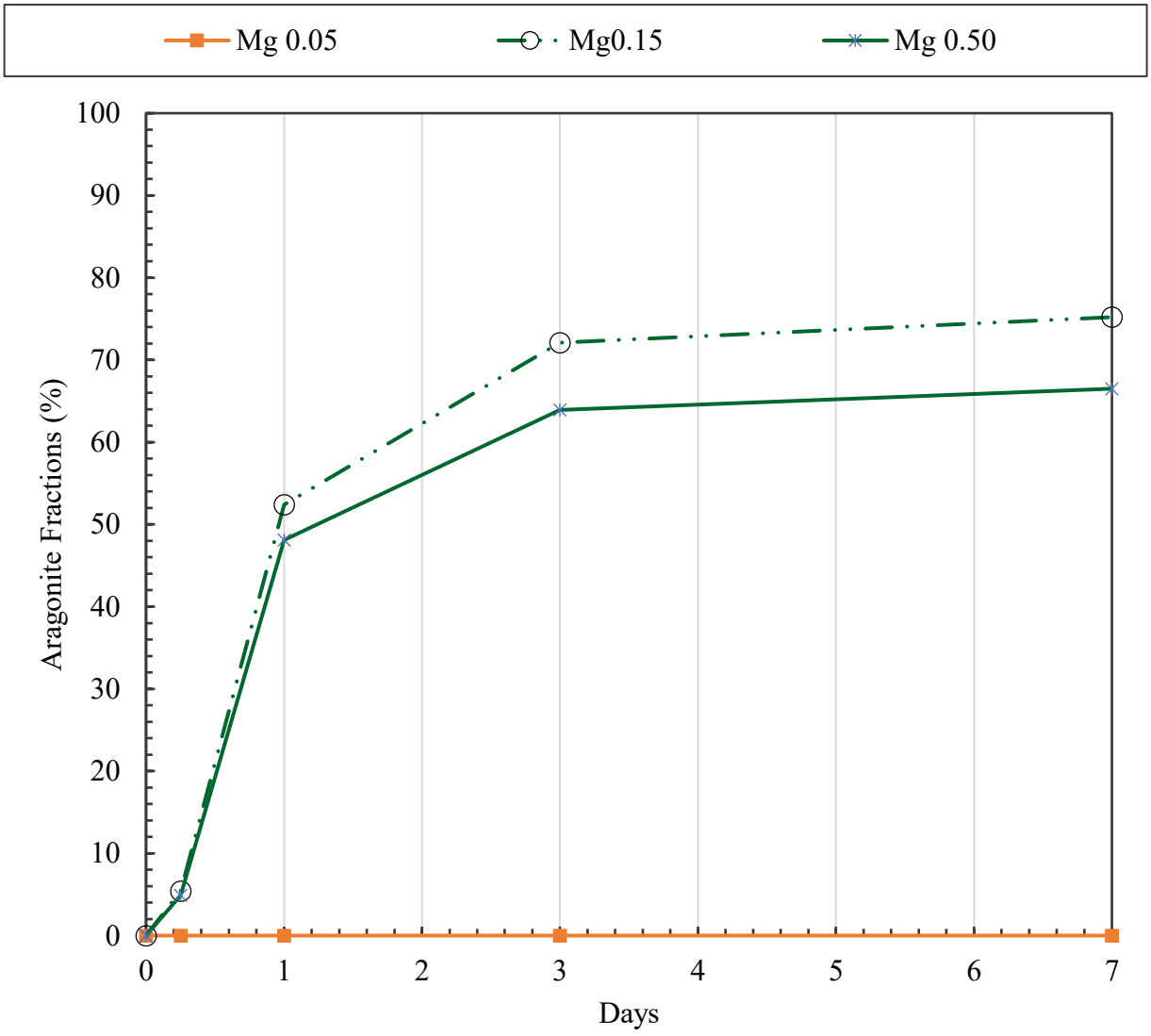

Figure 3.13 Transformation from vaterite to aragonite over time in different Mg^{2+} concentrations.

3.3.3 Transformation in Mg^{2+} and Sr^{2+} solution

Prior research has shown that, in dilute suspensions, Sr^{2+} ions promote aragonite formation. To study the effect of Sr^{2+} ions in $CaCO_3$ cement pastes with low L/S (0.5), a solution containing 0.15 M Mg^{2+} and 0.05 M Sr^{2+} was investigated. The $CaCO_3$ cement paste containing Sr^{2+} produced aragonite fractions of approximately 13.4 percent, 73 percent, 95 percent, and 95 percent at 6 hours, 1, 3, and 7 days, respectively (Figure 3.14), which is comparably higher than the solutions

containing only 0.15 M Mg^{2+}. The experimental and calculated XRD patterns are in Appendix: A. 13 - Appendix: A. 16, and the acicular particle morphology can be seen in Figure 3.15.

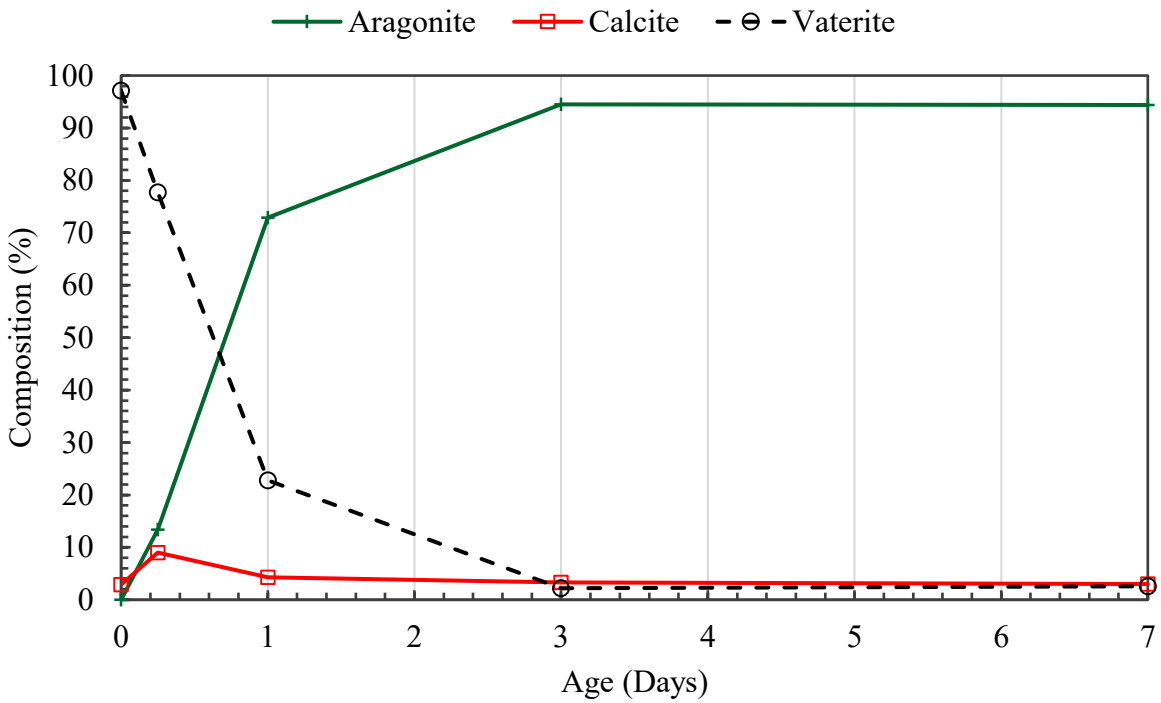

Figure 3.14 Transformation of vaterite in 0.15 M Mg^{2+} and 0.05 M Sr^{2+} solution.

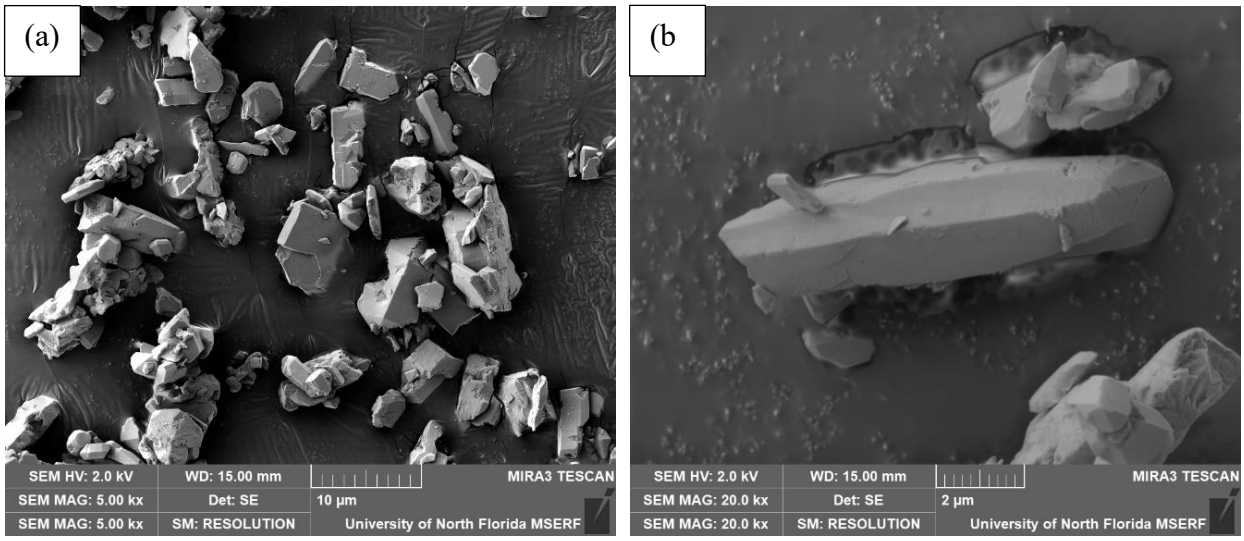

Figure 3.15 a) SEM images of grinded hardened cement powder; b) Elongated acicular morphology of aragonite crystal.

Figure 3.16 illustrates the faster dissolution of vaterite in the presence of Sr^{2+} ions. The higher coordination number of Sr^{2+} (9) compared to Ca^{2+} (6 for calcite) and a bigger ionic radius of Sr^{2+} attract more CO_3^{2-} to form $SrCO_3$ (Plummer et al., 1982). Sr^{2+} ions can catalyze aragonite formation if the Sr^{2+} ions' concentration is sufficient for SrCO3 formation, which can seed the aragonite's precipitation providing an aragonite-like crystal habit (Bischoff, 1968). The presence of higher amounts of aragonite indicates that 0.05 M Sr^{2+} can promote aragonite formation (Figure 3.17).

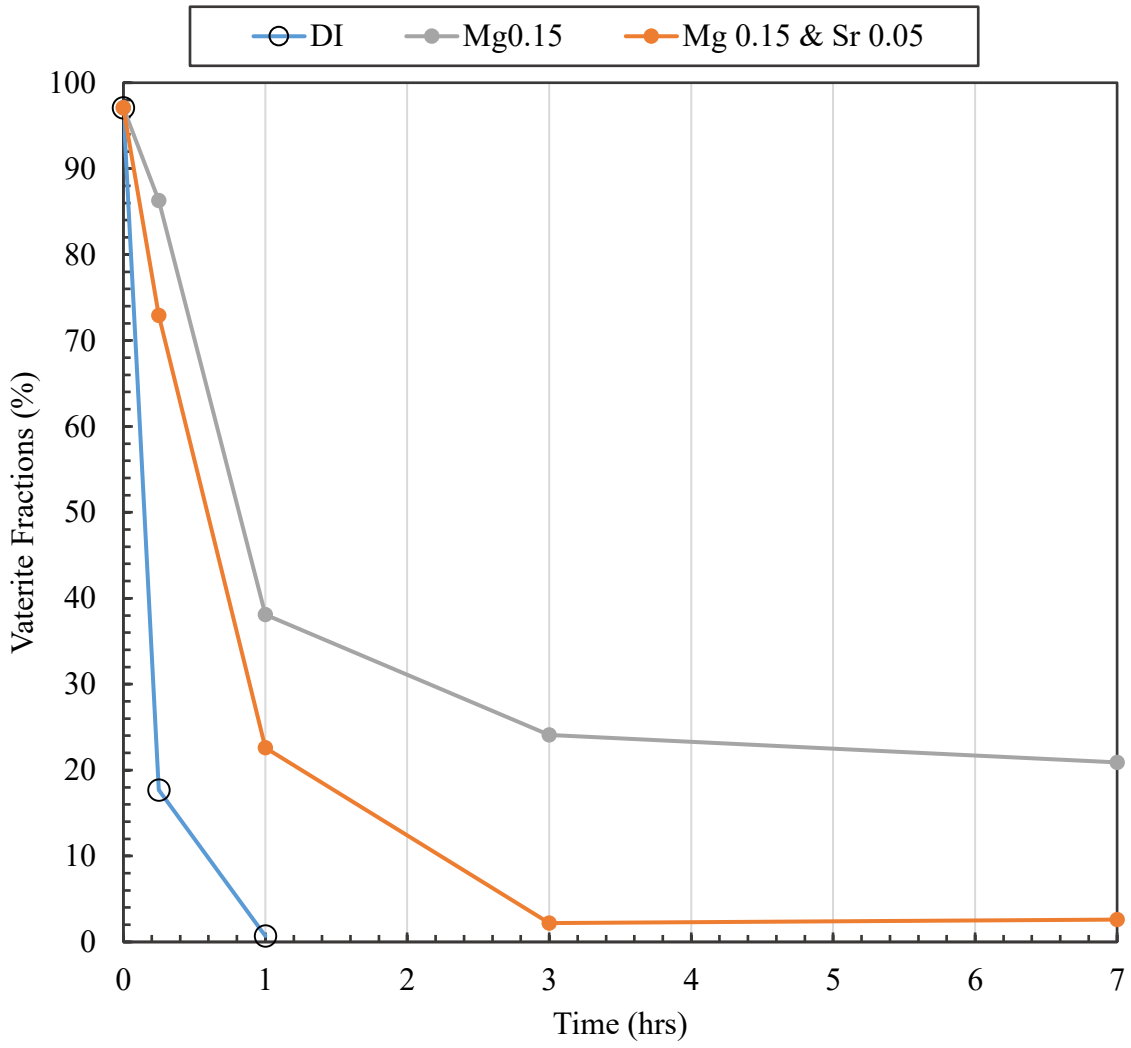

Figure 3.16 Effect of Mg^{2+} and/or Sr^{2+} ions on the transformation rate of vaterite.

In contrast to the cement paste that contained Mg^{2+} ions only, no initial delay was observed before 6 hrs. This is evidenced by the nearly straight line between 0 and 1 day, as shown in Figure 3.17 for the 0.15 M Mg^{2+} and 0.05 M Sr^{2+} cement paste. Plummer et al. (1982) reported that the formation of $SrCO_3$ was faster than aragonite/calcite formation. Therefore, vaterite dissolution was the controlling step in the transformation reaction. Incorporating Sr^{2+} into the mix solution can significantly accelerate aragonite formation and decrease the required time for $CaCO_3$ cement pastes to harden.

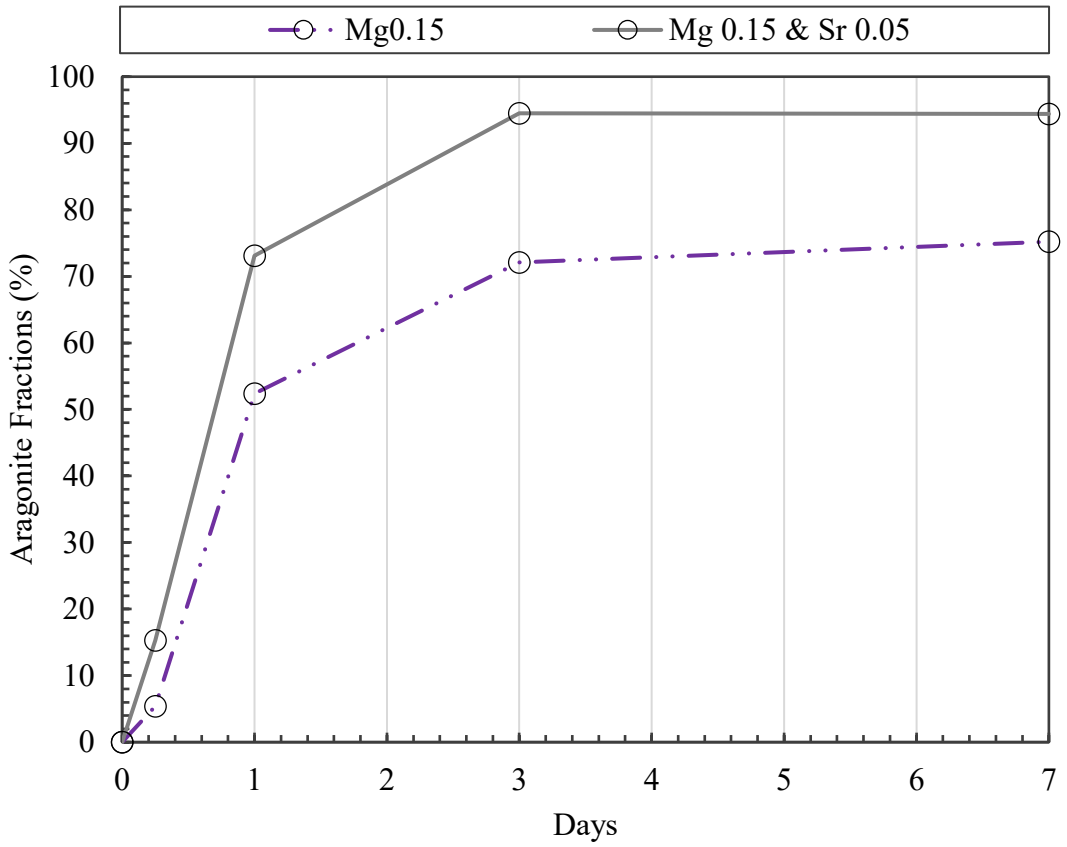

Figure 3.17 Transformation from vaterite to aragonite over time.

3.4 Effect of divalent ions on the crystal lattice of calcite and aragonite

A decrease in the lattice parameter of the c axis is observed with the increase of Mg^{2+} 17.054, 17.049, 17.036, and 17.030 Å was found for DI, 0.05 Mg^{2+}, 0.15 M Mg^{2+}, and 0.050 M

Mg^{2+}, respectively (Table 3.2, Appendix: A. 17, Appendix: A. 19, Appendix: A. 21). The shorter cell parameters of calcite are probably from the incorporation of Mg^{2+} (0.72 Å) into calcite, which has a smaller ionic radius to Ca^{2+} (Myszka et al., 2019). However, for Sr^{2+} incorporated Mg^{2+} solution, an increase in lattice parameters in all axis. Saito et al. (2020) also reported that the incorporation of Sr^{2+} ions increases the lattice parameter of calcite crystal, see Appendix: A. *23*.

The incorporation of Mg^{2+} ions hinders the growth of aragonite crystals. As shown in Figure 3.18 (a and b), a decrease in the lattice parameters is observed with increased Mg^{2+} concentration. Fermani et al. (2017) also observed similar effects on the lattice parameters and reported the replacement of Ca^{2+} ions by Mg^{2+} ions at the surface site probably caused this negative effect on aragonite lattice. However, the incorporation of Sr^{2+} ions can alleviate the negative effect of Mg^{2+} (Boon et al., 2019). For the Sr^{2+} incorporated Mg^{2+} case, an increase in lattice parameters along all axis is observed compared to the Mg^{2+} case. The use of low Mg^{2+} ions with high Sr^{2+} may favor the lattice parameters growth.

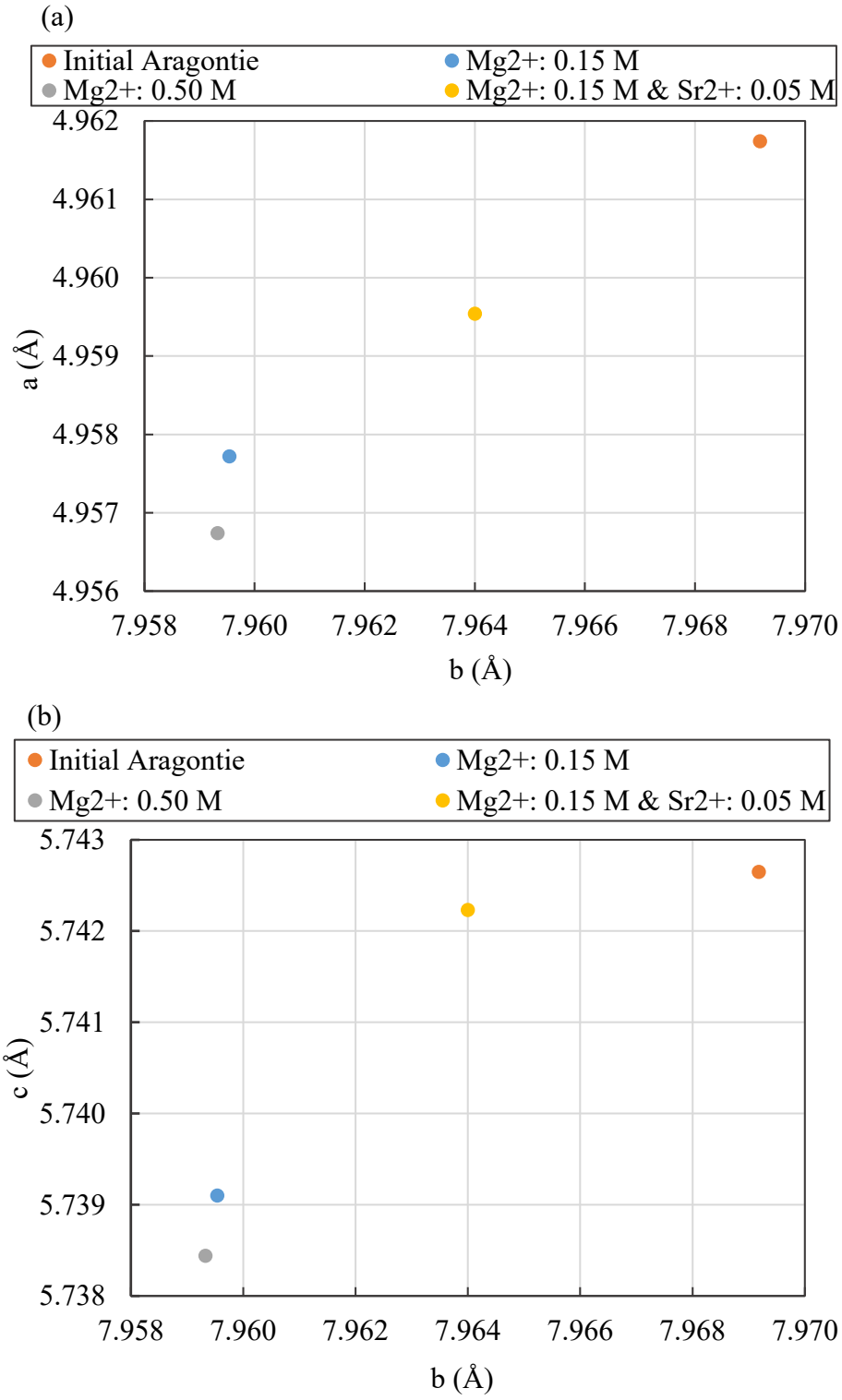

Figure 3.18 Effect of Mg^{2+} and Sr^{2+} ions on the aragonite lattice parameters at 7 days, (a) a and b axis, (b) c and a axis.

3.5 Role of divalent ions on compressive strength development

3.5.1 Strength development in DI water

To study the development of the mechanical properties of $CaCO_3$ cement pastes produced with DI water, compressive strength testing was performed at various curing timepoints (1, 3, and 7 days), and the results are shown in Figure 3.19. The compressive strength remained relatively unchanged between 1, 3, and 7 days, approximately 0.07 MPa. The mechanical properties of the cement paste did not change after 1 day because the vaterite in the $CaCO_3$ cement paste had already transformed to calcite by 1 day as evidence by XRD, see Figure 3.7. Rhombohedral calcite crystals cannot interlock as well as aragonite needles in porous systems like $CaCO_3$ cement pastes with a L/S = 0.5, and the result is lower compressive strengths.

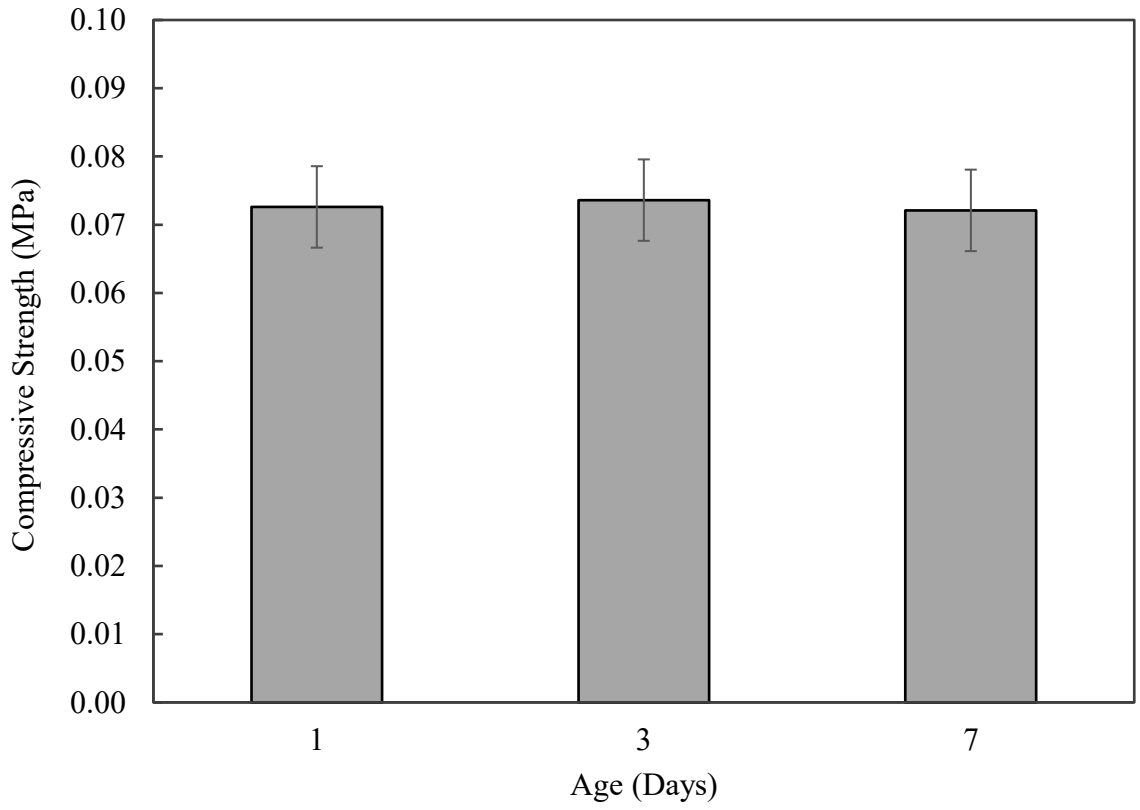

Figure 3.19 Compressive strength of $CaCO_3$ cement pastes made with DI water at different ages. Compressive strength remains relatively unchanged despite increased curing time.

3.5.2 Strength development in Mg^{2+} solution

To understand the effect that changing the concentration of Mg^{2+} ions had on the strength development of $CaCO_3$ cement pastes, $CaCO_3$ cement pastes with three different Mg^{2+} concentrations (0.05, 0.15, and 0.5 M) were tested in compression at 1, 3 and 7 days. For $CaCO_3$ cement pastes made with 0.05 M Mg^{2+}, the compressive strength was measured to be 0.06 MPa after 1 day (Figure 3.20), which is slightly lower than the compressive strength of the $CaCO_3$ cement paste made with DI water. No further compressive strength testing was performed because almost no untransformed vaterite remained after 1 day, as evidenced by XRD, see Figure 3.9. Therefore, it is expected that no change in compressive strength will occur beyond this time point.

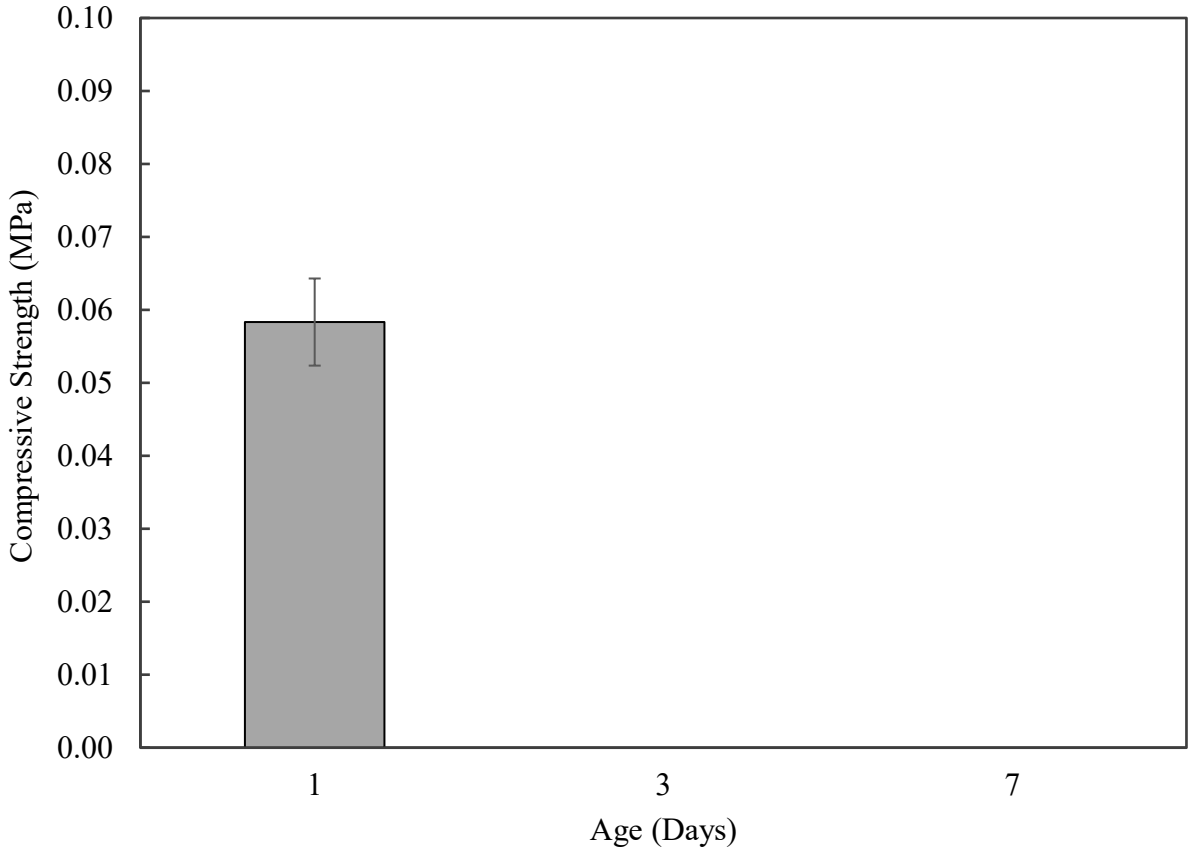

Figure 3.20 Compressive strength of $CaCO_3$ cement pastes made with 0.05 M Mg^{2+}.

When the Mg^{2+} concentration was increased to 0.15 M, an increase in compressive strength was observed with curing age, as shown in Figure 3.21. On average, compressive strengths of 0.72 MPa, 0.78 MPa, and 0.95 MPa were found on 1, 3, and 7 days. At 0.15 M Mg^{2+}, the average strengths are approximately 10 times higher than $CaCO_3$ cement pastes made with 0.05 M Mg^{2+}. Calcite and aragonite were the major $CaCO_3$ phases after transformation for 0.05 M and 0.15 M Mg^{2+} cases, respectively. It is believed that the acicular aragonite in the hardened cement provides better interlocking than the rhombohedral calcite. This hypothesis is reinforced by the trend of increasing compressive strength with increasing aragonite content of the hardened cement pastes. Increasing strength with increasing aragonite content can be observed over time as the vaterite transforms to aragonite (Figure 3.10 and Figure 3.21).

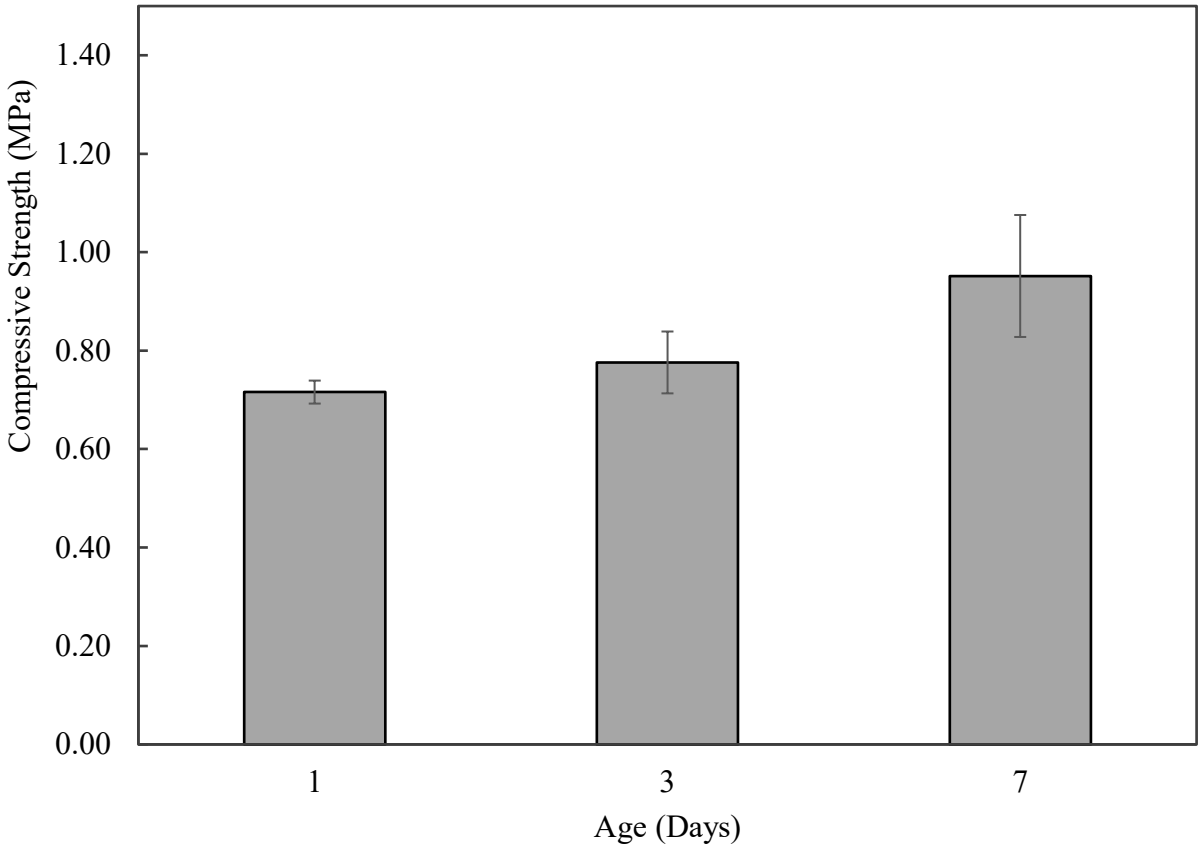

Figure 3.21 Compressive strength of $CaCO_3$ cement pastes made with 0.15 M Mg^{2+}.

When $CaCO_3$ cement pastes are made with 0.50 M Mg^{2+}, the measured average compressive strengths at 1, 3, and 7 days were 0.32 MPa, 0.78 MPa, and 0.78 MPa, as shown in Figure 3.21. No change in compressive strengths was observed between 3 and 7 days, due to the lack of aragonite variation during this period. Comparing Figures 3.21 and 3.22, it is observed that the $CaCO_3$ cement pastes made with 0.5 M Mg^{2+} has slower mechanical property development compared to the $CaCO_3$ cement pastes made with 0.15 M Mg^{2+}. The analysis of XRD results can explain this (Figure 3.12 and Figure 3.13); the higher concentration of Mg^{2+} is retarding the vaterite dissolution and aragonite formation.

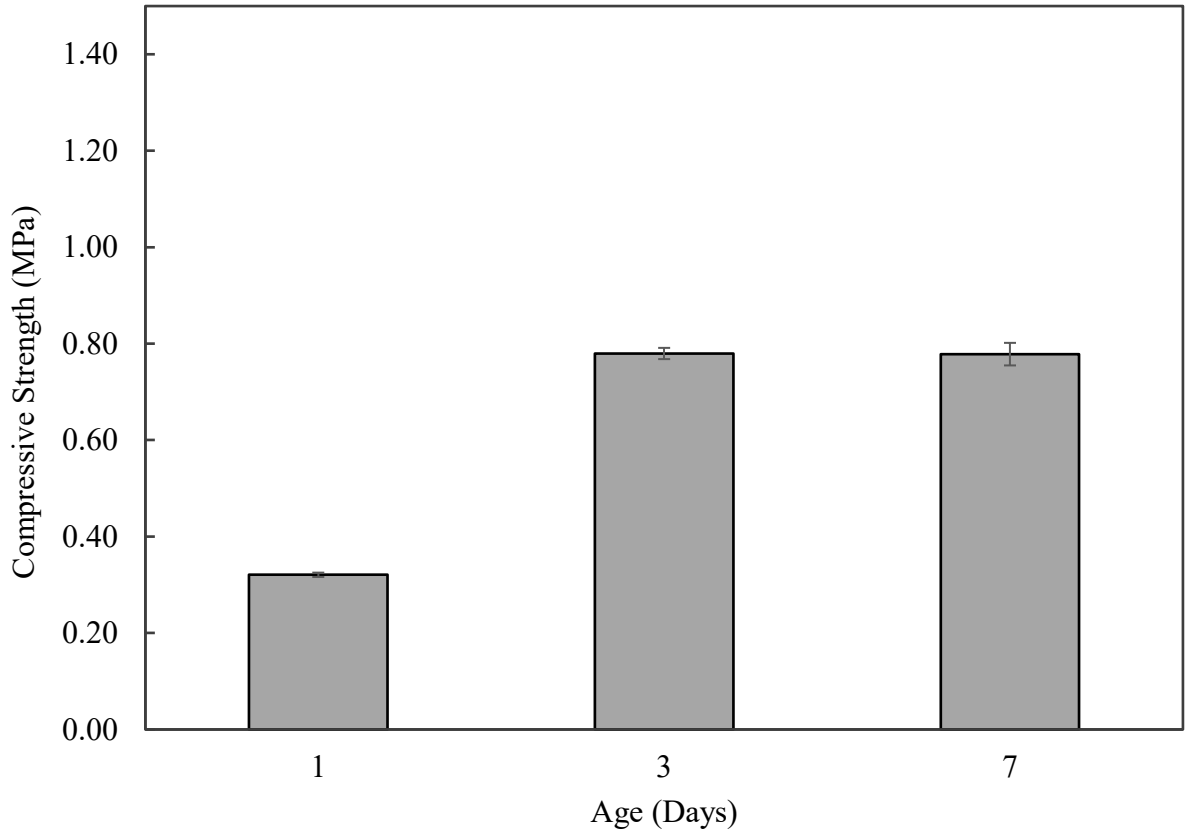

Figure 3.22 Compressive strength of $CaCO_3$ cement pastes made with 0.50 M Mg^{2+}.

3.5.3 Strength development in Mg^{2+} and Sr^{2+} solution

To study the effect of Sr^{2+} ions on the mechanical property development of $CaCO_3$ cement pastes, the compressive strength of $CaCO_3$ cement pastes made with 0.15 M Mg^{2+} and 0.05 M Sr^{2+} were tested at 1, 3, and 7 days of curing. An increase in compressive strength was observed over time (Figure 3.23). On average, compressive strengths of 0.87 MPa, 0.94 MPa, and 1.02 MPa were found for 1, 3, and 7 days, which is higher than the corresponding 0.15 M Mg^{2+} pastes (Figure 3.21). The maximum individual compressive strength is 1.11 MPa. The maximum measured compressive strength occurred at 7 days, which was achieved for the highest amount of aragonite.

Again, this reinforces the hypothesis that vaterite transformation to aragonite instead of calcite results in superior mechanical properties.

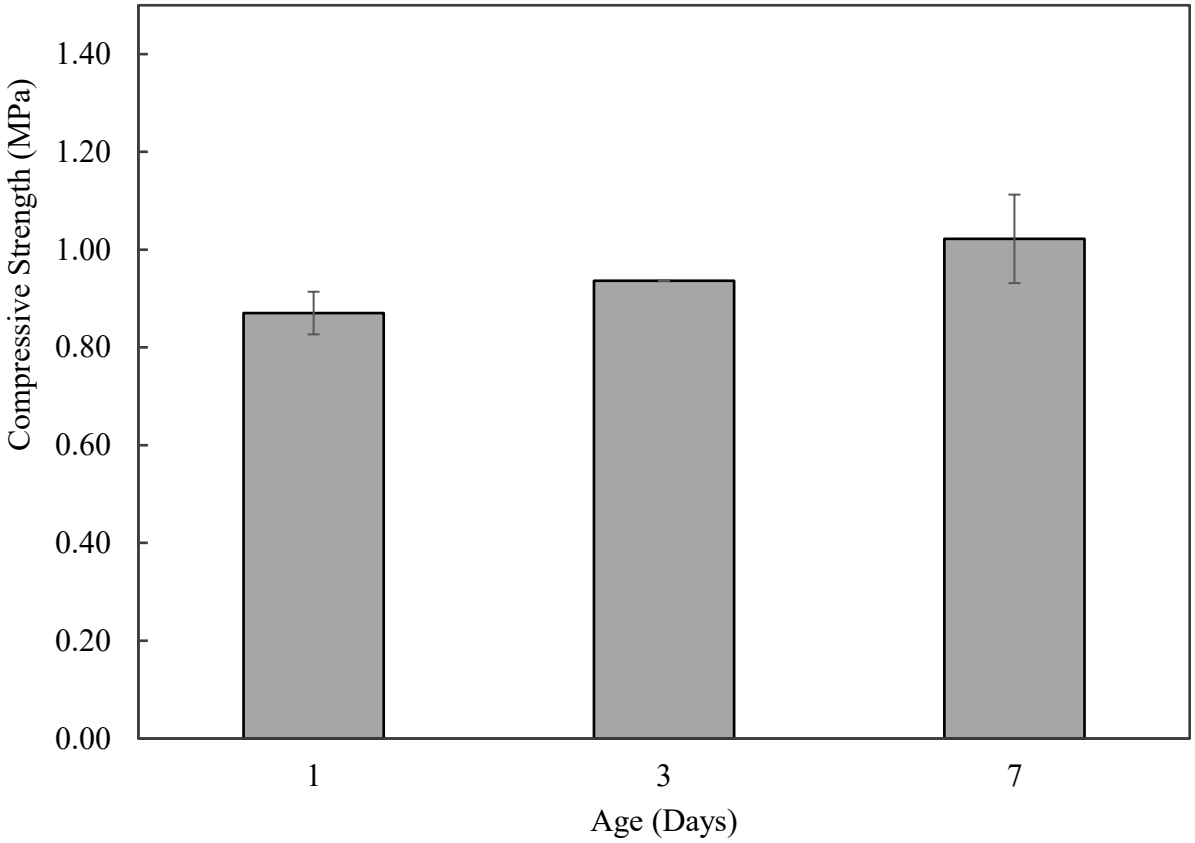

Figure 3.23 Compressive strength of $CaCO_3$ cement pastes made with 0.15 M Mg^{2+} and 0.05 M Sr^{2+}.

3.6 Relationship between compressive strength and transformed phase

Figure 3.24 shows the relationship between compressive strength and the transformed $CaCO_3$ phase. Vaterite to aragonite transformed cases exhibit almost 10 times higher compressive strength than vaterite to calcite cases. The highest compressive strength, 1.02 MPa, occurred in a $CaCO_3$ cement paste that contained 94 percent aragonite. In contrast, the lowest compressive strength 0.06 MPa occurred in a $CaCO_3$ cement paste that contained 99 percent calcite. The ascending relationship between compressive strength and aragonite fraction shows that the higher

aragonite containing $CaCO_3$ cement pastes will exhibit better compressive strengths. The approximately 50 percent aragonite containing $CaCO_3$ cement paste yields 0.78 MPa, approximately 6 times higher than the calcite only containing pastes. Evidently, the transformation of spherical vaterite agglomerates to acicular aragonite is the setting and strength development mechanism.

Additionally, prior research has shown that Sr^{2+} can promote aragonite formation with higher aspect ratios (longer), facilitating the formation of an interlocking aragonite needle network that results in higher strengths (Boon et al., 2019). This may further explain why the $CaCO_3$ cement pastes with Sr^{2+} develop a higher compressive strength; however, to support this hypothesis, additional microscopy work measuring the aspect ratios of the resulting aragonite crystals would need to be conducted. Those aragonite crystal aspect ratios would need to be correlated to the compressive strengths of the pastes.

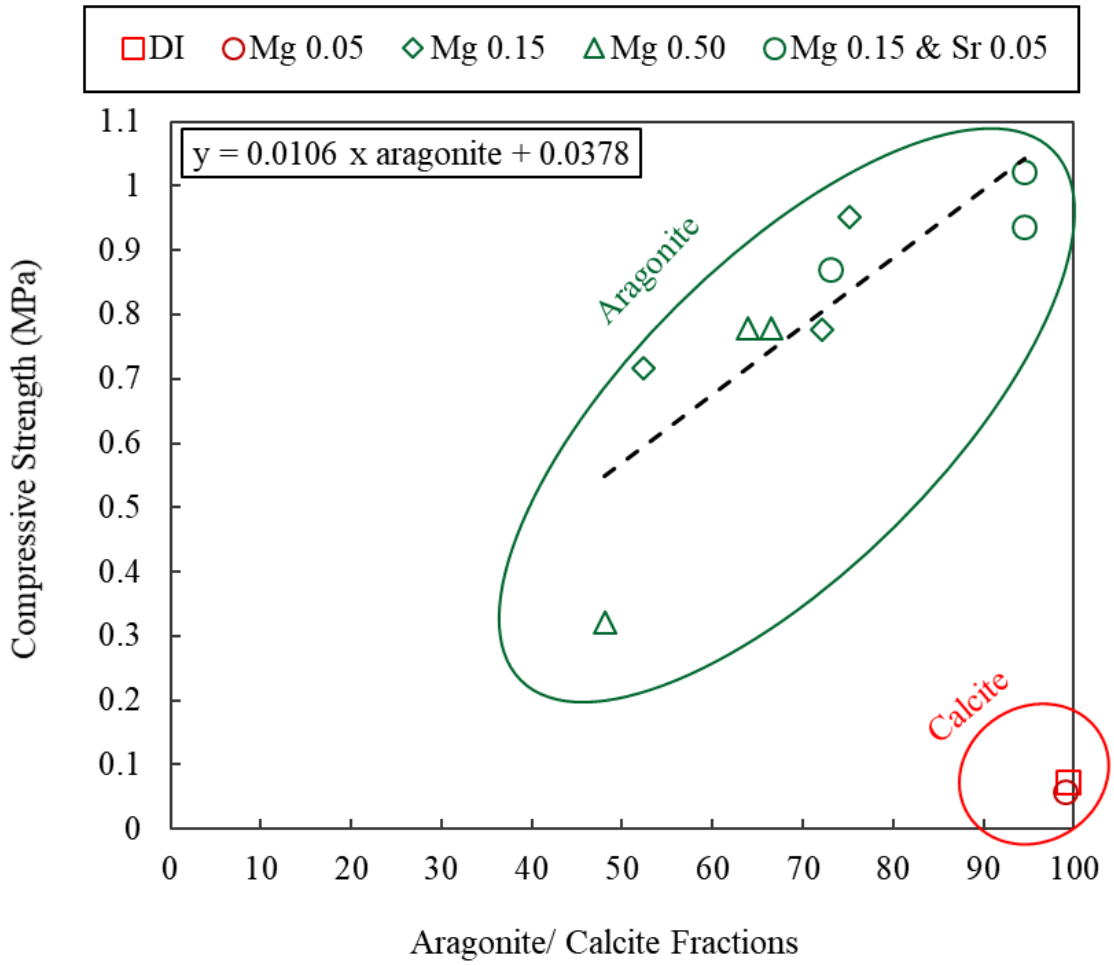

Figure 3.24 Relationship between transformed phase and mechanical strength.

Although this study adequately demonstrates that $CaCO_3$ cement pastes that transform to aragonite develop higher compressive strengths, the compressive strengths developed in this study are much less than strengths reported by Constantz et al. (2011) and Hargis et al. (2020). It appears that even though vaterite to aragonite transformation is the strength development mechanism, the magnitude of strength depends on something else. It is hypothesized that the particle size of the initial cement is affecting the microstructure that develops in the hardened cement pastes. The particle sizes of the initial cement of those studies were 25 µm and 15 µm, significantly larger than this study's mean particle size, 4.12 µm. In the study of Hargis et al. (2020), the aragonite needles appear to be nucleated on the surface of the vaterite spheres and grown out radially, producing an

interconnected network of needles as vaterite continues to dissolve and releasing Ca^{2+} and CO_3^{2-} ions that go on to precipitate on the growing aragonite needles, which have a lower solubility than vaterite (Figure 3.25 (a)). In Figure 3.25(b) and Figure 3.26, the aragonite distribution in the present study appears to be more random and evenly distributed without the same honeycombed needle network developing, as was seen by Hargis et al. (2020). It is hypothesized that the less organized microstructure lacks the interlocking of aragonite necessary to achieve optimal strength development. Additional $CaCO_3$ cements with varying particle size distributions would need to be synthesized to test this hypothesis.

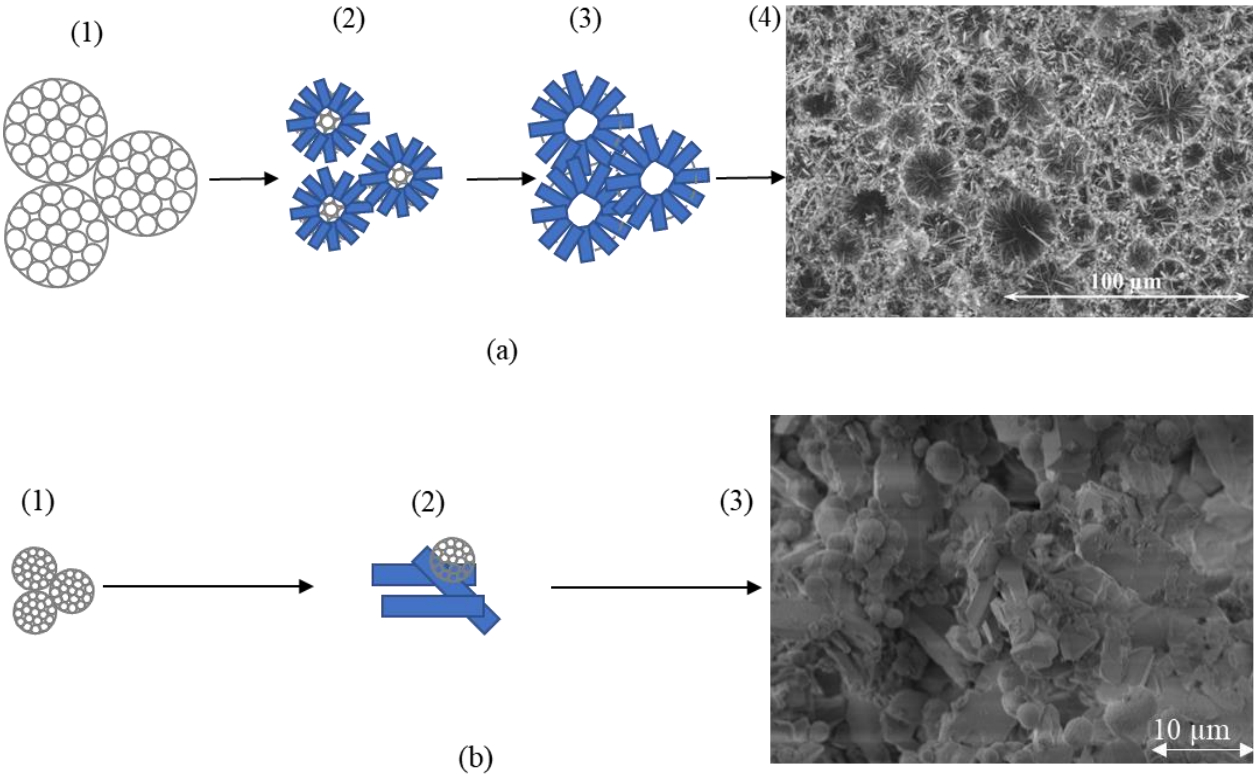

Figure 3.25 Schematic diagram illustrating the microstructure development of the hardened cement,
a. (1) Nanoaggregate micron-sized vaterite particles (15 µm) (2) Aragonite nucleation on the surface of vaterite (3-4) Aragonite grows radially and forms an interconnected microstructure (Image 4 adopted from Hargis et al.,2020);
b. (1) Nanoaggregate micron-sized vaterite particles (4.12 µm) (2) Smaller vaterite dissolved quickly and precipitates aragonite without forming a well interlocked microstructural network.

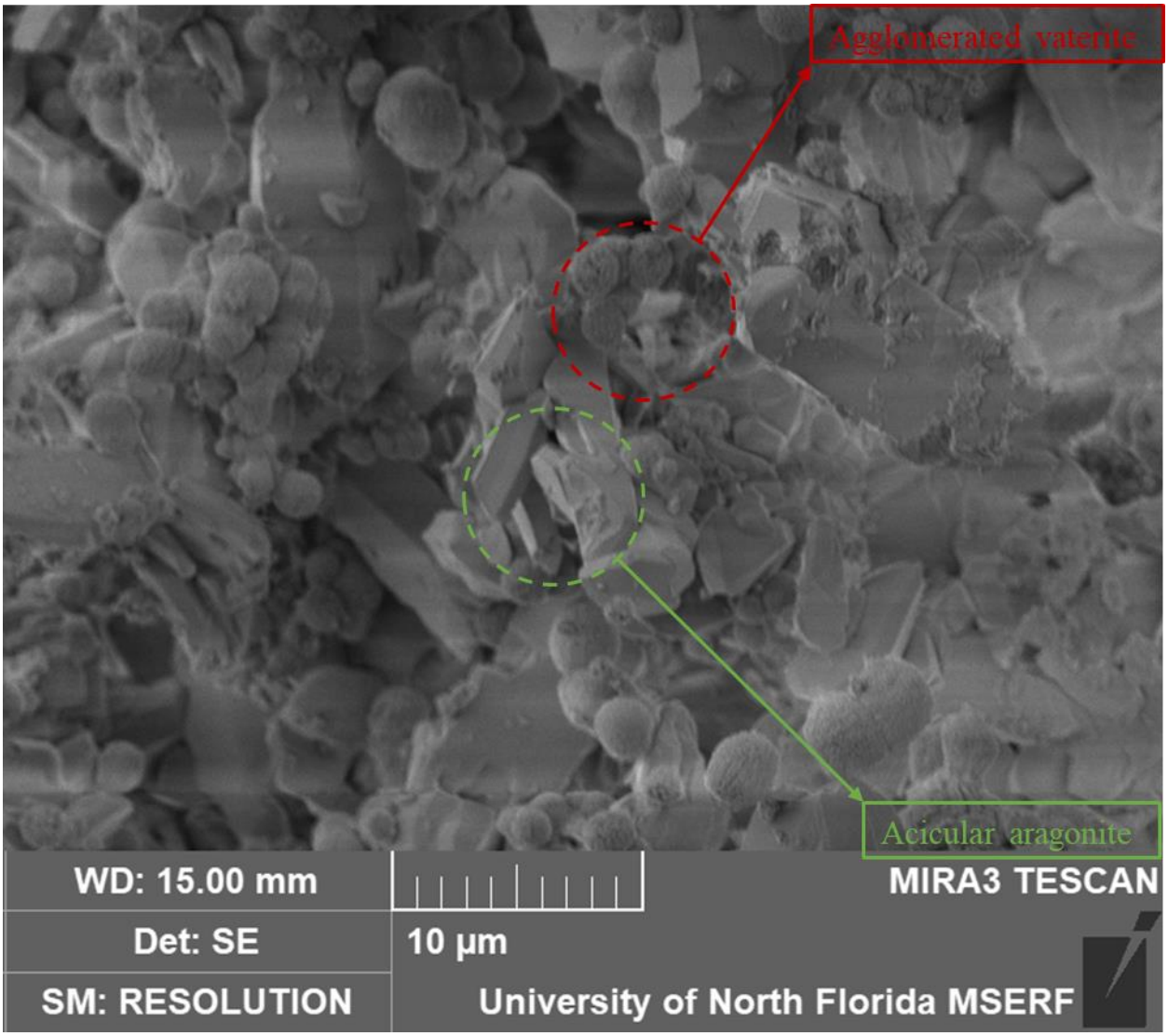

Figure 3.26 Fracture surface of compressive strength specimen of 0.50 M Mg^{2+} concentration at 7 days.

CHAPTER 4: CONCLUSIONS AND SUGGESTIONS FOR FUTURE STUDY

This study describes a method of producing a $CaCO_3$ cement, beginning with the precipitation of bulk vaterite powder for use as a starting material. Reactions of equimolar solutions of Ca^{2+} and CO_3^{2-} at room temperature (20°C) favors the precipitation of predominately vateritic $CaCO_3$. Post filtration alcohol washing and drying at 60°C helps to stabilize the vaterite. The surface morphology of the vaterite particles reveals that agglomeration of nano-sized vaterite is forming the micron sized spherical vaterite.

The cement transforms through the aqueous process, which is analogous to the curing of Portland cement. However, instead of anhydrous cement phases dissolving and precipitating hydration products, $CaCO_3$ cement hardens via the dissolution of vaterite and precipitation of aragonite or calcite without chemically binding water. Use of DI water or low concentrations of Mg^{2+} (0.05 M) solutions transform vaterite to calcite and exhibit low compressive strength. Cement pastes that transform to aragonite possess 10 times higher compressive strengths than the calcite containing hardened cement pastes. $CaCO_3$ cement pastes that contain predominantly aragonite were only found when the concentration of Mg^{2+} is 0.15 M or higher. However, increasing the concentration of Mg^{2+} hinders vaterite to aragonite transformation. In contrast, Sr^{2+} accelerated the vaterite to aragonite transformation.

The results shown here show a trend of increased compressive strength with an increase of the aragonite phase fraction after curing. However, the compressive strength of the cement was lower than anticipated, the maximum compressive strength was approximately 1.11 MPa. Using a lower liquid to powder ratio (<0.50) may enhance the compressive strength of cement. In this study, the low compressive strength is most likely related to a smaller vaterite particle size synthesized in this study (compared to others in the literature), a limitation due to the vaterite synthesis

conditions utilized in this study. Synthesis of larger vaterite spheres may yield higher compressive strengths and is a proposed topic of study for future research.

The pH neutral characteristic of the $CaCO_3$ cement may be of potential benefit for use in environmentally sensitive projects. For instance, $CaCO_3$ cement could be used in oyster and coral reef restoration projects, where lower strength binders would be acceptable, and the chemistry and pH of $CaCO_3$ cement provide it advantages over Portland cement, which is not as biocompatible. In conclusion, the developed cement in the study is not currently a suitable candidate for building construction due to its low compressive strength, but the pH neutral properties of $CaCO_3$ cement makes it a candidate for specialty applications.

REFERENCES

Andrew, R. M. (2019). Global CO_2 emissions from cement production, 1928–2018. *Earth System Science Data*, *11*(4), 1675–1710. https://doi.org/10.5194/essd-11-1675-2019

Antao, S. M., & Hassan, I. (2009). The orthorhombic structure of $CaCO_3$, $SrCO_3$, $PbCO_3$ and $BaCO_3$: Linear structural trends. *Canadian Mineralogist*, *47*(5), 1245–1255. https://doi.org/10.3749/canmin.47.5.1245

Azdarpour, A., Afkhami Karaei, M., Hamidi, H., Mohammadian, E., & Honarvar, B. (2018). CO2 sequestration through direct aqueous mineral carbonation of red gypsum. *Petroleum*, *4*(4), 398–407. https://doi.org/10.1016/j.petlm.2017.10.002

Bischoff, J. L., & Fyfe, W. S. (1968). Catalysis, inhibition, and the calcite-aragonite problem; [Part] 1, The aragonite-calcite transformation. *American Journal of Science*, *266*(2), 65–79. https://doi.org/10.2475/ajs.266.2.65

Bischoff, J. L. (1968). Catalysis, inhibition, and the calcite-aragonite problem; [Part] 2, The vaterite-aragonite transformation. *American Journal of Science*, *266*(2), 80–90. https://doi.org/10.2475/ajs.266.2.80

Blake, A. J., Cole, J. M., Evans, J. S., Main, P., Parsons, S., & Watkin, D. J. (2009). *Crystal structure analysis: principles and practice* (Vol. 13). Oxford University Press.

Boon, M., Rickard, W. D. A., Rohl, A. L., & Jones, F. (2020). Stabilization of Aragonite: Role of Mg^{2+} and Other Impurity Ions. *Crystal Growth & Design*, *20*(8), 5006–5017. https://doi.org/10.1021/acs.cgd.0c00152

Burkett, J. R., Hight, L. M., Kenny, P., & Wilker, J. J. (2010). Oysters Produce an Organic−Inorganic Adhesive for Intertidal Reef Construction. *Journal of the American Chemical Society*, *132*(36), 12531–12533. https://doi.org/10.1021/ja104996y

Chang, R., Kim, S., Lee, S., Choi, S., Kim, M., & Park, Y. (2017). Calcium carbonate precipitation for CO_2 storage and utilization: A review of the carbonate crystallization and polymorphism. In *Frontiers in Energy Research* (Vol. 5, Issue JUL, p. 1). Frontiers Media S.A. https://doi.org/10.3389/fenrg.2017.00017

Chen, J., & Xiang, L. (2009). Controllable synthesis of calcium carbonate polymorphs at different temperatures. *Powder Technology*, *189*(1), 64–69. https://doi.org/10.1016/j.powtec.2008.06.004

Cherkas, O., Beuvier, T., Zontone, F., Chushkin, Y., Demoulin, L., Rousseau, A., & Gibaud, A. (2018). On the kinetics of phase transformations of dried porous vaterite particles immersed in deionized and tap water. *Advanced Powder Technology*, *29*(11), 2872–2880. https://doi.org/10.1016/j.apt.2018.08.008

Combes, C., Bareille, R., & Rey, C. (2006). Calcium carbonate–calcium phosphate mixed cement compositions for bone reconstruction. *Journal of Biomedical Materials Research Part A*, *79A* (2), 318–328. https://doi.org/10.1002/jbm.a.30795

Combes, C., Miao, B., Bareille, R., & Rey, C. (2006). Preparation, physical–chemical characterisation and cytocompatibility of calcium carbonate cements. *Biomaterials*, *27*(9), 1945–1954. https://doi.org/10.1016/j.biomaterials.2005.09.026

Combes, C., Tadier, S., Galliard, H., Girod-Fullana, S., Charvillat, C., Rey, C., Auzély-Velty, R., & El Kissi, N. (2010). Rheological properties of calcium carbonate self-setting injectable paste. *Acta Biomaterialia*, *6*(3), 920–927. https://doi.org/10.1016/j.actbio.2009.08.032

Constantz, B. R., Farsad, K., Camire, C., Patterson, J., Fernandez, M., Yaccato, K., ... & Hodson, K. (2012). *U.S. Patent No. 8,114,214*. Washington, DC: U.S. Patent and Trademark Office.

Dhami, N. K., Reddy, M. S., & Mukherjee, A. (2013). Biomineralization of calcium carbonates and their engineered applications: a review. *Frontiers in Microbiology*, *4*(OCT). https://doi.org/10.3389/fmicb.2013.00314

Farfan, G. A., Cordes, E. E., Waller, R. G., DeCarlo, T. M., & Hansel, C. M. (2018). Mineralogy of Deep-Sea Coral Aragonites as a Function of Aragonite Saturation State. *Frontiers in Marine Science*, *5*(DEC), 473. https://doi.org/10.3389/fmars.2018.00473

Fermani, S., Njegić Džakula, B., Reggi, M., Falini, G., & Kralj, D. (2017). Effects of magnesium and temperature control on aragonite crystal aggregation and morphology. *CrystEngComm*, *19*(18), 2451–2455. https://doi.org/10.1039/C7CE00197E

Fontaine, M.-L., Combes, C., Sillam, T., Dechambre, G., & Rey, C. (2005). New Calcium Carbonate-Based Cements for Bone Reconstruction. *Key Engineering Materials*, *284–286*, 105–108. https://doi.org/10.4028/www.scientific.net/kem.284-286.105

Gutjahr, A., Dabringhaus, H., & Lacmann, R. (1996). Studies of the growth and dissolution kinetics of the $CaCO_3$ polymorphs calcite and aragonite II. The influence of divalent cation additives on the growth and dissolution rates. *Journal of Crystal Growth*, *158*(3), 310–315. https://doi.org/10.1016/0022-0248(95)00447-5

Gutschick, K. A. (2000). Lime and Limestone. In *Kirk-Othmer Encyclopedia of Chemical Technology*. John Wiley & Sons, Inc. https://doi.org/10.1002/0471238961.1209130507212019.a01

Han, Y. S., Hadiko, G., Fuji, M., & Takahashi, M. (2006). Factors affecting the phase and morphology of $CaCO_3$ prepared by a bubbling method. *Journal of the European Ceramic Society*, *26*(4–5), 843–847. https://doi.org/10.1016/j.jeurceramsoc.2005.07.050

Hamester, M. R. R., Balzer, P. S., & Becker, D. (2012). Characterization of calcium carbonate obtained from oyster and mussel shells and incorporation in polypropylene. *Materials Research*, *15*(2), 204–208. https://doi.org/10.1590/S1516-14392012005000014

Hargis, C. W., Chen, I. A., Devenney, M., Fernandez, M. J., Gilliama, R. J., & Thatchera, R. P. (2020). *Calcium carbonate cement: A carbon capture, utilization, and storage (CCUS) technique.* Manuscript submitted for publication.

IEA (2009). *Cement Technology Roadmap: Carbon Emissions Reductions up to 2050*. IEA Technology Roadmaps. OECD Publishing. Paris, https://doi.org/10.1787/9789264088061-en.

Imai, H., Tochimoto, N., Nishino, Y., Takezawa, Y., & Oaki, Y. (2012). Oriented Nanocrystal Mosaic in Monodispersed CaCO 3 Microspheres with Functional Organic Molecules. *Crystal Growth & Design*, *12*(2), 876–882. https://doi.org/10.1021/cg201301x

Kelley, K. N. (2009). *Use of recycled oyster shells as aggregate for pervious concrete* [Master's thesis, University of Florida, Florida, USA]. Retrieved from http://etd.fcla.edu/UF/UFE0041269/kelley_k.pdf

Konopacka-Łyskawa, D. (2019). Synthesis Methods and Favorable Conditions for Spherical Vaterite Precipitation: A Review. *Crystals*, *9*(4), 223. https://doi.org/10.3390/cryst9040223

Kontoyannis, C. G., & Vagenas, N. V. (2000). Calcium carbonate phase analysis using XRD and FT-Raman spectroscopy. *The Analyst*, *125*(2), 251–255. https://doi.org/10.1039/a908609i

Le Bail, A., Ouhenia, S., & Chateigner, D. (2011). Microtwinning hypothesis for a more ordered vaterite model. *Powder Diffraction*, *26*(1), 16–21. https://doi.org/10.1154/1.3552994

Lee, M. G., Kang, D., Yoo, Y., Jo, H., Song, H. J., & Park, J. (2016). Continuous and Simultaneous CO2 Absorption, Calcium Extraction, and Production of Calcium Carbonate Using Ammonium Nitrate. *Industrial and Engineering Chemistry Research*, *55*(45), 11795–11800. https://doi.org/10.1021/acs.iecr.6b02880

Li, Q., Ding, Y., Li, F., Xie, B., & Qian, Y. (2002). Solvothermal growth of vaterite in the presence of ethylene glycol, 1,2-propanediol and glycerin. *Journal of Crystal Growth*, *236*(1–3), 357–362. https://doi.org/10.1016/S0022-0248(01)02130-3

Lombardi, S. A., Chon, G. D., Lee, J. J.-W., Lane, H. A., & Paynter, K. T. (2013). Shell Hardness and Compressive Strength of the Eastern Oyster, Crassostrea virginica, and the Asian Oyster, Crassostrea ariakensis. *The Biological Bulletin*, *225*(3), 175–183. https://doi.org/10.1086/BBLv225n3p175

Ludwig, H.-M., & Zhang, W. (2015). Research review of cement clinker chemistry. *Cement and Concrete Research*, *78*, 24–37. https://doi.org/10.1016/j.cemconres.2015.05.018

Luo, X., Song, X., Cao, Y., Song, L., & Bu, X. (2020). Investigation of calcium carbonate synthesized by steamed ammonia liquid waste without use of additives. *RSC Advances*, *10*(13), 7976–7986. https://doi.org/10.1039/c9ra10460g

Maddalena, R., Roberts, J. J., & Hamilton, A. (2018). Can Portland cement be replaced by low-carbon alternative materials? A study on the thermal properties and carbon emissions of innovative cements. *Journal of Cleaner Production*, *186*, 933–942. https://doi.org/10.1016/j.jclepro.2018.02.138

Mehta, P. K. (2002). Greening of the concrete industry for sustainable development. *Concrete international*, *24*(7), 23-28.

Miller, S. A., Horvath, A., & Monteiro, P. J. M. (2016). Readily implementable techniques can cut annual CO 2 emissions from the production of concrete by over 20%. *Environmental Research Letters*, *11*(7), 074029. https://doi.org/10.1088/1748-9326/11/7/074029

Morris, R. L., Bilkovic, D. M., Boswell, M. K., Bushek, D., Cebrian, J., Goff, J., Kibler, K. M., La Peyre, M. K., McClenachan, G., Moody, J., Sacks, P., Shinn, J. P., Sparks, E. L., Temple, N. A., Walters, L. J., Webb, B. M., & Swearer, S. E. (2019). The application of oyster reefs in shoreline protection: Are we over-engineering for an ecosystem engineer? *Journal of Applied Ecology*, *56*(7), 1703–1711. https://doi.org/10.1111/1365-2664.13390

Müller, W. E. G., Neufurth, M., Huang, J., Wang, K., Feng, Q., Schröder, H. C., Diehl-Seifert, B., Muñoz-Espí, R., & Wang, X. (2015). Nonenzymatic Transformation of Amorphous CaCO 3 into Calcium Phosphate Mineral after Exposure to Sodium Phosphate in Vitro: Implications for in Vivo Hydroxyapatite Bone Formation. *ChemBioChem*, *16*(9), 1323–1332. https://doi.org/10.1002/cbic.201500057

Myszka, B., Hurle, K., Zheng, K., Wolf, S. E., & Boccaccini, A. R. (2019). Mechanical improvement of calcium carbonate cements by in situ HEMA polymerization during hardening. *Journal of Materials Chemistry B*, *7*(21), 3403–3411. https://doi.org/10.1039/C9TB00237E

Naik, T. R. (2008). Sustainability of Concrete Construction. *Practice Periodical on Structural Design and Construction*, *13*(2), 98–103. https://doi.org/10.1061/(ASCE)1084-0680(2008)13:2(98)

Nebel, H., & Epple, M. (2008). Continuous Preparation of Calcite, Aragonite and Vaterite, and of Magnesium-Substituted Amorphous Calcium Carbonate (Mg-ACC). *Zeitschrift Für Anorganische Und Allgemeine Chemie*, *634*(8), 1439–1443. https://doi.org/10.1002/zaac.200800134

Nielsen, M. H., Aloni, S., & De Yoreo, J. J. (2014). In situ TEM imaging of $_{CaCO3}$ nucleation reveals coexistence of direct and indirect pathways. *Science*, *345*(6201), 1158–1162. https://doi.org/10.1126/science.1254051

Ogino, T., Suzuki, T., & Sawada, K. (1987). The formation and transformation mechanism of calcium carbonate in water. *Geochimica et Cosmochimica Acta*, *51*(10), 2757–2767. https://doi.org/10.1016/0016-7037(87)90155-4

Ondrus, P., Veselovsky, F., Gabasova, A., Hlousek, J., Srein, V., Vavrin, I., Skala, R., Sejkora, J., & Drabek, M. (2003). Primary minerals of the Jachymov ore district. *Journal of the Czech Geological Society*, *48*(3–4), 19–147.

Plummer, L. N., & Busenberg, E. (1982). The solubilities of calcite, aragonite and vaterite in CO2-H2O solutions between 0 and 90°C, and an evaluation of the aqueous model for the system $_{CaCO3}$-CO2-H2O. *Geochimica et Cosmochimica Acta*, *46*(6), 1011–1040. https://doi.org/10.1016/0016-7037(82)90056-4

Rodriguez-Blanco, J. D., Shaw, S., & Benning, L. G. (2011). The kinetics and mechanisms of amorphous calcium carbonate (ACC) crystallization to calcite, viavaterite. *Nanoscale*, *3*(1), 265–271. https://doi.org/10.1039/C0NR00589D

Rodríguez-Sánchez, J., Myszka, B., Boccaccini, A. R., & Dysthe, D. K. (2019). Setting behavior and bioactivity assessment of calcium carbonate cements. *Journal of the American Ceramic Society*, *102*(11), 6980–6990. https://doi.org/10.1111/jace.16593

Rodríguez-Sánchez, J., Liberto, T., Barentin, C., & Dysthe, D. K. (2020). Mechanisms of Phase Transformation and Creating Mechanical Strength in a Sustainable Calcium Carbonate Cement. *Materials*, *13*(16), 3582. https://doi.org/10.3390/ma13163582

Saito, A., Kagi, H., Marugata, S., Komatsu, K., Enomoto, D., Maruyama, K., & Kawano, J. (2020). Incorporation of Incompatible Strontium and Barium Ions into Calcite ($_{CaCO3}$) through Amorphous Calcium Carbonate. *Minerals*, *10*(3), 270. https://doi.org/10.3390/min10030270

Sakai, K., & Noguchi, T. (2012). The Sustainable Use of Concrete. CRC Press. https://doi.org/10.1201/b12355

Scott, L. (2012). *Reduced calcium carbonate scaling through turbulent physical conditioning*. [Doctoral dissertation, University of Wollongong, New South Wales, Australia]. Retrieved from https://ro.uow.edu.au/cgi/viewcontent.cgi?article=4834&context=theses.

Schneider, M. (2019). The cement industry on the way to a low-carbon future. *Cement and Concrete Research*, *124*, 105792. https://doi.org/10.1016/j.cemconres.2019.105792

Spanos, N., & Koutsoukos, P. G. (1998). The transformation of vaterite to calcite: effect of the conditions of the solutions in contact with the mineral phase. *Journal of Crystal Growth*, *191*(4), 783–790. https://doi.org/10.1016/S0022-0248(98)00385-6

Tai, C. Y., & Chen, F. B. (1998). Polymorphism of $_{CaCO3}$ precipitated in a constant-composition environment. *AIChE Journal*, *44*(8), 1790–1798. https://doi.org/10.1002/aic.690440810

Vagenas, N. V., Gatsouli, A., & Kontoyannis, C. G. (2003). Quantitative analysis of synthetic calcium carbonate polymorphs using FT-IR spectroscopy. *Talanta*, *59*(4), 831–836. https://doi.org/10.1016/S0039-9140(02)00638-0

Wada, N., Yamashita, K., & Umegaki, T. (1995). Effects of divalent cations upon nucleation, growth and transformation of calcium carbonate polymorphs under conditions of double diffusion. *Journal of Crystal Growth*, *148*(3), 297–304. https://doi.org/10.1016/0022-0248(94)00880-9

APPENDIX A

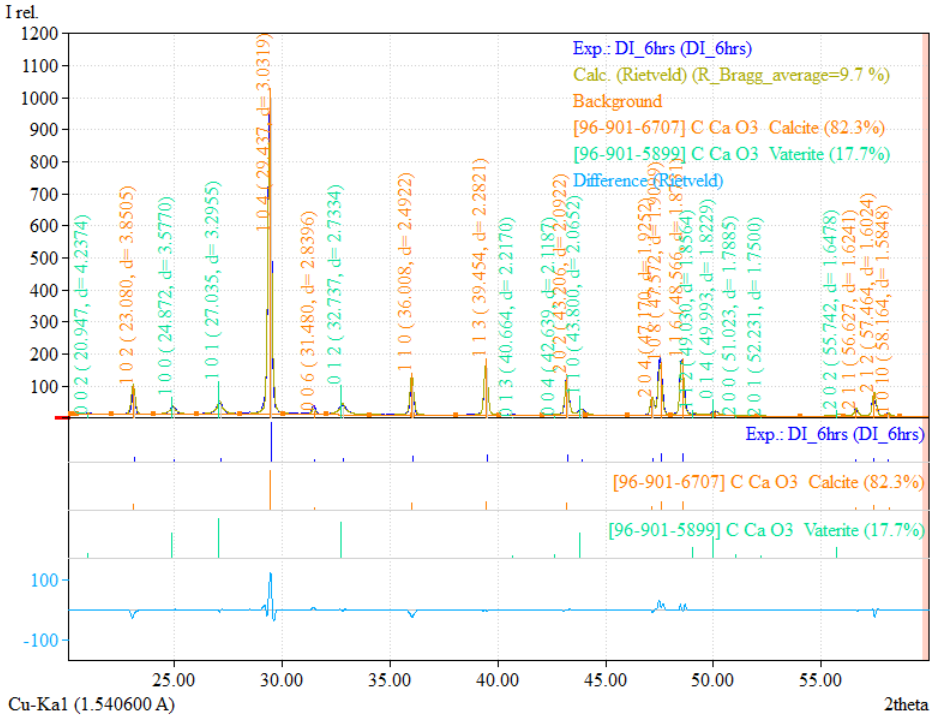

Appendix: A.1 Rietveld refinement of DI water at 6 hours.

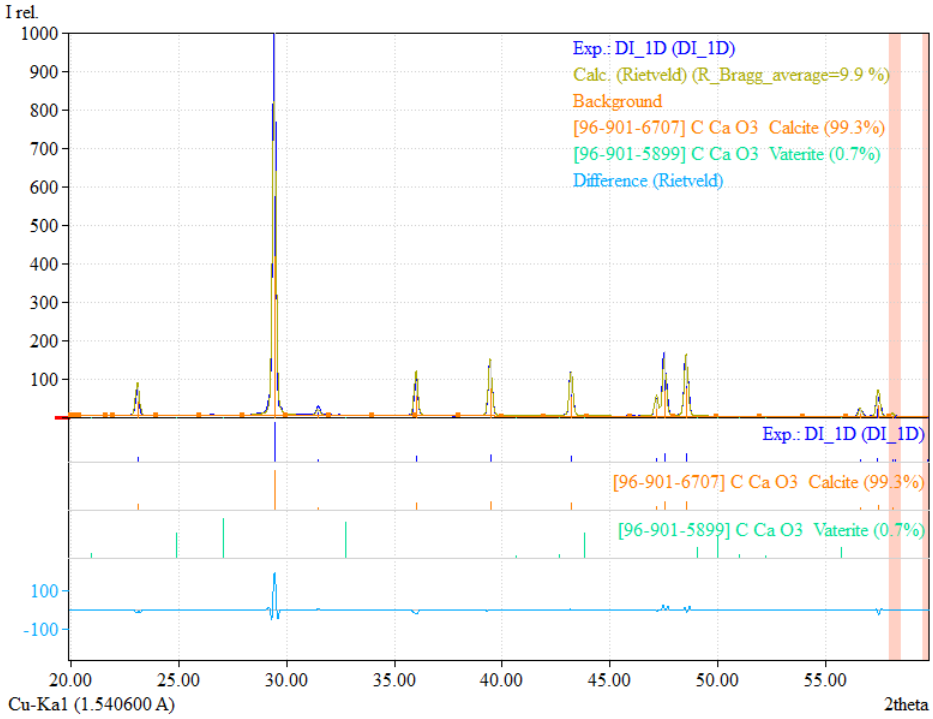

Appendix: A.2 Rietveld refinement of DI water at 1 day.

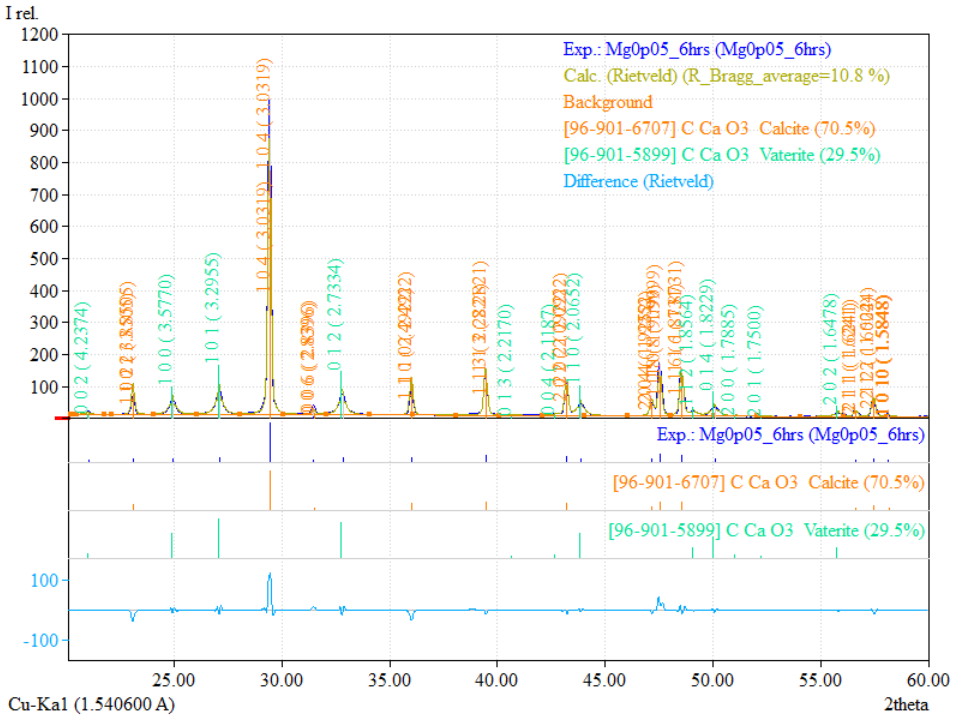

Appendix: A.3 Rietveld refinement of Mg 0.05 M solution at 6 hours.

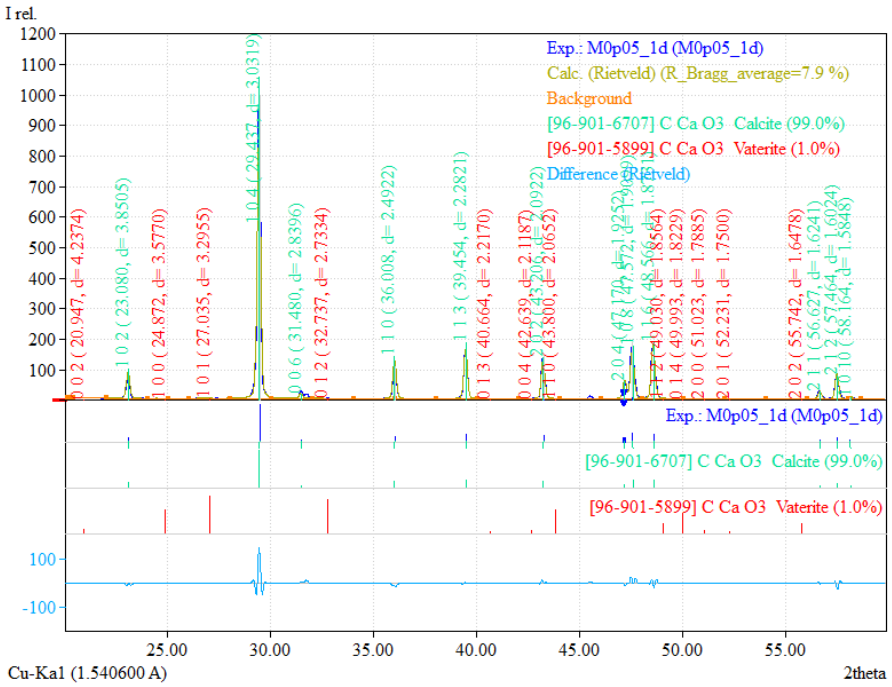

Appendix: A.4 Rietveld refinement of Mg 0.05 M solution at 1 day.

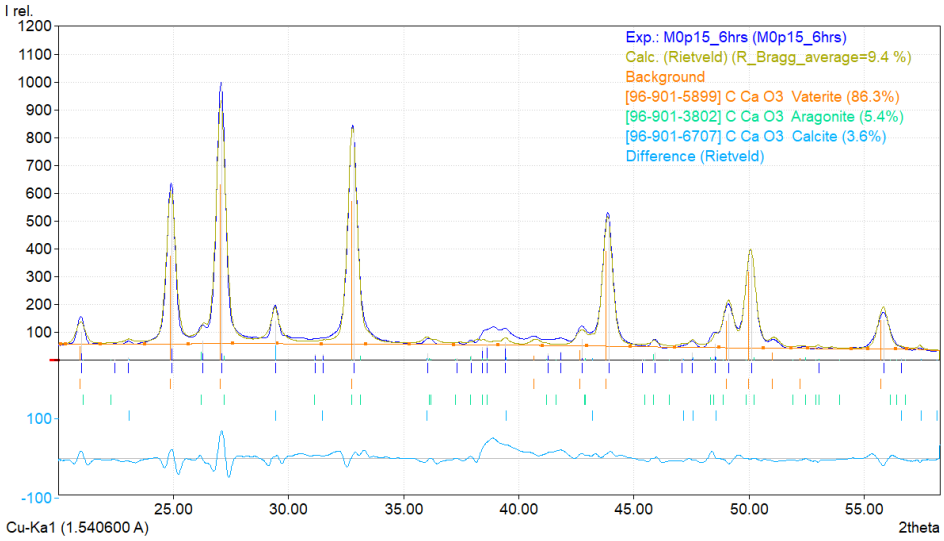

Appendix: A.5 Rietveld refinement of Mg 0.15 M solution at 6 hours.

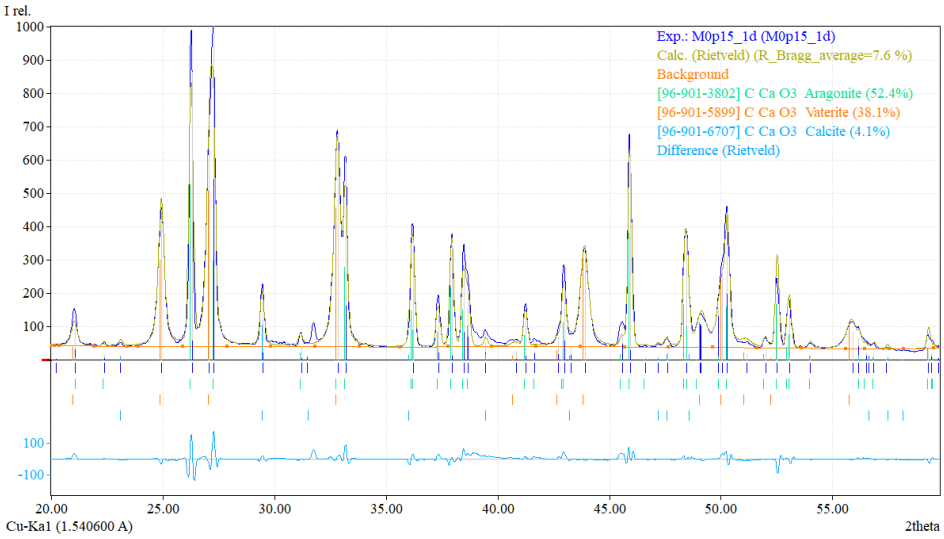

Appendix: A.6 Rietveld refinement of Mg 0.15 M solution at 1 day.

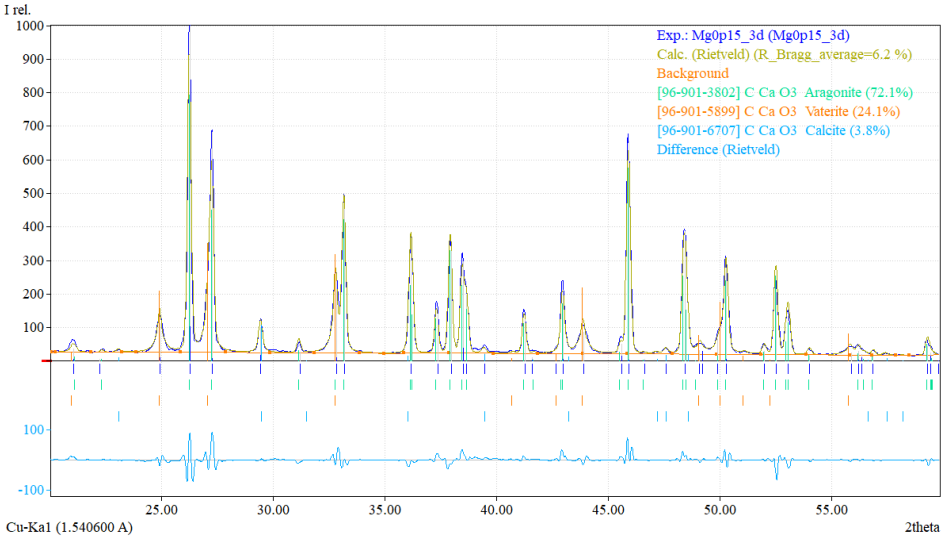

Appendix: A.7 Rietveld refinement of Mg 0.15 M solution at 3 days.

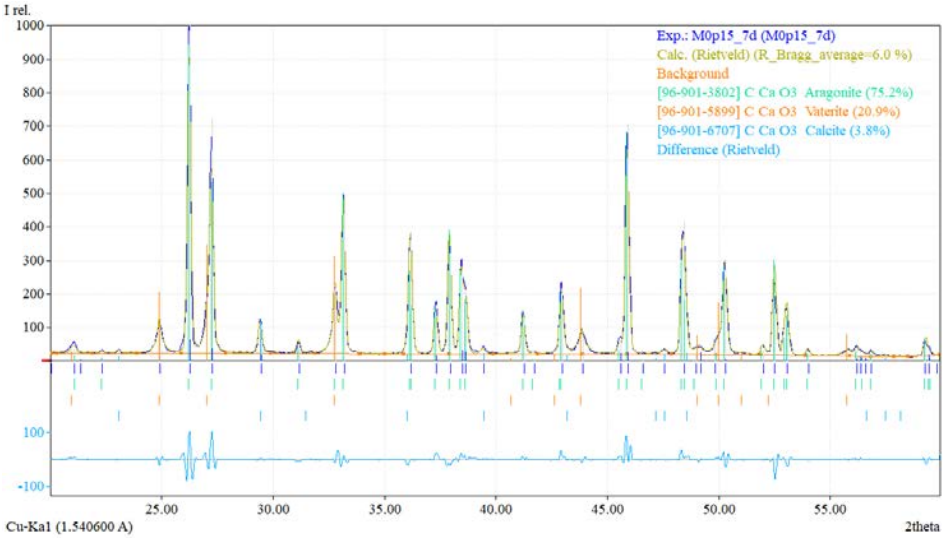

Appendix: A.8 Rietveld refinement of Mg 0.15 M solution at 7 days.

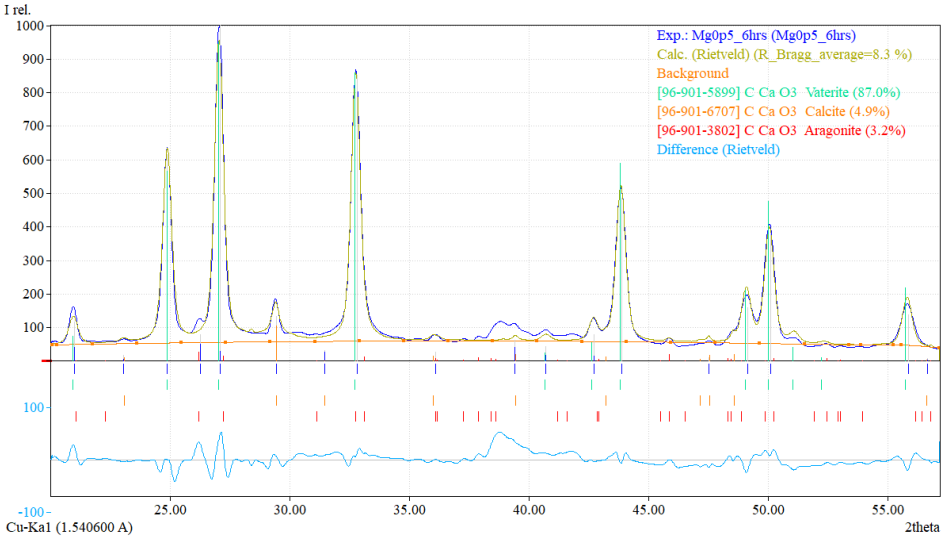

Appendix: A.9 Rietveld refinement of Mg 0.50 M solution at 6 hours.

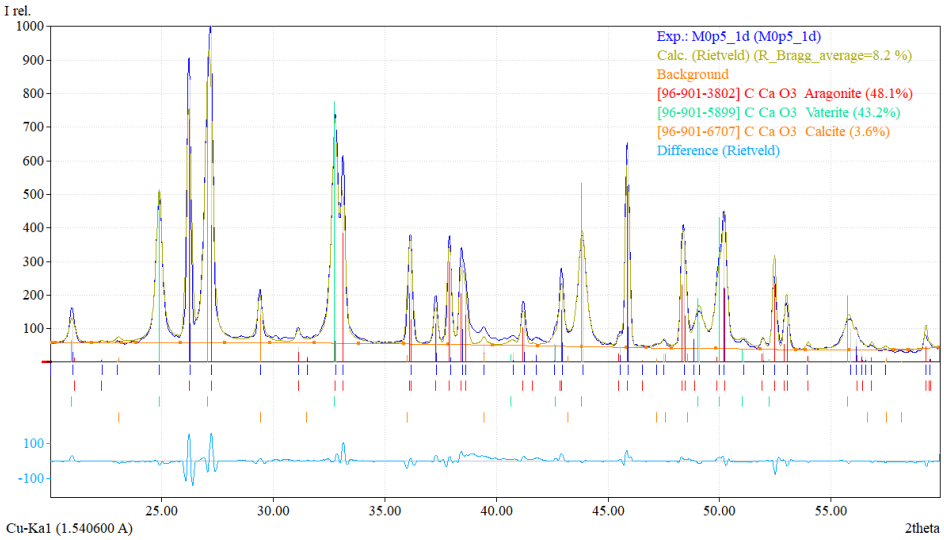

Appendix: A.10 Rietveld refinement of Mg 0.50 M solution at 1 days.

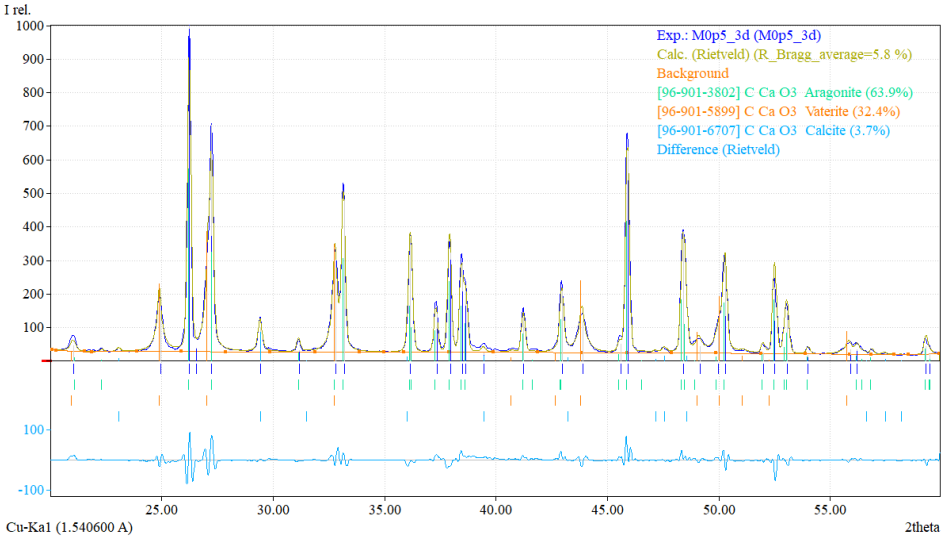

Appendix: A. 11 Rietveld refinement of Mg 0.50 M solution at 3 days.

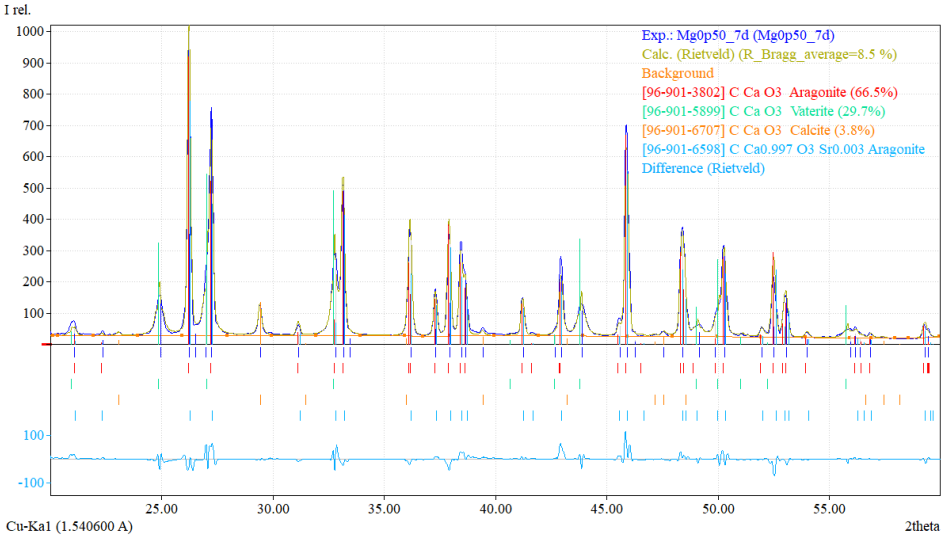

Appendix: A. 12 Rietveld refinement of Mg 0.50 M solution at 7 days.

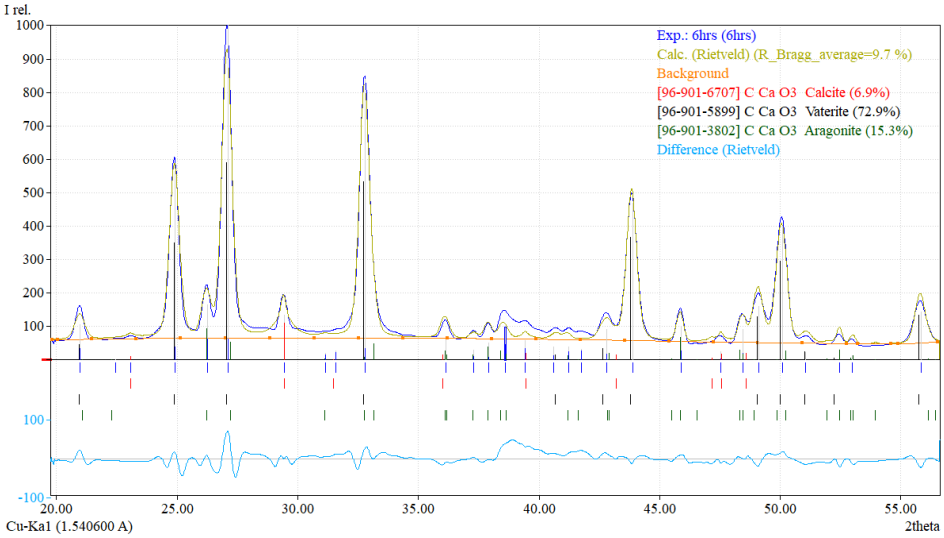

Appendix: A. 13 Rietveld refinement of Mg 0.15 M & Sr^{2+}0.05 M solution at 6 hours.

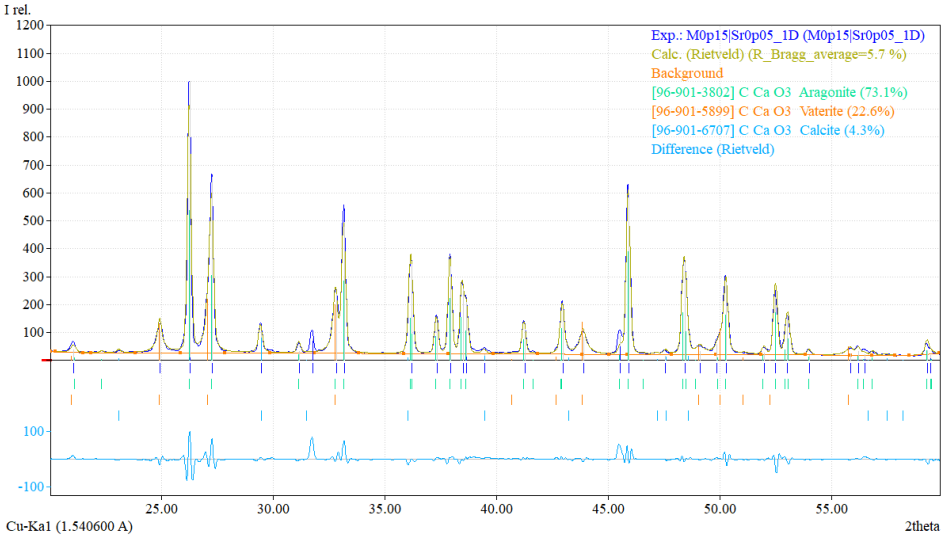

Appendix: A. 14 Rietveld refinement of Mg 0.15 M & Sr^{2+}0.05 M solution at 1 days.

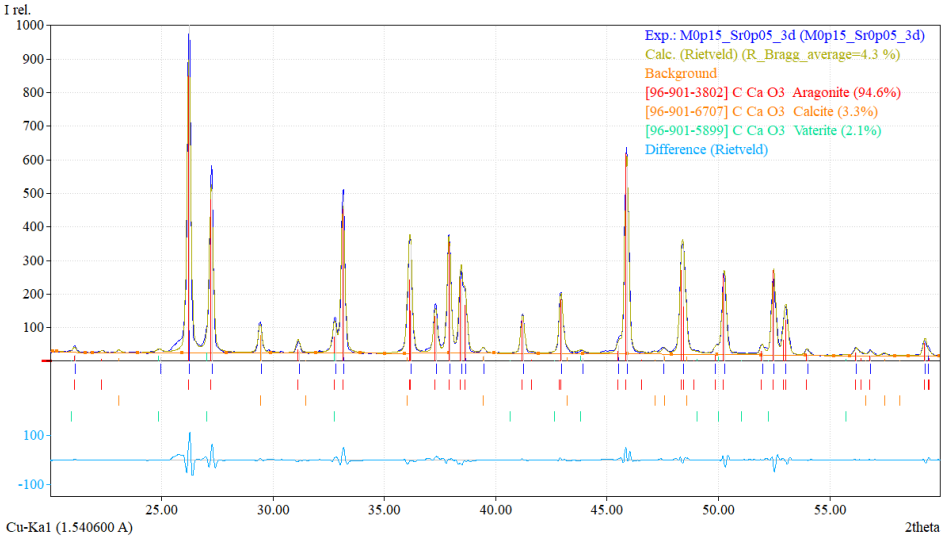

Appendix: A. 15 Rietveld refinement of Mg 0.15 M & Sr^{2+}0.05 M solution at 3 days.

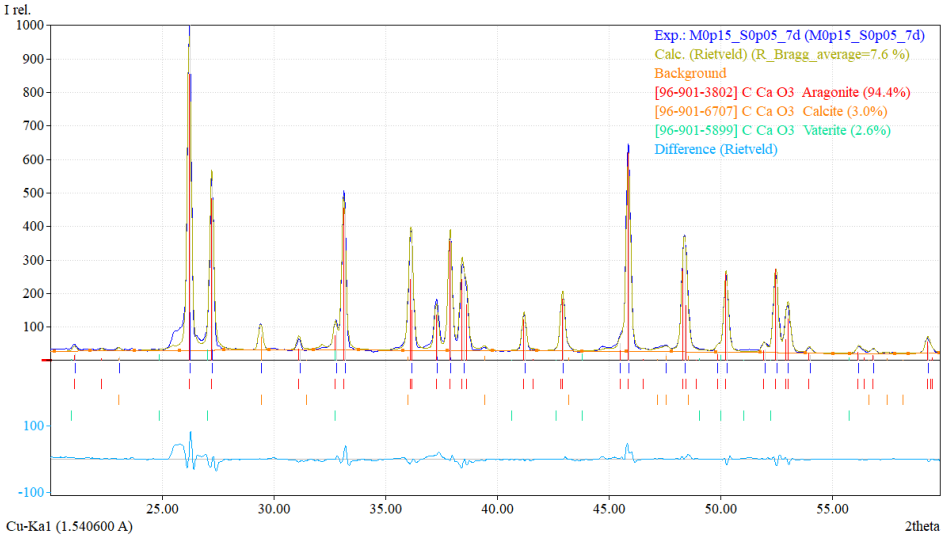

Appendix: A. 16 Rietveld refinement of Mg 0.15 M & Sr^{2+}0.05 M solution at 7 days.

Appendix: A. 17 Calcite lattice parameter in different ages for Mg^{2+}: 0.05 M solution.

Age	a = b (Å)	c (Å)	R Bragg factor	χ^2
Initial calcite	4.984	17.038		
6 hours	4.985	17.051	10.8	5.7
1 day	4.984	17.049	7.9	6.5

Appendix: A. 18 Aragonite lattice parameter in different ages for Mg^{2+}: 0.15 M solution. Reference aragonite is the orthorhombic aragonite model that used in the refinement model

Age	a (Å)	b (Å)	c (Å)	R Bragg factor	χ^2
Reference aragonite	4.962	7.969	5.743		

Age	a (Å)	b (Å)	c (Å)	R Bragg factor	χ^2
6 hours	4.973	7.945	5.676	9.4	4.6
1 day	4.958	7.961	5.740	7.6	5.0
3 day	4.958	7.961	5.740	6.2	2.9
7 day	4.958	7.960	5.739	6.0	3.0

Appendix: A. 19 Calcite lattice parameter in different ages for Mg^{2+}: 0.15 M solution.

Age	a = b (Å)	c (Å)	R Bragg factor	χ^2
Initial calcite	4.984	17.038		
6 hours	4.988	17.040	9.4	4.6
1 day	4.987	17.042	7.6	5.0
3 day	4.991	17.036	6.2	2.9
7 day	4.990	17.036	6.0	3.0

Appendix: A. 20 Aragonite lattice parameter in different ages for Mg^{2+}: 0.50 M solution. Reference aragonite is the orthorhombic aragonite model that used in the refinement model.

Age	a (Å)	b (Å)	c (Å)	R Bragg factor	χ^2
Reference aragonite	4.962	7.969	5.743		
6 hours	5.923	9.055	4.054	8.3	5.3
1 day	4.959	7.963	5.741	8.3	4.4
3 day	4.957	7.960	5.740	5.8	3.0
7 day	4.957	7.959	5.738	8.6	3.0

Appendix: A. 21 Calcite lattice parameter in different ages for Mg^{2+}: 0.50 M solution.

Age	a = b (Å)	c (Å)	R Bragg factor	χ^2
Initial calcite	4.984	17.038		
6 hours	4.984	17.054	8.3	5.3
1 day	4.985	17.058	8.3	4.4
3 day	4.989	17.044	5.8	3.0
7 day	4.990	17.030	8.6	3.0

Appendix: A. 22 Aragonite lattice parameter in different ages for Mg^{2+}: 0.15 & Sr^{2+}: 0.05 M solution. Reference aragonite is the orthorhombic aragonite model used in the refinement model.

Age	a (Å)	b (Å)	c (Å)	R Bragg factor	χ^2
Reference aragonite	4.962	7.969	5.743		
6 hours	4.963	7.960	5.742	9.7	3.9
1 day	4.960	7.963	5.742	5.6	3.4
3 day	4.958	7.961	5.740	4.3	2.8
7 day	4.960	7.964	5.742	7.6	3.1

Appendix: A. 23 Calcite lattice parameter in different ages for Mg^{2+}: 0.15 M & Sr^{2+}: 0.05 M solution.

Age	a = b (Å)	c (Å)	R Bragg factor	χ^2
Initial calcite	4.984	17.038		
6 hours	4.987	17.048	9.7	3.9
1 day	4.989	17.044	5.6	3.4
3 day	4.985	17.041	4.3	2.8
7 day	4.988	17.041	7.6	3.1